Glass dynamics in confinement examined with quasi-elastic nuclear resonant forward scattering

Dissertation zur Erlangung des Doktorgrades des Fachbereichs Physik der Universität Hamburg

vorgelegt von

Gerd Wellenreuther

aus

Göttingen

Hamburg

2005

Gutachter der Dissertation:

Prof. Dr. Jochen Schneider
Prof. Dr. Wilfried Wurth

Gutachter der Disputation:

Prof. Dr. Jochen Schneider
Priv. Doz. Dr. Ralf Röhlsberger

Datum der Disputation:

2. August 2005

Vorsitzender des Prüfungsausschusses:

Dr. Michael Martins

Vorsitzender des Promotionsausschusses:

Prof. Dr. Günter Huber

ABSTRACT

Since Adam and Gibbs proposed their theory of cooperatively rearranging regions in 1965 [AG65] our understanding of the liquid-glass transition is connected to the concept of cooperativity. This theory implies a temperature-dependent radius of cooperativity, which diverges at the glass transition, the so-called ***divergent length scale***. While the necessity of a *divergent time scale* for the glass transition is widely accepted nowadays (e.g. in advanced theories like mode-coupling theory), the existence of the divergent length scale is still subject to controversy. The principal question of its existence can be addressed by experiments concerning glass forming liquids in confinement, since the dynamics of a confined glass is expected to deviate strongly from the dynamics of a bulk glass as soon as the confining radius approximately matches the length scale of cooperativity.

Nuclear resonant scattering is an experimental method suited to study the fast and slow dynamics of a glass with atomic resolution. First experiments on the model glass-former dibutylphthalate:ferrocene confined in controlled pore glasses yielded evidence for a shift of the glass transition to higher temperatures, but were unable to discern whether this was caused by the surface-glass interaction or induced by the geometrical confinement [ASF$^+$01].

In this work nuclear resonant scattering experiments were performed using the oriented channels of mesoporous silicon as a confining matrix; Mößbauer spectroscopy is applied as a complementary experimental method. The temperature dependencies of experimental parameters like the relaxation time and the Lamb-Mößbauer factor yielded new insights into the glass transition and the connected molecular dynamics. In all cases shifts of the mode-coupling critical temperature T_C to higher temperatures were observed. The orientation dependencies were used to discern between confinement-induced effects and effects of other origin, e.g. surface-molecule interactions: Both surface-molecule interactions and confinement effects are contributing to the upward shift of T_C in our sample.

From this the opportunity arises to test our current understanding of the glass transition, in particular predictions made by mode-coupling theory and molecular dynamics simulations. Mode-coupling theory predictions are better fulfilled in the less-confining direction than in the more-confining case, which is interpreted as a smearing of the glass transition in confinement.

ZUSAMMENFASSUNG

Seit Adam und Gibbs 1965 ihre Theorie der kooperativ rearrangierenden Regionen vorschlugen, ist unser Verständnis des Flüssigkeits-Glas-Überganges verbunden mit dem Konzept der Kooperativität. Diese Theorie setzt einen temperaturabhängigen Kooperativitätsradius voraus welcher am Glasübergang divergiert, die sogenannte ***divergierende Längenskala***. Während die Notwendigkeit einer *divergierenden Zeitskala* für den Glasübergang heutzutage im wesentlichen akzeptiert ist (z.B. in fortgeschrittenen Theorien wie der Modenkopplungstheorie), ist die divergierende Längenskala immer noch Gegenstand einer Kontroverse. Die grundsätzliche Frage ihrer Existenz kann durch Experimente an Glasbildnern in geometrischem Einschluss untersucht werden, da angenommen wird, dass die Dynamik eines eingeschlossenen Glases sich stark von der eines freien Glases unterscheidet, sobald der Einschlussradius etwa der kooperativen Längenskala entspricht.

Kernresonante Streuung ist eine experimentelle Methode, die gut geeignet ist, um die schnelle und langsame Dynamik eines Glases mit atomarer Auflösung zu studieren. Erste Experimente mit dem Modelglasbildner Dibutylphthalat:Ferrocene, eingeschlossen in porösen Gläsern, ergaben eine Verschiebung des Glasüberganges zu höheren Temperaturen, aber es war nicht möglich zu entscheiden, ob dies hervorgerufen wurde durch die Wechselwirkung zwischen Oberfläche und Glas oder erzeugt wurde durch den geometrischen Einschluss [ASF+01].

In dieser Arbeit wurden Kernresonanz-Experimente durchgeführt unter Benutzung einer Matrix aus den orientierten Kanälen mesoporösen Siliziums; Mößbauerspektroskopie wurde angewandt als eine komplementäre experimentelle Methode. Die Temperaturabhängigkeiten von experimentellen Parametern wie der Relaxationszeit und des Lamb-Mößbauerfaktors führten zu neuen Erkenntnissen über den Glasübergang und die mit ihm verbundene molekulare Dynamik. In allen Fällen wurden Verschiebungen der kritischen Moden-Kopplungs-Temperatur T_C beobachtet. Die Orientierungsabhängigkeiten wurden ausgenutzt, um zwischen den vom geometrischen Einschluss hervorgerufenen Effekten und Effekten anderen Ursprungs, z.B. der Wechselwirkung der Moleküle mit der Oberfläche zu differenzieren: Sowohl Oberflächen als auch Confinement-Effekte tragen zur Erhöhung von T_C in unserer Probe bei.

Dies ermöglicht es, unser heutiges Verständnis des Glasübergangs zu testen, im Besonderen Vorhersagen der Modenkopplungstheorie und Moleculardynamik-Simulationen. Die Vorhersagen der Moden-Kopplungstheorie sind besser erfüllt im Falle der weniger eingrenzenden Richtungen, dies wird interpretiert als hervorgerufen durch eine Verschmierung des Glasüberganges in geometrischem Einschluss.

CONTENTS

Abstract 3

Contents 6

Part I Theoretical Background 13

1. The Glassy State 15

1.1 How to characterize a glass 15

1.2 Theory of the glass transition 21

1.2.1 Free volume theory 21

1.2.2 Adam-Gibbs theory 23

1.2.3 Idealized mode coupling theory 23

1.2.4 Extended mode coupling theory 29

1.3 The glass transition in confinement 30

1.3.1 The search for the divergent length scale 31

1.3.2 Testing mode coupling theory based molecular dynamics simulations 32

2. Experimental Methods 35

2.1 The Lamb-Mößbauer factor 35

2.2 Mößbauer spectroscopy . . . 40
2.3 Nuclear resonant forward scattering . . . 41
2.4 Theory of nuclear resonant scattering . . . 42
2.4.1 Frequency dependence of Mößbauer spectroscopy . . . 44
2.4.2 Time dependence of nuclear resonant forward scattering 45
2.5 Hyperfine Interactions . . . 47
2.5.1 Isomer shift . . . 49
2.5.2 Quadrupole splitting . . . 50
2.5.3 Other hyperfine interactions . . . 52
2.6 Coupling of molecular dynamics and hyperfine interactions . . 54
2.6.1 Kubo-Anderson theory . . . 55
2.6.2 Generalized Kubo-Anderson theory . . . 56
2.6.3 Isotropic fluctuation of the electric field gradient 61
2.6.4 Anisotropic fluctuation of the electric field gradient . . 63
2.7 Small Angle X-ray Scattering . . . 65
2.7.1 SAXS by a cylindrical pore . . . 65
2.7.2 Simulation of SAXS-patterns . . . 66

Part II Experiments 69

3. Sample . . . 71
3.1 The Model Glass Former DBP:ferrocene . . . 71
3.2 The Confining Matrix: Porous Silicon . . . 72
3.2.1 Application as a confining matrix . . . 73
3.2.2 Production . . . 73

3.2.3 Preparation 75
3.2.4 Characterization with SAXS 75
3.2.5 Filling DBP:ferrocene into the pores 79

4. *Quasi-elastic nuclear forward scattering experiments* 81
4.1 Setup 81
4.1.1 Sample description 84
4.2 Results 85
4.2.1 Data analysis 86
4.2.2 Static model fits 88
4.2.3 Principal quadrupole splitting: Motional narrowing . . 91
4.2.4 Second quadrupole splitting: Relative fraction 93
4.2.5 Isomer shift of the second quadrupole splitting 95
4.2.6 Fast decaying line 97
4.2.7 Effective thickness: Shift of T_C / Deviations from MCT 99
4.2.8 Molecular diffusion 102

5. *Mössbauer spectroscopy* 105
5.1 Setup 105
5.2 Mößbauer spectroscopy with confined DBP:ferrocene 106
5.3 Results 106
5.3.1 Data analysis 106
5.3.2 Spectra and Fits for sample #2 107
5.3.3 Spectra and Fits for sample #4 108
5.3.4 Principal quadrupole splitting 109

5.3.5 Second quadrupole splitting 110
5.3.6 Isomer shift of the second quadrupole splitting 111
5.3.7 Lamb-Mößbauer factor 113
5.3.8 Additional line broadening 114

6. X-ray Absorption Near Edge Structure experiments 117
6.1 Setup 118
6.2 Results 119
6.2.1 XANES-spectra 119
6.2.2 Intensity of the pre-peak 121
6.2.3 Position of the absorption edge 121

7. Modelling of results 123
7.1 Anisotropic relaxation: The MONDIA approach 123
7.2 Results from MONDIA 126
7.2.1 Fits with MONDIA 127
7.2.2 Principal quadrupole splitting 130
7.2.3 Onset of anisotropic rotation 132
7.2.4 Onset of isotropic rotation 134

8. Discussion 137
8.1 Origin of the reduced quadrupole doublet 137
8.2 Chemical change of the valence state 138
8.2.1 Mixing of the valence-state of ferrocene 138
8.2.2 Oxidation of ferrocene in porous silicon? 140
8.3 Anisotropic relaxation of the ferrocene molecule 142

8.4 The glassy dynamic of DBP:ferrocene in porous silicon 145

8.4.1 Diffusive molecular motion 145

8.4.2 The shift of the critical temperature T_C 147

9. Conclusion 149

Appendix 151

A. Acknowledgements 153

B. Bibliography 155

Part I

THEORETICAL BACKGROUND

1. THE GLASSY STATE

Despite a large research effort in the last century there exists still no complete theory for the glassy state which is able to explain its development and its dynamics quantitatively, e.g. in comparison to the very well understood crystalline state. This can be attributed to the fact that molecular dynamics and thermodynamics are getting increasingly complex when dealing with non-equilibrium-states of $N \approx 10^{23}$ different molecules moving around cooperatively.

Though there has been a lot progress in the last decades. This chapter will start with a short introduction into the phenomenology of the glassy state, and will deal with some of the main ideas and concepts developed to describe the glass transition. The main focus lies on presenting mode coupling theory and its predictions concerning glass dynamics, specifically in confined geometries.

1.1 How to characterize a glass

At first glance one connects the term "glass" with silica glass common to us in everyday items like bottles, jars and windows. In fact a huge number of materials surrounding us are glasses, e.g. almost all plastics. In principle every material can be transferred into the glassy state from the melt, *provided* that its liquid state can be cooled rapidly enough to solidify without crystallization. The supercooled liquid state is unstable and tends to crystallize, but this process can be prevented or at least slowed down e.g. by avoiding the presence of any crystallization nuclei. Easily crystallizing compounds require large cooling rates to transfer them into a glassy state. Usual cooling rates range from 10^{-2} K/s for very good glass formers like silica glasses over $10^3 - 10^9$ K/s needed for production of metallic glasses (Co-Nb, Cu-Zr, Ni-Ti) up to 10^{13} K/s achievable through vapor deposition an cooled surfaces.

Due to this origin a glass is sometimes defined as a ”supercooled liquid”. Unfortunately this term is misleading, since a glass has completely lost its ability to flow, and should not be mistaken for a liquid. Historically this term seems to originate from an incomplete quote of Tamman, who stated that a glass can be understood as ”a *frozen* supercooled liquid”. To be accurate we will instead consider every ***amorphous solid state*** to be a ***glass***, thus clearly discriminating it from both the crystalline and the liquid state. *Amorphous* matter in this context is characterized by not showing any distinct bragg-reflections (which is equivalent to demand the loss of any long rang order), while for *solid* we will have to agree upon a arbitrary value of the shear viscosity η_s (e.g. 10^{12} Pa s) that marks the transition between solid and liquid state.

There are some distinct differences when comparing the liquid-glass with the liquid-crystalline transition: The liquid-crystalline transition (e.g. from water to ice) takes place at a very distinct temperature T_M. We can observe a discontinuity in several thermodynamical variables like specific heat, density, entropy, shear viscosity, ... Latent heat is released, so this is a first order phase transition. The liquid-glass transition is more complex: in a temperature range easily spanning several hundred degrees the viscosity of the liquid melt increases from 10^{-3} Pa s (well above the melting point) through 10^1 Pa s (comparable to honey) to $10^{13.5}$ Pa s (the so-called strain point) and more. No latent heat is observed when a glass is melted, so obviously the liquid-glass-transition is not a first order phase transition. Consequently the first questions arising historically were whether the glass transition is a second order phase transition and if there exists a physically meaningful glass transition temperature comparable to the melting temperature T_M of the liquid-crystalline transition.

The examination of the specific heat c_p in the glass transition regime yields (see Fig. 1.1) a pronounced peak. Other variables like the density show a crossover-behavior in the same region, giving reason to define the

calorimetric glass transition temperature T_g.

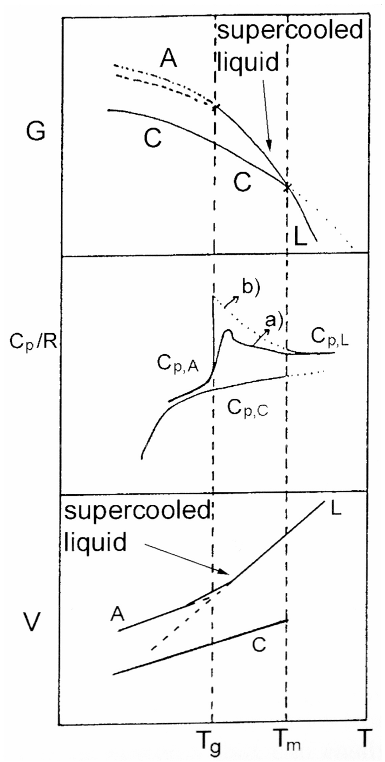

Figure 1.1: Free energy G, specific heat at constant pressure c_p/R and volume V for liquid phase L, crystalline phase C and amorphous phase A. (from [Oss03])

Other definitions for the ***glass transition temperature*** T_g can be made using the shear viscosity ($\eta = 10^{12}$ Pa s at T_g), the viscoplastic relaxation time ($\tau_{visco} = 100$ s at T_g) or the molecular relaxation time ($\tau_{relax} = 100$ s at T_g).

τ_{visco} is the characteristic response time of a sample: For stresses applied for times below τ_{visco} an elastic response is observed, for times above τ_{visco} the sample is subject to plastic flow. According to Maxwell the structural relaxation time relates to the shear viscosity via

$$\tau_{visco} = \frac{\eta_s}{G(\infty)}, \tag{1.1}$$

with $G(\infty)$ being the high-frequency shear modulus, which is about the same for all easy glass-forming liquids ($\approx 10^{10}$ J/m^3) resulting in $\tau_{visco} \approx 100$ s [Oss03].

Surprisingly, values for the molecular relaxation time τ_{relax} measured at q-values corresponding to the maximum of the structure factor also are around 100 s at T_g. Thereby experiments observing molecular dynamics usually refer to the *molecular* or *structural relaxation time* τ_{relax}.

But there are several disadvantages connected to the concept of T_g: Simply setting the glass transition temperature corresponding to an arbitrary value of η_s, τ_{visco}, τ_{relax} or else is far from satisfactory, at least from a scientific point of view. The value of T_g obviously depends upon the method used to determine it, e.g. in case of the calorimetric glass transition temperature the shear viscosity η is often as low as 10^8 Pa s.

Additionally T_g depends upon the applied cooling rate (see Fig. 1.2). Thus a glassy state *remembers* how it was formed, memory effects are playing a role. This implies that a glass is a *non-equilibrium state*, the amount of liquid-like disorder frozen in during the transition depending upon the applied cooling-rate.

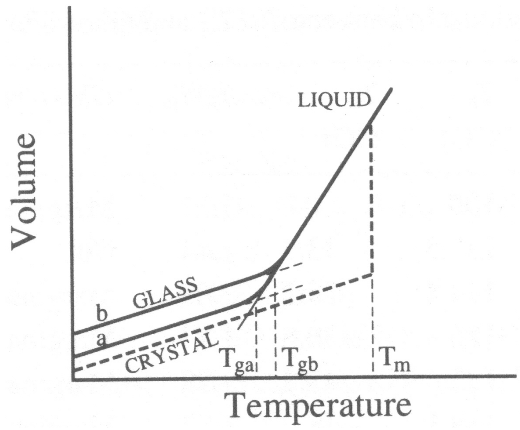

Figure 1.2: Different cooling rates lead to glassy states characterized by different glass transition temperatures T_{ga} (slow cooling) and T_{gb} (fast cooling) and different residual entropy. Taken from [Deb96])

Another characteristic temperature was proposed for so-called *fragile* glasses:

So called *strong* glass formers show a Arrhenius-type dependence between temperature and shear viscosity, while fragile glass formers deviate from Arrhenius-type behavior (see Fig. 1.3), but can be well described by the Vogel-Fulcher-Tammann-equation (short: VFT) below T_g:

$$\eta_s = \eta_0 \, e^{\frac{B}{T-T_0}} \, . \tag{1.2}$$

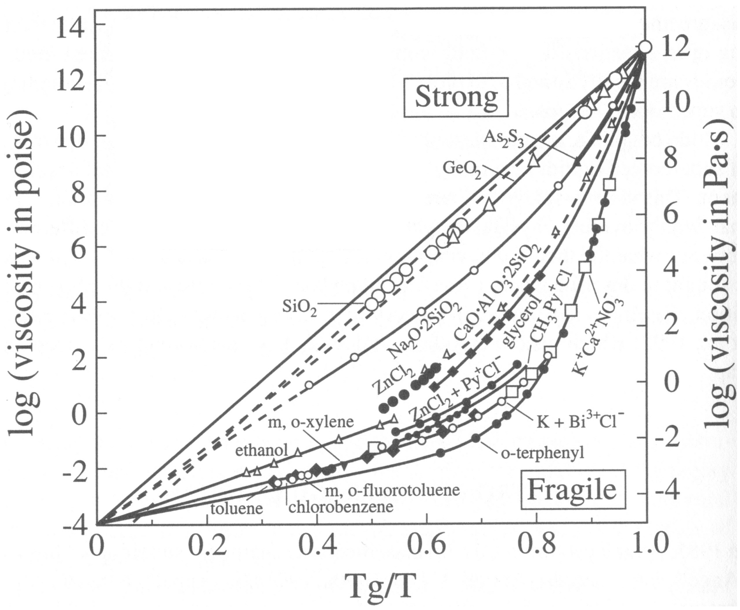

Figure 1.3: Comparison of glass formers of different fragility, with VFT-fits through the corresponding data points. For example, SiO_2 represents a strong and ortho-terphenyl (OTP) a very fragile glass former (from [Deb96])

If $T_0 = 0$ we observe Arrhenius-type behavior, with B corresponding to an activation barrier E/k_B. Fragile glass formers show a positive T_0, leading to a divergence in η_s and thereby in τ_{relax} (1.1). Since all relaxations freeze in at T_0 it is sometimes referred to as the ***ideal glass transition temperature***. The VFT-law successfully describes the steep slope in the shear viscosity of fragile glass formers, but fails beyond $\eta = 10^{12}$ Pa s. In fact the viscosity of real glasses is not diverging, but is always reverting to Arrhenius-like behavior.

Nevertheless the concept of T_0 was generalized by taking a closer look at the configurational entropy. We can disregard contributions from vibrations and mixing by comparing the entropy of the supercooled liquid state and the respective crystalline state at a fixed temperature to measure the *configurational disorder* of the supercooled state as can be seen in Fig. 1.4:

$$S_{conf} = S_{liquid} - S_{crystal}. \tag{1.3}$$

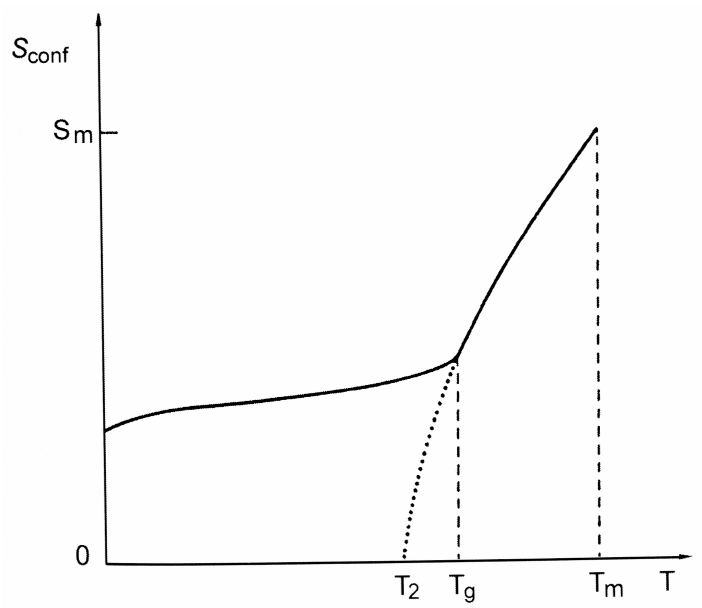

Figure 1.4: Configurational entropy during liquid-glass transition (from [Oss03])

S_{conf} is decreasing during cooling from T_M until T_g is reached. Around T_g a residual entropy remains which stays practically constant down to $T = 0K$, proving hereby that the glassy state is in fact a *non-equilibrium state.*

Applying a lower cooling rate (provided that no crystallization occurs) the supercooled liquid would have more time to relax at higher temperatures, and thereby result in a lower residual entropy. Extrapolation of T_g to lower cooling rates into the experimentally unaccessible domain down to $S_{conf} = 0$ yields the ***ideal glass transition temperature*** or so-called ***Kauzmann temperature*** T_K. It can be understood as a low-cooling-rate-limit glass transition temperature of a liquid with an infinite crystallization barrier. Since the crystalline state has the minimum entropy possible the liquid state has to solidify at T_K. As the names already indicate there is a close correlation between the VFT-derived T_0 and the extrapolated T_K, in fact they are identical in the margin of experimental error (p. 64 in [Oss03], p. 259 Table 4.6 in [Deb96]).

But if configurational entropy reaches its plateau value around T_g, then the glass transition must already be completed - further cooling is not affecting the structure or stability of the now metastable glass, just decreasing the vibrational dynamics. The particles of a real glass may be still diffusing on a very long timescale, but final relaxation (=crystallization) may take virtually forever - several thousand year old stone age arrow heads made of obsidian (a natural glass) have not lost their sharp edges, and amorphous solids from the moon have been dated several billion years old without sign of structural deformation. Since $T_g, T_0/T_K$ only mark the final point of the glass transition the main clue must be hidden somewhere in the non-equilibrium transition from the liquid melt down to those glass transition temperatures mentioned above.

1.2 Theory of the glass transition

There have been several attempts to formulate theories to describe the liquid-glass transition, three of these shall be explained to some extent. The free volume theory and the Adam-Gibbs theory both are classical phenomenological approaches, while the mode coupling theory is a microscopic theory.

1.2.1 Free volume theory

In 1959 Cohen and Turnbull [CT59] proposed the ***free volume theory*** stemming from liquid theory. Particles are modelled by hard spheres moving in the cage formed by their nearest-neighbors. The cage-volume V_{cage} is partly occupied by the self-volume of the spheres V_0 and the remaining free volume V_{free}, in which the particle and its neighbors can diffuse (see Fig. 1.5).

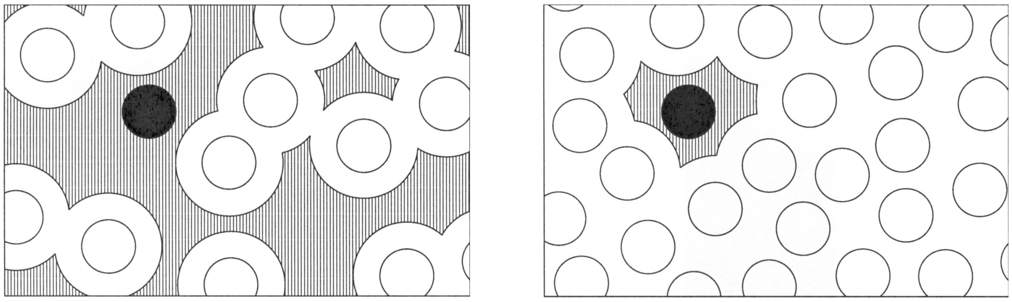

Figure 1.5: Free volume of a particle in a free, "liquid" state (left) and "solid" state. Taken from [Sch03].

In the "liquid" state the free volume is delocalized and diffusive motion is not restricted by neighbors at any time, in contrast to the dense "solid" state where particles are confined in their cages, thus immobilized and in reverse confining their neighbors movements. Cohen and Turnbull postulate that the glass transition is connected to the localization of the free volume, and that below a critical free volume $V_{free,c}$ transport is prohibited.

Starting with several assumptions about the probability density of V_{free}, its thermal expansion and correlation with the shear viscosity η_s and the existence of a critical temperature, the above mentioned VFT-equation (1.2) is deduced. Consequently the critical temperature proposed is identified to be the ideal glass transition temperature T_0.

But there are several drawbacks to this theory: Since no local free energy is needed for free volume redistribution, the modelled system is obviously in equilibrium, in contradiction to the experiment. Additionally, the relevance of the free volume was overestimated, since models of hard spheres with higher density (e.g. the right state displayed in Fig. 1.5) still resemble a liquid state. In fact, the density of a liquid undergoing a liquid-glass transition is only changed by 6-10%, in contradiction to change of density of around 100 % displayed in Fig. 1.5.

Nevertheless the concept of a confining cage made of neighboring particles is instructive and is also used in later theories.

1.2.2 Adam-Gibbs theory

In 1965 Adam and Gibbs [AG65] formulated their theory based on the concept of ***cooperatively rearranging regions (CRRs)***: In a very dense, cool state particles can not move without others cooperating, e.g. moving aside or filling the remaining gap, implying that the configurational degrees of freedom are reduced. Each CRR consists of a number of particles sufficient for cooperative movement, and is supposed to have two possible configurational states. Each CRR is able to change its configuration independently of its environment due to energy fluctuations. These assumptions make calculation of total entropy possible, leading to the insight that the size of the CRRs is growing upon temperature decrease.

Adam and Gibbs were able to derive the VFT-equation from their postulates, but failed to make any further predictions about the glass transition and the CRRs. With aid of the additional assumption that the configurational entropy vanishes below the Kauzmann-temperature T_K

$$S_C(T) \begin{cases} = 0 \quad , & T \leq T_K \\ > 0 \quad , & T > T_K \end{cases} , \tag{1.4}$$

follows that the size of the CRRs is diverging upon approaching T_K. This led to the search for diverging length scales in the field of glass dynamics. Unfortunately, only few evidence for a diverging length scale around T_K or elsewhere has been found [ASG+97].

1.2.3 Idealized mode coupling theory

In 1984 Bengtzelius, Götze and Sjölander [BGS84] and Leutheusser [Leu84] began to formulate a theory to describe the glass transition not based upon phenomenological models, but on a microscopic approach using Kawasakis ***mode coupling theory (MCT)*** [Kaw70]. Initially MCT was used to describe the dynamics of simple liquids. The idealized MCT Bengtzelius et al. proposed describes the liquid-glass transition of a simple liquid made of spherical particles, thus disregarding internal degrees of freedom.

MCT is based upon density-density-correlations. That these are characteristic for the glass transition is justified since the increase in η_s around T_g implies a freezing of density fluctuations. The ***normalized intermediate scattering function*** can be expressed as a autocorrelation function of density-fluctuations

$$F(\mathbf{k},t) = \langle \partial n(\mathbf{k},t)\, \partial n(-\mathbf{k},0)\rangle / N, \tag{1.5}$$

in which $\partial n(\mathbf{k},t)$ are the density fluctuations with respect to the quasi-equilibrium microscopic density $n(t)$. $F(\mathbf{k},t)$ is the Fourier-transform of the well known ***van Hove correlation function*** $G(\mathbf{r},t)$:

$$G(\mathbf{r},t) = \langle \partial n(\mathbf{r},t)\, \partial n^*(\mathbf{0},0)\rangle / \rho. \tag{1.6}$$

Using the *Mori-Zwanzig*-formalism an equation of motion for the correlators can be formulated

$$\begin{aligned} \left[\frac{\partial^2}{\partial t^2} + \frac{\partial}{\partial t}\gamma + \omega^2(\mathbf{k})\right] F(\mathbf{k},t) & \\ + \omega^2(\mathbf{k}) \int_0^t M(\mathbf{k},t-t')\, \frac{\partial}{\partial t'} F(\mathbf{k},t')\,\mathrm{d}t &= 0, \end{aligned} \tag{1.7}$$

with the initial conditions $F(\mathbf{k},0) = 1$ and $\dot{F}(\mathbf{k},0) = 0$, containing a characteristic frequency $\omega^2 = \frac{(k\gamma)^2}{S_\mathbf{k}}$ and a Newtonian friction term $\gamma = \sqrt{kT/m_{mol}}$, m_{mol} being the molecular weight. Equation (1.7) is similar to the differential equation of a harmonic oscillator with an additional damping term, with ω being a vibrational frequency on a picosecond timescale. Since the kernel $M(\mathbf{k},t)$ is evaluated at times between 0 and t the coupling is retarded, which was later deemed crucial for density fluctuations to be able to stabilize. The equation of motion is usually solved by Laplace-transformation:

$$\begin{aligned} F(\mathbf{k},z) &= \frac{-1}{z - \frac{\omega^2}{z+M(\mathbf{k},z)}} \\ M(\mathbf{k},z) &= i\gamma + \omega^2 m(\mathbf{k},z) \end{aligned} \tag{1.8}$$

The solution contains the memory kernel $m(\mathbf{k}, z)$, which depends again on $F(\mathbf{k}, z)$.

We are only interested in slow solutions of (1.7), because fast solutions would describe crystallization processes. Slow solutions are only possible assuming a slow evolution of $m(\mathbf{k}, t)$. Since the memory function should resemble the environment of the particle, and this environment is essentially the cage formed by neighboring particles, $m(\mathbf{k}, t)$ can be expressed as a sum over density fluctuations.

$$m(\mathbf{k}, t) = \sum_{\mathbf{k_1},\mathbf{k_2}} \mathbf{V}_{\mathbf{k},\mathbf{k_1},\mathbf{k_2}} F(\mathbf{k_1}, t)\, F(\mathbf{k_2}, t). \tag{1.9}$$

Self-consistent evaluation of the ***mode-coupling vertex*** $\mathbf{V}_{\mathbf{k},\mathbf{k_1},\mathbf{k_2}}$ is the most demanding part of the solution of (1.9), in the end this leads to the third, lengthy equation which connects $\mathbf{V}_{\mathbf{k},\mathbf{k_1},\mathbf{k_2}}$ with the static two-point correlator (= the static structure factor, which is experimentally accessible), which is directly connected to the intermediate scattering function by

$$S(\mathbf{k}) := F(\mathbf{k}, t = 0), \tag{1.10}$$

and the static three-point correlator $\langle \rho(\mathbf{k})^* \, \rho(\mathbf{k_1})\, \rho(\mathbf{k_2})\rangle$. E.g. Cummins came to a simplified equation for $\mathbf{V}_{\mathbf{k},\mathbf{k_1},\mathbf{k_2}}$ which only depends on the structure factor by neglecting the intermolecular potentials [Cum99]:

$$\mathbf{V}_{\mathbf{k},\mathbf{k_1},\mathbf{k_2}} = \frac{n}{k^4} S(\mathbf{k}) S(\mathbf{k_1}) S(\mathbf{k_2}) \left(C(\mathbf{k_1}) \mathbf{k} \cdot \mathbf{k_1} + C(\mathbf{k_2}) \mathbf{k} \cdot \mathbf{k_2} \right) \tag{1.11}$$

with $C(\mathbf{k}) = \frac{S(\mathbf{k})-1}{nS(\mathbf{k})}$) and n the density. These three equations (Eq. 1.8, 1.9 and 1.11) form a closed set of equations and are called ***mode coupling equations***. Both correlators needed can either be calculated from the intermolecular potentials or measured experimentally, and since no obvious structural changes happen during the liquid-glass transition ($S(\mathbf{k})$ remains almost unchanged), the $\mathbf{V}_{\mathbf{k},\mathbf{k_1},\mathbf{k_2}}$ are only slowly changing, continuous functions of T.

For high temperatures the coupling constants $\mathbf{V}_{\mathbf{k},\mathbf{k_1},\mathbf{k_2}}$ are all small, resulting in a fast decay of any density fluctuation, thereby describing a liquid state. The glassy state is formed at low temperatures with increased coupling constants; here density fluctuations do not decay anymore, they persist and remain localized. The transition between both regimes occurs suddenly as a bifurcation at a critical density ρ_C corresponding to the so-called ***mode coupling critical temperature*** T_C. MCT predicts T_C to be well above the glass transition temperature T_g (difference is 15 - 20 % for fragile glasses, 15 - 60% for strong glasses) [Oss03].

The evolution of the intermediate scattering function during the liquid-glass transition is depicted in Fig. 1.6:

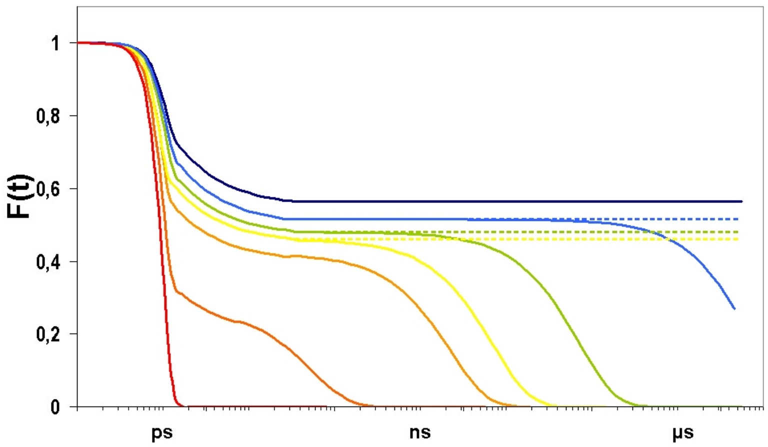

Figure 1.6: Normalized intermediate scattering functions $F(t, \mathbf{k} = \mathbf{const})$: From bottom to top: Cooling of an ideal liquid-state well above T_M (red line) through liquid states (orange / light orange), the liquid-glass transition (yellow) at T_C, glassy states (green / blue) into the ideal glassy state (dark blue) well below T_C.

Well above T_C $F(t, \mathbf{k})$ decays fast to 0 (red line in Fig. 1.6). Still in the liquid regime (orange / light orange) a relaxation process is distinguishable from the phononic vibrations, which then splits into a *slow* and a *fast* part closer to T_C, as the timescale of the slow relaxation process increases dramatically, diverging at T_C (yellow). [1] When the slow decay process completely freezes $F(\mathbf{k}, t)$ stays on a plateau-value for all times indicating structural arrest; this corresponds to the critical temperature of the liquid-glass transition. To characterize the transition the so-called ***non-ergodicity-parameter*** is introduced

$$f(\mathbf{k}) = \lim_{t\to\infty} F(\mathbf{k}, t) = \begin{cases} 0 & \Rightarrow & ergodic \\ > 0 & \Rightarrow & non - ergodic \end{cases} . \tag{1.12}$$

The development of $F(\mathbf{k}, t)$ with decreasing temperature can be understood in more detail with aid of the concept of the confining molecular cages of the free volume theory: At $T \gg T_C$ the particles can diffuse freely, their movements are not hindered by their neighbors. The two components of the relaxational motion discovered upon approaching T_C are identified as: The fast vibrational mode is called *fast β-relaxation* (not to be confused with the slow Johari-Goldstein β-process!), which is attributed to the rattling of the particle inside its cage, and the slow mode is called *α-relaxation*, which is responsible for breaking of the cage and/or movement of the whole cage, thus leading to final relaxation. Starting from sub-nanoseconds in the liquid regime the typical relaxation timescale of the α-relaxation is increasing by several orders of magnitude during cooling, and finally diverges at T_C.

Thereby in ideal MCT no final relaxation can take place below T_C, according to (1.1) the diffusion D constant vanishes and the shear viscosity η_s diverges. This is of course inconsistent with experimental finding that a glass solidifies around the lower T_g, but will be explained in the scope of the extended MCT.

[1] In ideal MCT no further relaxation would take place at or below T_C (dotted yellow / green / blue / dark blue lines). As we will see in extended MCT and real glasses (solid yellow / green / blue / dark blue lines), phonon-induced hopping processes also play a role causing final relaxation to be existent also in glassy states between T_C and T_g, thereby only leading to a plateau-value for intermediate times, before complete structural relaxation takes place. For temperatures sufficiently below T_g the timescale of phonon-induced hopping is almost infinity. Consequently, glassy states are recognized by the existence of a plateau value caused by the splitting of $\alpha-$ and $\beta-$relaxation.

The height of the plateau is directly connected to the vibrational modes and the strength of the β-relaxation, consequently $f(\mathbf{k})$ can be identified as the Lamb-Mössbauer-factor (p. 72 in [Oss03]). MCT predicts its dependence upon T below T_C:

$$F(\mathbf{k}) \begin{cases} 0 & , \quad T > T_C \\ f_C(\mathbf{k}) + c\sqrt{\frac{T_C - T}{T_C}} & , \quad T \leq T_C \end{cases}, \tag{1.13}$$

with $f_C(\mathbf{k}) = f(\mathbf{k})|_{T=T_C}$, c an amplitude factor and $\frac{T_C-T}{T_C} = \sigma$ being the so-called *separation parameter*. Close to T_C MCT further predicts the development of the the intermediate scattering function

$$F(\mathbf{k}, t) = f_C(\mathbf{k}) + h(\mathbf{k})G(t), \tag{1.14}$$

with $|G(t)| \ll 1$, the factorization into t- and $\mathbf{k}$-dependence is stemming from the properties of the divergence at T_C. In the regime $t < \tau_\beta$ the *critical law* applies

$$G(t) = \left(\frac{t}{\tau_\beta}\right)^{-a}, \tag{1.15}$$

with time scale $\tau_\beta(T) \propto |T - T_C|^{-\frac{1}{2a}}$, while the onset of the α-relaxation for $t > \tau_\beta$ and $T > T_C$ is modelled by the *von Schweidler law*

$$G(t) = -\left(\frac{t}{\tau_\alpha}\right)^{b}, \tag{1.16}$$

with time scale $\tau_\alpha(T) \propto (T - T_C)^{-\gamma}, \quad \gamma = \frac{1}{2a} + \frac{1}{2b}$. The two exponents a and b are connected to the *exponent parameter* λ

$$\lambda = \frac{\Gamma^2(1-a)}{\Gamma(1-2a)} = \frac{\Gamma^2(1+b)}{\Gamma(1+2b)}. \tag{1.17}$$

The critical and the von Schweidler law can be used to either scale the β- or the onset of the α-relaxation to fit on a master curve.

Reviewing ideal MCT

Ideal MCT already makes a large number of predictions, e.g. the existence of T_C, the critical and von Schweidler law and their scaling properties, deviations from the VFT-law and more. These have been extensively tested in the temperature range $T > T_C$ with methods like depolarized light scattering, Raman spectroscopy, inelastic coherent neutron scattering, dielectric loss spectroscopy in glass formers like CKN, OTP, Salol, PC, Toluene, isopropylbenzene and hard-sphere colloids among others. For an extensive review see e.g. [GS92].

The *scaling-law for the β-relaxation* was experimentally found to be valid over several orders of magnitude in time in many systems. From the fit the *separation parameters* λ and the *critical temperatures* were extracted. The *factorization property* (1.14) was also proven in the β-relaxation-regime. The *scaling law for the α-relaxation* was e.g. observed to be valid in OTP, Salol and PC for several orders of magnitude, with fits yielding consistent values of T_C and λ.

The *behavior of the non-ergodicity parameter* for $T < T_C$ also yielded values for T_C, but especially in this temperature regime ideal MCT shows deviations from the experiment. These deviations are partially caused by the neglect of phononic excitations. To correct for this usually a separation ansatz is used (see [KBD+92] and references therein):

$$f_{LM}(\mathbf{k}, T) = f_{phonon}(\mathbf{k}, T) \cdot f_{MCT}(\mathbf{k}, T). \tag{1.18}$$

1.2.4 Extended mode coupling theory

The deviations between the predictions of ideal MCT and experiments have partly been attributed to thermally activated *hopping processes* occurring on long time scales. These were taken into account in an ***extended MCT*** (see e.g. [FGHL92] [CDF+93] [DLC+94] [FM99] and references therein). In the case of small hopping rates (1.14) stays valid and a *hopping parameter* δ is introduced in the solution Eq. 1.8:

$$
\begin{aligned}
M(\mathbf{k}, z) &= i\gamma + \omega^2 m(\mathbf{k}, z) / \left(1 - \delta(\mathbf{k}, t)\left[i\gamma + \omega^2 m(\mathbf{k}, z)\right]\right) \\
\delta(\mathbf{k}, t) &= \sum_{\mathbf{k_1}, \mathbf{k_2}} \mathbf{V}'_{\mathbf{k}, \mathbf{k_1}, \mathbf{k_2}} F(\mathbf{k_1}, t)\, \ddot{F}(\mathbf{k_2}, t). \qquad (1.19)
\end{aligned}
$$

This hopping kernel is similar to the memory kernel from Eq. 1.9. It reflects the fact that from time to time a particle has enough thermal energy to overcome the potential barriers between different states, while the mean thermal energy is insufficient to allow for frequent hopping. Through these **hopping processes** ergodicity is restored in the long-time limit, and the singularity at T_C is smeared out due to the transition from liquid-like cage-dynamics to solid-like hopping processes.

Hopping processes are also responsible for shifting the final solidification of glasses from T_C until T_g: Without hopping, a glass would instantly freeze at T_C. The extended MCT describes the relaxations below T_C as purely thermally activated, so the low viscosity of the glassy state between T_C and T_g can be compared the softening of the crystalline state just below T_M.

Ideal MCT stems from liquid theory, where particles have coordination numbers of ≈ 12 and are assumed to have spherical symmetry, thus neglecting rotational degrees of freedom. For strong glass formers like network-building SiO_2, B_2O_3 the coordination numbers are clearly different, and consequently ideal MCT fails to describe these samples [GS92]. In addition, for most real glass forming liquids the assumption of spherical molecules is obviously not true. First steps to extend MCT in this domain are accounting for rotational motion [Käm97] [Käm04] [Sch00].

1.3 The glass transition in confinement

All theories described above only apply to bulk-like states of liquids or glasses. Addressing the question of how the liquid-glass transition changes upon introducing geometrical confinement should lead to insights about the fundamental glass-forming mechanism. The unsolved question of the ***existence***

of a divergent length scale in glass dynamics could be addressed. In addition, the results of recent molecular dynamics simulations also searching for insight into the problem of the divergent length scale could be compared with experimental data.

1.3.1 The search for the divergent length scale

In all theories described above it is consensual that there exists a *divergent time scale* of the molecular dynamics at or around the corresponding glass transition temperature. Additionally, theories based upon the Adam-Gibbs-model of cooperatively rearranging regions thereby imply a *divergent length scale*. On the other hand, neither ideal or extended MCT needs an additional divergence in space to model the liquid-glass transition [GS92], the typical length scale being introduced by the self-consistent blocking of particle movement trapped in the cages. But recent research indicates that also the MCT transition must be understood as a divergence both in space and time [BB04].

Experiments by Arnd et. al [ASG$^+$97] imply a length scale of cooperativity in the order of several nm at the calorimetric glass transition temperature T_g for Salol confined in mesoporous material (controlled pore glasses with 2.5 - 7.5 nm mean pore radius).

Nevertheless, it is unclear whether the effect of confining a liquid results into a slowing down or a speeding up of its dynamics (see [McK03] [FKZ03]). One often used argument supplied by MCT is that confinement would inhibit cooperative modes associated with slow glass dynamics around T_C (cage effect), and thus leads to a further *slowing down of dynamics*. This would only apply to translational dynamics, since ideal MCT neglects rotational degrees of freedom. On the other hand, Arnd et al. state that in the case of rotational dynamics unhindered by the presence of a wall a *speeding up of dynamics* would have to be observed, since the radius of cooperativity in a confined liquid could not extend to values greater than the pore diameter.

This controversy displays that it is nontrivial to distinguish between effects induced by geometrical confinement and the interaction of the glass with the surface of the pore (see [SF03] and in general [FKZ03]). Apart from the effect of confinement chemical interactions between the particles and the pore wall (ranging from Van-der-Waals-interaction, hydrogen-bonds, charge transfer up to formation of chemical bonds) are playing a role, and there may be an additional influence due to the topology of the confining surface.

The surfaces of mesoporous matrices like controlled pore glasses are often passivated with silan-groups in order to reduce the chemical interaction. Other matrices like urea-clathrates are synthetisized with the sample as a structure-directing agent. These matrices sometimes are *unstable* without the sample inside the pore, thereby the chemical interaction of wall and sample obviously has to be taken into account.

Additionally, a flat wall will lead to adsorption of particles in dense layers (so-called "layering"). This dramatically changes the density and the structural properties close to the wall in a first step, and further effects the properties of a glassy liquid even at a distance of a few particle diameters due to the self-blocking behavior as described by MCT or due to the size of CRRs in Adam-Gibbs-based theories.

1.3.2 Testing mode coupling theory based molecular dynamics simulations

There exist many methods to observe glass dynamics in confinement, e.g. neutron scattering, NMR, dielectric spectroscopy, nuclear resonant scattering . . . [FKZ03]. Due to the unique possibilities to model the wall-particle interaction, molecular dynamics simulations are well suited to study the effects induced by a **flat pore wall** in detail. Scheidler et al. [SKB02] compared molecular dynamics (MD) simulations of a bulk-like sample formed by binary Lennard-Jones (LJ) particles with a film consisting of the identical binary mixture facing a smooth and a rough wall. The realization of the smooth wall was achieved by an external exponential potential which additionally coupled to changes of the density of the glass, thereby prohibiting layering successfully. The rough wall was realized by freezing particles. As a consequence the structure of the film is in both cases comparable to the bulk.

In the first case the dynamics of particles close to the wall was *speeded up* because particles could slip along the smooth walls; in the second case the dynamics was *slowed down*, which can be attributed to the hindering of cooperative modes close to the wall. In both cases the radius of the region affected by the wall grew with decreasing temperature.

Scheidler et al. argue that a passivated wall (a wall which only interacts via Van-der-Waals interaction with the confined glass) should resemble their case of a LJ fluid close to a smooth wall, and a wall forming H-bonds behaves more like a rough wall. Consequently they interpret the results of Arnd et al. as an superposition of fast dynamics close to the pore wall and bulk-like dynamics in the middle of the pore, leading to the observed increase of overall relaxation.

Scheidler et al. also studied the dynamics of a LJ liquid confined in a **mesoporous pore** by molecular dynamics simulations [SKB00], [SKB03]. The concepts of the rough and the smooth wall formed by freezed LJ-particles are used to from circular pore walls (pore diameter corresponding to 5 particle diameters). The MD simulations yield the intermediate scattering function $F_s(\mathbf{k}, t)$, which Scheidler et al. compare with results obtained from bulk-like simulations. In both cases the cage-effect and final relaxation are observable[2], but the dynamics in the case of the rough wall is strongly slowed down, while in the case of the smooth wall a speed up is observed.

Additionally in the case of the rough wall, the shape of $F(\mathbf{k}, t)$ contains an additional tail component, which grows with decreasing temperatures. This stretching corresponds to a broader distribution of relaxation times[3], in other words: Confinement increases the heterogeneity of the glassy dynamics.

Further investigation of the radial dependence of $F(\mathbf{k}, t)$ gave evidence for a strong slowing down of particles close to the pore wall, even if the particles constituting the wall were at non-zero temperatures. The slowing down is

[2] Due to the immense computing time needed to equilibrate an ensemble during cooling, MD simulations are today only able to observe dynamics approaching the critical temperature T_C from the liquid regime.

[3] Final relaxations can often be well described by the so-called "stretched exponential" Kohlrausch function $F(\mathbf{k}, t) = e^{-\left(\frac{t}{\tau_K}\right)^{\beta}}$.

consequently attributed to the suppression of cooperative modes close to the rough wall, while the speed up corresponds to particles slipping along the smooth wall.

2. EXPERIMENTAL METHODS

First a short introduction into the Lamb-Mößbauer factor, Mößbauer spectroscopy and nuclear resonant forward scattering is given. Since these techniques are based upon nuclear scattering of X-rays, the theory of nuclear resonant scattering is presented in the second part of this chapter. In the third part the influence of translational and rotational molecular dynamics on hyperfine interactions is explained, and the Blume-formalism is applied to describe anisotropic rotation.

The last section focuses on small angle scattering, which was used to characterize the sample matrices.

2.1 *The Lamb-Mößbauer factor*

Heisenbergs uncertainty principle $\Delta E \Delta\tau \geq \hbar$ can be used to connect the energy spread of a radiated photon with the life time of the corresponding excited state. A state with a life time of $\Delta\tau$ would have to emit energy at least with an energy spread of ΔE; there can not exist any truly harmonic sources (a purely sinusoidal wave has $\Delta E = 0$), this would in return lead to an infinite life time and thereby would prohibit any radiation or decay. Thus *every* source has to radiate energy within a finite linewidth, the so-called *Heisenberg natural linewidth* Γ_{nat}.

These arguments hold for any source, for electronic as well as nuclear transitions. Electronic transitions normally occur on a femtosecond timescale, leading to natural linewidths of some electron-Volts (short eV). In contrast, nuclear transitions have nano- to microseconds lifetimes, resulting in

$\Gamma_{nat} \approx 0.01 - 100$ neV, e.g. 4.66 neV for ^{57}Fe, the most important Mößbauer-nucleus. In all of the following calculations a ^{57}Fe-nucleus is considered, since this is only one used in this work.

Observing these small natural linewidths is nontrivial in experiment due to the *Doppler-shift*: Radiation emitted by a moving nucleus will experience a frequency-shift:

$$\Delta\omega_{Doppler} = \mathbf{k} \cdot \mathbf{v_{nucleus}}. \tag{2.1}$$

In a gas the velocities are distributed according to the Maxwell distribution, thereby at a thermal velocity of $\approx$ 100 m/s the resulting Doppler-broadening is already of the order of 200 meV, at least five orders of magnitude larger than Γ_{nat}!

Because a photon carries a momentum of $\hbar k$ every emission- or absorption-act results in a *recoil-shift* suffered by the nucleus. In the case of an emission by a resting atom the emitted photon is lacking E_{recoil} of the total transition energy E_γ, thus shifting the emitted line to lower energies, whereas absorption by a resting atom requires the photon to have E_{recoil} in excess of E_γ. These lines both suffer Doppler-broadening as can be seen in Fig. 2.1.

Taking Doppler- and recoil-shift into account the frequency of a photon is

$$\omega = \omega_0 + \underbrace{\mathbf{k} \cdot \mathbf{v_{nucleus}}}_{Doppler-shift} \mp \underbrace{\frac{\hbar \mathbf{k^2}}{2M}}_{recoil-shift}, \tag{2.2}$$

with $-$ for emission and $+$ for absorption. As can be seen in Fig. 2.1 without Doppler-broadening (solid lines) the recoil-shift would completely inhibit the possibility of re-absorption of an emitted photon, since the absorption curves have virtually no overlap. In contrast, the Doppler-broadened lines (dashed lines in Fig. 2.1 overlap in a large energy range.

Because binding energies in solids ($\approx$ eV) exceed the recoil energy by far, atoms are fixed to their lattice sites and thereby can not absorb recoil

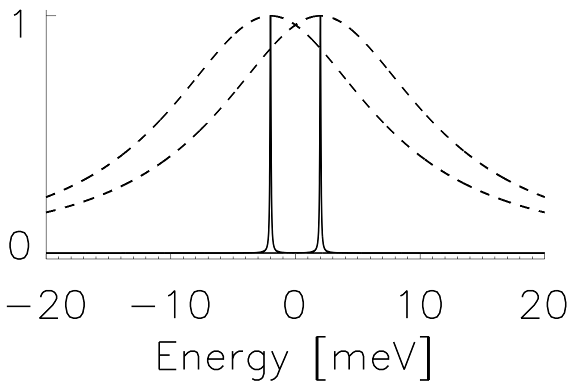

Figure 2.1: Recoil-shift and Doppler broadening in the case of ^{57}Fe. The linewidth of the narrow line is 0.1 meV, so still broadened by a factor of 20.000 with respect to the natural linewidth $\Gamma_{nat} = 4.66 neV$ of ^{57}Fe. This large factor is needed to magnify the otherwise not perceivable natural line width, since the recoil energy is $E_{recoil} = 1.96$ meV. The dashed (- -) line corresponds to Doppler broadening of 20 meV. Observe the amount of both lines overlapping below the thick line resembling the increased chance of re-absorption.

freely. But they participate in the vibrational dynamics, so recoil may lead to creation of phonons. Typical phonon-energies are in the order of meV, thereby we could in a simple fashion assume that the emission of a γ-quantum from the nucleus will lead to excitation of phonons, which carry the recoil-energy, inevitably inhibiting further re-absorption. At higher temperatures the recoil energy could be provided by annihilation of phonons. One would thereby assume that the fraction of re-absorbed photons would decrease with decreasing temperature.

But Rudolf Mößbauer discovered an increase of re-absorption at lower temperatures and explained this with an increased probability for so-called *recoilless emission/absorption*. Recoilless means that no phonons are excited or annihilated, thereby the γ-quantum experiences no energy shift. The fraction of recoilless emission f_{LM} is called the ***Lamb-Mößbauer factor***, since Mößbauer used results from Lamb[1] in his derivation of the recoilless

[1] Lamb first calculated f_{LM} in 1939 when examining scattering of cold neutron from crystals. [Lam39]

fraction.

Recoilless emission in fact predominates over *all other* processes involving phonon excitation (with $\approx 10^{23}$ modes!) at low and intermediate temperatures, this is called the ***Mößbauer Effect.*** This is caused by the boson-nature of phonons: Since bosons tend to populate the same quantum-mechanical states, and only very few phonon-modes are populated at low temperatures, the excitation of a single phonon in a new mode is highly improbable. Nevertheless energy conservation is not violated as the total excitations average out to the classical value of the recoil-energy $\frac{\hbar^2\mathbf{k^2}}{2M}$.

To apply the Mößbauer Effect in physics we need a reasonable absorption and emission cross section. Of course, this implies a high Lamb-Mößbauer factor. The Lamb-Mößbauer factor is closely related to the *Debye-Waller* factor known from X-ray diffraction, both stemming from the relative phase term induced by motion or static disorder in the structure factor:

$$f = \exp\left(-\frac{1}{2}(\mathbf{k}_f - \mathbf{k}_0)^2 \cdot \langle x^2 \rangle\right). \tag{2.3}$$

X-ray scattering takes place on a 10^{-16} - 10^{-15} s timescale, thus being much faster than the typical vibration times 10^{-14} - 10^{-13} s. The average can be approximated by

$$f_D = \langle \exp\left(-i\mathbf{k}_f \cdot \mathbf{x}(\mathbf{t} \approx \mathbf{0})\right) \exp\left(i\mathbf{k}_0 \cdot \mathbf{x}(\mathbf{0})\right)\rangle. \tag{2.4}$$

But since nuclear transitions take place on a timescale of 10^{-10} - 10^{-6} s the position of the nucleus during absorption and emission is uncorrelated and thereby the average factorizes:

$$f_{LM} = \langle \exp\left(-i\mathbf{k}_f \cdot \mathbf{x}\right)\rangle \langle \exp\left(i\mathbf{k}_0 \cdot \mathbf{x}\right)\rangle. \tag{2.5}$$

Sometimes Eq. 2.3 is also called the Debye-Waller factor, or consequently the Lamb-Mößbauer factor is called Debye-Waller factor; but in fact both are approximations of the phase factor for different timescales of scattering.

To carry out an actual calculation of f_{LM} the density of states of phonons is needed, and in most cases the Debye-model is applied. The Lamb-Mößbauer factor follows as (see p. 11 in [GG71]):

$$f_{LM}(T) = \exp\left(-\frac{\hbar^2 k^2}{2M} \cdot \frac{3}{2k_B\Theta_D}\left[1 + 4\left(\frac{T}{\Theta_D}\right)^2 \cdot \int_0^{\Theta_D/T} \frac{x\,\mathrm{d}x}{e^{x-1}}\right]\right). \tag{2.6}$$

It follows that the Lamb-Mößbauer factor is close to 1 in case of *high nuclei-mass* and *low γ-energy*, both reducing the recoil-energy, and of course for *low temperature*. For practical purposes in most cases [2] γ-energies up to 30 keV are being used, e.g. ^{57}Fe at 14.4 kev, ^{119}Sn at 23.9 keV, ^{151}Eu at 21.5 keV, ^{161}Dy at 21.5 keV [Weg65] [Sch02].

(2.6) can be expanded for T $\ll \Theta_D$ to

$$f_{LM}(T \ll \Theta_D) \approx \exp\left(-\frac{\hbar^2 k^2}{2M} \cdot \frac{3}{2k_B\Theta_D}\left[1 + 4\left(\frac{\pi T}{\Theta_D}\right)^2\right]\right). \tag{2.7}$$

The recoilless fraction at 0 K is

$$f_{LM}(0) = \exp\left(-\frac{\hbar^2 k^2}{2M} \cdot \frac{3}{2k_B\Theta_D}\right), \tag{2.8}$$

and essentially depends upon the ratio of the recoil-energy $\frac{\hbar^2 k^2}{2M} = E_{recoil}$ versus the typical phonon energies $k_B\Theta_D = \hbar\omega_D$.

But a high Lamb-Mößbauer factor is not the only parameter effecting a successful application of the Mößbauer-effect: E.g. ^{73}Ge has a low γ-energy of 13.5 keV, a large lifetime of 4 μs and reasonable natural abundance. But its internal conversion factor (the number of nuclei decaying via internal conversion per nuclei decaying via emission of a γ-quantum) of $\alpha = 3600$ means

[2] There exist also Mößbauer nuclei with higher energies, e.g. ^{61} Ni at 67.41 keV, ^{67} Zn at 93.32 keV, ^{197}Au at 77 keV, etc. ...

that almost all excited nuclear states relax by ejection of a core electron instead of emitting γ-quanta again. This reduces the resonant cross-section $\sigma(E)$:

$$\sigma(E) = \sigma_0 \frac{(\Gamma_{nat}/2)^2}{(E_\gamma - E)^2 + (\Gamma_{nat}/2)^2}. \tag{2.9}$$

Here σ_0 is

$$\sigma_0 = \frac{2\pi}{k^2} \frac{2I_e + 1}{2I_g + 1} \frac{1}{1+\alpha}, \tag{2.10}$$

with I_e,I_g being the quantum numbers of the nuclear spin and α the internal conversion coefficient.

2.2 *Mößbauer spectroscopy*

The first application of the Mößbauer effect was undoubtedly spectroscopy. With his first experiments Mößbauer himself was able to measure the linewidth of the ^{191}Ir-transition, and thereby the lifetime of the excited state.

The extreme energy resolution of nuclear states (e.g. $\Delta E/E = \frac{4.66\times10^{-9}eV}{14411eV} \approx 3\times10^{-13}$ in case of ^{57}Fe) is unsurpassed by any other spectroscopic method known today. E.g. modern high-resolution monochromators select X-rays with $\Delta E > 100$ μeV, leading to $\Delta E/E \approx 1 * 10^{-8}$. Laser light of 7 eV photon energy can be monochromatized down to 0.1 meV, corresponding to $\Delta E/E \approx 5 \times 10^{-5}$ or better. In case of neutrons ΔE can be as low as 1μeV, but the corresponding energies of neutrons are only several meV. In the famous Pound-Rebka-Snider experiment [PR60] applying the Mößbauer effect, the minute Einstein shift of an photon "falling" in the gravitational field of the earth ($\Delta E/E \approx 5 \times 10^{-15}$!) was measured and proven to be in very good agreement with predictions of general relativity; the energy shifts measured were of the order of 0.035 neV.

Energy shifts in the order of neV can be realized by Doppler drives; since moving the source with speeds in the order of mm/s already shifts the γ-energy in the order of Γ_{nat} this can easily be achieved. Conversion into energy depends upon the energy E_γ of the used Mößbauer transition:

$$\Delta E = \frac{v}{c} E_\gamma. \tag{2.11}$$

Thereby the γ-quanta emitted by the source can be shifted to measure an energy spectrum of a resonant absorbing sample. This of course requires the sample to contain a reasonable amount of resonant nuclei, and to meet the other requirements (like low temperature etc.) to achieve a high f_{LM} in order to carry out experiments in finite times. We also implicitly assumed that the source radiates a single line, for simplicity. Multi-line sources would be possible and have been used, but analysis of the gained spectra is tedious.

There exist several possibilities to detect the increase in resonant absorption in the sample. In most cases the decrease of transmission is measured e.g. by a NaI-detector, but it is also possible to detect scattered γ-quanta, or emitted electrons or X-rays following internal conversion.

2.3 Nuclear resonant forward scattering

Instead of using a radioactive source as in the case of Mößbauer spectroscopy a nuclear resonant sample can also be excited with a short pulse of synchrotron radiation (SR). In this case, *all* possible transitions between hyperfine states are excited simultaneously, in contrast to Mößbauer-spectroscopy, where one wishes to use nuclear γ-quanta to induce single transitions only. The radiated waves are fully coherent during the whole collision process [BD64], which can last up to several μs. Due to this coherence the scattering amplitudes of all nuclei interfere. This state, the delocalized excitation of an ensemble of nuclei by a single γ-quantum, is called a ***nuclear exciton***. The creation and annihilation of a nuclear exciton is done by summing over all absorption and emission probabilities.

The probability waves corresponding to emission suffer a phase-shift depending on their direction and the relative position of the radiating nucleus. In single crystals they interfere constructively to form nuclear bragg reflections [BC63]. As a consequence of this constructive interference the decay of a nuclear exciton is enhanced into these directions. In amorphous matter only the enhancement of the (0 0 0)-reflection, the so-called nuclear resonant forward scattering ***(NFS)*** exists. Here only the signal in the forward direction channel is enhanced significantly compared to coherent scattering into 4π.

In a thick sample the absorption line is first saturated (absorption ≈ 1) in the central part. The relative absorption in the wings of the line profile increases, leading to a broader absorption line profile. Since the line width is connected with the life time of the nuclear state by the Heisenbergs uncertainty principle, we observe a ***speed up*** of the decay for short times. Due to the interaction of the reformed electromagnetic wave and the ensemble of nuclei a ***dynamic beating*** forms.

Additionally the re-emitted radiation of the different hyperfine states is coherent, giving rise to the so-called ***quantum beating***.

2.4 Theory of nuclear resonant scattering

Both Mößbauer spectroscopy and NFS can be described in a theory of nuclear resonant scattering according to Smirnov and Kohn [SK95] [KS98]. To derive a time-dependent description of nuclear resonant scattering in matter one starts with a plane monochromatic wave propagating into z-direction through a resonant sample positioned at $z = 0$:

$$\mathbf{E}(t, z) = \mathrm{E}(\omega) \exp\left(i(\mathbf{k} \cdot \mathbf{z} - \omega t)\right). \tag{2.12}$$

Propagation of this plane wave in matter is described by the solution of Maxwell's wave equation

$$(k^2 - k_0^2)\, \mathbf{E}(\mathbf{k}, \omega) - \mathbf{k}\,(\mathbf{k} \cdot \mathbf{E}(\mathbf{k}, \omega)) = \frac{4\pi i \omega}{c^2}\, \mathbf{j}(\mathbf{k}, \omega), \tag{2.13}$$

with k_0 being the magnitude of the wave vector in vacuum, and $\mathbf{j}(\mathbf{k}, \omega)$ the current density induced by the wave $\mathbf{E}(\mathbf{k}, \omega)$. The current density can be expressed depending on the incident wave by

$$\mathbf{j}(\mathbf{k},\omega) = \frac{c^2K^2}{4\pi i\omega}\,\chi_{00}(\mathbf{k},\omega)\,\mathbf{E}(\mathbf{k},\omega). \tag{2.14}$$

Here $\chi_{00}(\mathbf{k},\omega)$ is the total susceptibility for scattering in forward direction as indicated by the index $_{00}$. It connects the current density with the electrical field, and contains both electronic and nuclear contributions:

$$\begin{aligned}
\chi_{00}(\mathbf{k},\omega) &= \chi_{00}^{(e)}(\mathbf{k},\omega) + \chi_{00}^{(n)}(\mathbf{k},\omega), & (2.15)\\
\chi_{00}^{(e)}(\mathbf{k},\omega) &= \frac{1}{V_0K}\left(-\frac{4\pi}{K}r_0 + i\sigma_e\right), & (2.16)\\
\chi_{00}^{(n)}(\mathbf{k},\omega) &= i\frac{1}{2\tau_0}\sum_{ge} B_{ge}\,\varphi(\mathbf{k},\omega-\omega_0). & (2.17)
\end{aligned}$$

Here r_0 is the classical electron radius and σ_e the total cross section of inelastic scattering, so that the electronic susceptibility accounts for both coherent scattering into 4π and incoherent scattering. The nuclear susceptibility is expressed with $B_{ge} = \frac{8\pi}{V_0\omega^2(2I_0+1)\Gamma}\,|\langle e|\hat{j}(\mathbf{k})|g\rangle|^2$ as a summation over all transitions between ground $|g\rangle$ and excited $|e\rangle$ hyperfine states, with $\hat{j}(\mathbf{k})$ being the quantum mechanical current density operator, and the function of atomic motion $\varphi(\mathbf{k},\omega-\omega_0)$ accounting for any nuclear motion:

$$\varphi(\mathbf{k},\omega) = \int_0^\infty \exp(i\omega t\;-\;t/2\tau_0)\,F(\mathbf{k},t)\mathrm{d}t, \tag{2.18}$$

with $\tau_0 = \hbar/\Gamma$ being the lifetime of the excited nuclear state. So φ is the frequency spectrum of the nuclear decay weighted with the *self-correlation function* or *intermediate scattering function* $F(\mathbf{k},t)$, the Fourier-transform of the Van-Hove function $G(\mathbf{k},t)$, which was already used in the theory of the glass transition.

As we saw in Eq. 1.13, vibrations in amorphous matter (and generally in any solid matter) lead to a decay of $F(\mathbf{k},t)$ from 1 down to a plateau value on a timescale of picoseconds. The plateau value was identified to be the Lamb-Mößbauer-factor f_{LM}. Since there is virtually no nuclear scattering on a picosecond-timescale, we can separate the self-correlation function into the self-correlation function time-dependent on a nanosecond timescale and the time-independent Lamb-Mößbauer factor:

$$F(\mathbf{k}, t) \approx f_{LM} F_{NS}(\mathbf{k}, t). \tag{2.19}$$

With this we can rewrite Eq. 2.18 as a function of atomic motion on the timescale of nuclear scattering:

$$\varphi_{NS}(\mathbf{k}, \omega) = f_{LM} \int_0^\infty \exp(i\omega t \, - \, t/2\tau_0) \, F_{NS}(\mathbf{k}, t) \mathrm{d}t. \tag{2.20}$$

The shape of $F_{NS}(\mathbf{k}, t)$ depends upon the type of motion the particles are undertaking. In the case of free diffusion one would apply $F_{FD}(\mathbf{k}, t) = \exp\left(-D\, k^2\, t\right)$, with the Diffusion coefficient D, whereas hindered motion in a glass is better described by a stretched exponential, the so-called ***Kohlrausch***-function $F_K(\mathbf{k}, t) = \exp\left(-(\frac{t}{\tau})^\beta\right)$. Here τ is the characteristic relaxation time and β the stretching exponent which is defined to be between 0 and 1.

Now inserting Eq. 2.14 into Eq. 2.13 and solving the Maxwell-equation in the case of forward scattering leads to

$$\begin{aligned} \mathbf{E}(\omega, z) &= \mathrm{E}(\omega) \, \exp\left(i \frac{K\, z}{2} \chi_{00}(\mathbf{k}, \omega)\right) \\ &\approx \mathrm{E}(\omega) \, \exp\left(-\frac{\sigma_e}{2\, V_0}\, z\right) \, \exp\left(i \frac{K\, z}{2} \chi_{00}^{(n)}(\mathbf{k}, \omega)\right), \end{aligned} \tag{2.21}$$

where we used Eq. 2.15 - 2.17 in the last step. We neglected the electronic contribution of coherent scattering, since its total cross section is usually several orders of magnitude smaller than the photo-electric absorption, and only the small fraction scattered in forward direction is relevant in our case.

2.4.1 Frequency dependence of Mößbauer spectroscopy

Not taking into account the width of a source the frequency dependence of Mößbauer-spectroscopy may be calculated from Eq. 2.21 by

$$\begin{aligned} I_{MS}(\omega, z) &= |\mathbf{E}(\omega, z)|^2, \\ &= |\mathrm{E}(\omega, z)|^2 \,\exp\left(-K\, z\, \Im\left(\chi_{00}^{(n)}(\mathbf{k}, \omega)\right)\right), \end{aligned} \qquad (2.22)$$

with $\mathrm{E}(\omega, z) = \mathrm{E}(\omega)\,\exp\left(-\frac{\sigma_e}{2\,V_0}\, z\right)$. Thereby the electronic contributions lead to an exponential decrease due to absorption. The experimentally observable intensity in a Mößbauer-spectroscopy experiment takes the imaginary part of $\chi_{00}^{(n)}$ into account, corresponding to the real part of φ only.

2.4.2 Time dependence of nuclear resonant forward scattering

If we excite the sample with a short pulse of synchrotron radiation (SR) the excitation can be described as a superposition of a continuous band of monochromatic waves. One may assume that in the vicinity of the nuclear resonance there is no dependence of ω for the amplitude E:

$$\mathbf{E}_{SR}(z, t) = \mathrm{E}(z) \int \frac{\mathrm{d}\omega}{2\pi} \exp\left(-i\omega t\right) \exp\left(i \frac{K\, z}{2} \chi_{00}^{(n)}(\mathbf{k}, \omega)\right). \qquad (2.23)$$

To describe the ***quantum beating*** we can further assume that the influence of the self-correlation function does not depend upon the hyperfine state of the excited nucleus, only the shifts of resonance frequency have to be taken into account:

$$\chi_{00}^{(n)}(\mathbf{k}, \omega) = i \frac{1}{2\tau_0}\, \varphi(\mathbf{k}, \omega) \sum_{ge} B_{ge} \exp\left(i\omega_{ge} t\right), \qquad (2.24)$$

with ω_{ge} being the shift of the resonance frequency of the $|e\rangle \rightarrow |g\rangle$ transition with respect to the mean position of the corresponding lines.

In the case of a single quadrupole frequency Ω and a single line strength $B_{ge} = B$ the equation simplifies to:

$$
\begin{aligned}
\chi_{00}^{(n)}(\mathbf{k},\omega) &= i\frac{B}{4\tau_0}\ \varphi(\mathbf{k},\omega)\ \left[\exp\left(i\frac{\Omega}{2}t\right)+\exp\left(-i\frac{\Omega}{2}t\right)\right], \\
&= i\frac{B}{2\tau_0}\ \varphi(\mathbf{k},\omega)\ \cos\left(\frac{\Omega}{2}t\right).
\end{aligned}
\tag{2.25}
$$

The resulting intensity in the case of nuclear forward scattering (NFS) and a single quadrupole doublet is:

$$
I_{SR}(z,t) = \left|\mathrm{E}(z)\int\frac{\mathrm{d}\omega}{2\pi}\exp\left(-i\omega t\right)\exp\left(-\frac{\xi}{4\tau_0}\cos\left(\frac{\Omega}{2}t\right)\varphi_{NS}(\mathbf{k},\omega)\right)\right|^2,
\tag{2.26}
$$

where we applied Eq. 2.20 and introduced the effective thickness of a resonant sample $\xi := f_{LM}\ z\ K\ B = f_{LM}\ z\ N\ \eta\ \sigma_0$ with N being the atomic number density, η the fraction of resonant nuclei, σ_0 the nuclear absorption cross section. In contrast to Mößbauer-spectroscopy, the whole complex $\varphi(\mathbf{k},\omega)$ enters the equation.

An analytical solution of Eq. 2.26 is possible in the case of small effective thickness, thereby only taking into account the incident electromagnetic wave and neglecting the re-emitted waves. The so-called ***kinematical approximation*** consequently only describes single-scattering and is achieved by expanding the exponential into a power series. The zeroth order term is $\propto \delta(t)$ and corresponds to the attenuated transmitted beam, which is not of our interest and thereby discarded. The first order term is kept, any further terms are also neglected. In the case of a single quadrupole doublet the result is:

$$
I_{NFS}(t,z) \approx \mathrm{E}^2(z)\left(\frac{\xi}{4\tau_0}\right)^2\cdot\ \exp(-t/\tau_0)\ \cos^2(\frac{\Omega}{2}t)\ F_{NS}^2(\mathbf{k},t).
\tag{2.27}
$$

In this approximation the solution separates into a thickness-dependent amplitude, the product of the exponential decay, and the decay of the self-correlation function describing the time-dependence. The exponential decay is caused by the spontaneous emission of quanta by the excited nuclei and is completely determined by the width of the corresponding nuclear level. Therefore the self-correlation function or, respectively, the Van-Hove function can be measured by nuclear forward scattering of synchrotron radiation.

An analytical solution of Eq. 2.26 for ***arbitrary thicknesses*** results in [SFA+02]

$$I_{NFS}(t,z) = \mathrm{E}^2(z)\, \left(\frac{\xi}{4\tau_0}\right)^2 \cdot\, \exp(-t/\tau_0)\, \cos^2(\frac{\Omega}{2}t)\, F_{NS}(\mathbf{k},t)^2\, R^2(t), \quad (2.28)$$

were $R^2(t)$ describes the influence of multiple scattering, but $R^2(t)$ and $F^2_{NS}(\mathbf{k},t)$ can not be separated without further assumptions. In the case of negligible effective thickness (as assumed in the kinematical approximation) $R(t) = 1$. In the case of negligible molecular motion ($F_{NS} = const.$) $R(t)$ was calculated to be [KS99]

$$R(t) = \frac{J_1(\xi t/\tau_0)}{\sqrt{\xi t/\tau_0}}, \quad (2.29)$$

which leads to the so-called ***dynamic beats***. But still when the sample thickness is too large to separate $R(t)$ and $F_{NS}(t)$ in the complete time range, one can approximate the influence of $R(t)$ in the time window where $\xi t/\tau_0$ is small as $R^2(t) = \exp(-\xi t/\tau_0)$. This additional decay factor for short times is the so-called ***speed-up effect*** introduced by the broadening of the absorption line.

The two Fourier transforms in Eq. 2.26 and Eq. 2.18 can also be calculated numerically using standard fast-Fourier-transform algorithms. In this case we also take multiple-scattering effects into account.

2.5 Hyperfine Interactions

Since nuclear resonant techniques can explore neV-energy shifts they are perfectly suited to investigate *hyperfine interactions*, the interactions between the electronic shell and the nucleus. These are in particular the *isomer shift*, the *quadrupole splitting*, the *magnetic hyperfine structure* and the *quadratic Doppler effect*.

To calculate the spectra of bound electrons one usually assumes a point-like nucleus. Both isomer shift and quadrupole splitting correct for size-effects of the nucleus being caused by the extent of the nuclear charge density ρ and its interaction with the electrons moving in its potential Φ. Taylor-expansion of Φ yields:

$$
\begin{aligned}
V &= \int \rho\, \Phi\, \mathrm{d}\mathbf{x}, \\
&\approx eZ\, \Phi_{x=0} + \frac{1}{2} \sum_{i\,j} \frac{\partial^2 \Phi}{\partial x_i \partial x_j}|_{\mathbf{x}=0} \int \rho\, x_i\, x_j \mathrm{d}\mathbf{x}.
\end{aligned}
\tag{2.30}
$$

The first term reflects the potential energy of a point-like nucleus in the electronic potential, resulting in an overall shift of the energy. The linear terms of the Taylor-expansion vanish, because nuclei can not have a dipole moment, so the quadratic term is the first non-trivial shift in energy. We can diagonalize it without any loss of generality. Since $-\nabla\Phi = \mathbf{E}$ we can identify $\frac{\partial^2\Phi}{\partial^2 x_i}|_{\mathbf{x}=0} = -\frac{\partial E_i}{\partial x_i}|_{\mathbf{x}=0} =: \partial_i E$ as the elements of the *gradient of the electric field* (EFG) at the nuclear position:

$$
V_{quadratic} = \frac{1}{2} \left[\sum_i \partial_i E \int \rho\, x_i^2\, \mathrm{d}\mathbf{x} \right]. \tag{2.31}
$$

Now one can split the sum into an isotropic and a traceless part. As we will see, the isotropic part of the EFG $\partial_i E_{iso}$ is produced by the contribution of s-electrons, the contributions of all other electrons are contained in the traceless part $\partial_i E_{tl}$:

$$
V_{quadratic} = \frac{1}{2} \sum_i \partial_i E_{iso} \int \rho\, \frac{r^2}{3}\, \mathrm{d}\mathbf{x} + \partial_i E_{tl} \int \rho \left(x_i^2 - \frac{r^2}{3} \right) \mathrm{d}\mathbf{x}. \tag{2.32}
$$

The first term yields the ***isomer shift***, the second leads to the ***quadrupole splitting***.

2.5.1 Isomer shift

We can evaluate the first term with aid of the Poisson equation:

$$\sum_i \partial_i E_{iso} = \Delta\Phi = 4\pi\, e\, |\Psi(0)|^2, \tag{2.33}$$

with $|\Psi|^2$ being the probability density of the electrons. Since the electronic states close to the nucleus decay $\propto r^l$, only s-electrons contribute in this case.

$$V_{isomer} = \frac{2\,\pi\, e}{3}\, |\Psi(0)|^2 \int \rho\, r^2\, \mathrm{d}\mathbf{x}. \tag{2.34}$$

The integral can be understood as a mean nuclear radius weighted by the charge density:

$$\int \rho\, r^2\, \mathrm{d}\mathbf{x} = Z\, e\, < r^2 > . \tag{2.35}$$

Because the charge density throughout the nucleus is in good approximation homogenous, this mean radius can be directly connected to the nuclear radius by $< r^2 >= \frac{3}{5} r^2$. Since the nuclear radius is dependent on the nuclear state an energy shift is connected to the transition between nuclear states:

$$\Delta V = \frac{2\,\pi\, Z\, e^2}{3}\, |\Psi(0)|^2\, (< r_e^2 > \,-\, < r_g^2 >). \tag{2.36}$$

A γ-quantum emitted by nucleus E gains the energy shift ΔV_E, and loses ΔV_A when being absorbed by nucleus A. This shift is called ***isomer shift***:

$$\delta = \Delta V_E - \Delta V_A = \frac{2\,\pi\, Z\, e^2}{3}\, (|\Psi_E(0)|^2 - |\Psi_A(0)|^2)\, (< r_e^2 > \,-\, < r_g^2 >). \tag{2.37}$$

In the simplest case both the emitting and the absorbing nuclei are identical in all their nuclear and chemical properties, e.g. $(|\Psi_E(0)|^2 - |\Psi_A(0)|^2)$

vanishes; in this case $\delta = 0$. Now measuring the absorbing nucleus in a different chemical environment leads to $(|\Psi_E(0)|^2 - |\Psi_A(0)|^2) \neq 0$ and thereby introduces a measurable shift $\delta \neq 0$ of the γ-energy. The isomer shift is thereby *sensitive to the chemical state* and environment of the excited isotope[3].

2.5.2 Quadrupole splitting

Stepping back to the traceless part from Eq. 2.32, the quadrupole term:

$$V_{quadrupole} = \frac{1}{6}\partial_i E_{tl} \int \rho \left(3x_i^2 - r^2\right) \mathrm{d}\mathbf{x}. \tag{2.38}$$

Since the isotropic EFG-tensor was reduced to a scalar value in the sum in Eq. 2.33, the traceless EFG-tensor $\partial_i E_{tl}$ is usually referred to as ***the* EFG-tensor**. The EFG-tensor was already diagonalized during the initial approach, its diagonal components are usually labeled V_{ii}. Since the EFG-tensor is a traceless second rank tensor, its major axes components fulfill the condition

$$\sum_i T_{ii} = 0. \tag{2.39}$$

We can without any loss of generality assume that V_{zz} is the major component. The ratio of V_{yy} and V_{xx} is usually expressed with aid of the *asymmetry parameter* η:

$$\eta = \frac{V_{xx} - V_{yy}}{V_{zz}}. \tag{2.40}$$

η is positive and between 0 and 1 if and only if $|V_{zz}| > |V_{yy}| \geq |V_{xx}|$, as it is generally defined in the literature . When given values for V_{zz} and η, we can calculate the remaining EFG-components with Eq. 2.39 and 2.40. Of importance is the case of cylindrical symmetry, in this case $|V_{yy}| = |V_{xx}|$.

[3] Since the same arguments also apply to the chemical environment of the emitting nuclei, one has always to state to which reference isomer shifts are measured.

The integral in Eq. 2.38 accounts for the *deviation from spherical symmetry* of the nucleus, it defines the *nuclear quadrupole tensor*:

$$e\,Q_{ii} := \int \rho \left(3x_i^2 - r^2\right) \mathrm{d}\mathbf{x}. \tag{2.41}$$

The quadrupole term results as:

$$V_{quadrupole} = \frac{e}{6} \sum_i V_{ii}\, Q_{ii}. \tag{2.42}$$

Now we can see that this hyperfine interactions is essentially due to a coupling of the quadrupole tensor Q_{ii} of the nucleus with the electric field gradient V_{ii} produced by the surrounding electrons: The orientation of the nuclear spin in an electric field gradient results in minute energy shifts due to its quadrupole interaction. Any contribution by s-electrons to the EFG-gradient would be rotationally symmetric and thereby could not cause any change in energy. The Q_{ii} can be expressed with aid of nuclear spin operators (p. 55 in [GG71]):

$$e\,Q_{ii} = Q \frac{1}{2I(2I-1)}\,\mathbf{I}_i^2. \tag{2.43}$$

Here Q is the quadrupole tensor magnitude, called the *nuclear quadrupole moment*. The corresponding Hamiltonian is

$$\mathcal{H}_{quadrupole} = \frac{e\,Q}{2I\,(2I\,-\,1)}\,(V_{zz}\mathbf{I}_z^2 \,+\, V_{yy}\mathbf{I}_y^2 \,+\, V_{xx}\mathbf{I}_x^2). \tag{2.44}$$

Using Eq. 2.40 and shift operators of the nuclear spin $\mathbf{I}_+/\mathbf{I}_-$, this can be written as

$$\mathcal{H}_{quadrupole} = \frac{e\,V_{zz}\,Q}{4I\,(2I\,-\,1)}\left[3\,\mathbf{I}_z^2 \,-\, I(I+1) \,+\, \frac{\eta}{2}(\mathbf{I}_+^2 + \mathbf{I}_-^2)\right]. \tag{2.45}$$

Because only nuclei with a spin quantum number $I > \frac{1}{2}$ have non-spherical charge densities the quadrupole moment vanishes for all nuclei with

$I \leq \frac{1}{2}$. Additionally, if the nuclear site has cubic symmetry the three axes x_i are interchangeable, thus the V_{ii} have to be identical and thereby the bracket in Eq. 2.44 vanishes.

In case of $I = \frac{3}{2}$ and $\eta = 0$, the shift of energy caused by this Hamiltonian is

$$< I_z' | \mathcal{H}_{quadrupole} | I_z >= \begin{cases} |I_z| = \frac{3}{2} & \Rightarrow \quad +\frac{(e\,V_{zz}\,Q)}{4} \\ |I_z| = \frac{1}{2} & \Rightarrow \quad -\frac{(e\,V_{zz}\,Q)}{4} \end{cases}, \tag{2.46}$$

thereby splitting the line into two components, the separation energy being $\Delta E_Q = \frac{(e\,V_{zz}\,Q)}{2}$ usually called ***quadrupole splitting***. In energy spectra this splitting manifests as a quadrupole doublet separated by ΔE_Q, in time spectra a quadrupole frequency $\hbar \Delta E_Q$ is observed.

If the EFG-components V_{yy} and V_{xx} are identical ($\eta = 0$), they do not contribute to the quadrupole energy, whereas in the case of extreme asymmetry ($\eta = 1$) they may change the result of Eq. 2.46 by up to 16%; the more general formula is $\Delta E_Q = \frac{eV_{zz}Q}{2}\sqrt{1 + \eta^2/3}$.

In general both excited and ground state can be quadrupole split. In the case of ^{57}Fe the ground state has $I = \frac{1}{2}$ and lacks a quadrupole splitting, so only the excited state with $I = \frac{3}{2}$ is split. Since above 1 K the nuclear states with m= -3/2, -1/2, 1/2, 3/2 are equally populated, we observe two equally strong lines corresponding to the states $m = \pm\frac{3}{2}$ and $m = \pm\frac{1}{2}$. In this case the isomer shift is identical with the shift of the mean position of the doublet.

2.5.3 Other hyperfine interactions

The already mentioned magnetic hyperfine structure and quadratic Doppler effect are also of great general interest. The ***magnetic hyperfine structure*** results from the orientation of the nuclear spin in a strong magnetic field, described by the Hamiltonian

$$\mathcal{H}_{Zeeman} = -\mu \cdot \mathbf{H} = -g\mu_n \mathbf{I} \cdot \mathbf{H}, \tag{2.47}$$

with H being the magnetic flux density, μ the nuclear magnetic moment, g the nuclear Landé factor and μ_n the nuclear magneton. Since in the experiments presented in this work no magnetic fields were applied, we did not observe the magnetic hyperfine structure.

The ***quadratic Doppler effect*** results from accurate relativistic treatment:

$$\nu_{rel} = \nu \left(1 - \frac{v}{c}\right) \left(1 - \frac{v^2}{c^2}\right)^{-\frac{1}{2}}. \tag{2.48}$$

The first term $\frac{v}{c}$ will usually average during the lifetime of a nuclear state. The second term is independent of the direction of v and thereby does not average out. It can be approximated by

$$\nu' = \nu \left(1 + \frac{< v^2 >}{2c^2}\right). \tag{2.49}$$

The corresponding shift of a Mößbauer line would be

$$\frac{\Delta E}{E} = \frac{\Delta \nu}{\nu} = -\frac{< v^2 >}{2c^2}. \tag{2.50}$$

In harmonic approximation this can be calculated from

$$-\frac{< v^2 >}{2c^2} = -\frac{3}{2\,M\,c^2} \sum_j A_j^2,\ \hbar\omega\,(\frac{1}{2} + n_j) \tag{2.51}$$

with ω_j the oscillation frequency, M the mass of the vibrating particle, A_j a weighting factor ($\sum_j A_j^2 = 1$) and $n_j = [\exp(\hbar\omega_j/k_B T) - 1]^{-1}$ the population of this mode.

Neglecting the zero-point motion $\frac{1}{2}\hbar\omega_j$, which is negligible in the experiments performed, in the high-temperature approximation we get (see p. 52 [GG71]):

$$-\frac{< v^2 >}{2c^2} = -\frac{3}{2}\frac{RT}{Mc^2}. \tag{2.52}$$

2.6 Coupling of molecular dynamics and hyperfine interactions

Until now only the influence of spatial dynamics on the NFS-signal has been considered. If we assume that relaxation of the nuclear spin states is independent of the spatial relaxation, then the corresponding dynamics can be expressed with the aid of separate functions. As we already saw in Eq. 2.17 the ***spatial dynamics*** is entering the formalism of NFS by the self-correlation function $F(\mathbf{k}, t)$. NFS is sensitive to spatial dynamics on a length scale of the resonant radiation, in our case $\lambda_{^{57}Fe} \approx 0.086$ nm. Any molecular motion of ≈ 0.01 nm on a time scale of the nuclear decay will lead to a loss of the coherence in forward direction. This can be detected by an increased decay rate of the NFS-signal.

The influence of the ***nuclear spin dynamics*** was omitted until now, which will be introduced now. It is assumed that the nuclear spin states are only indirectly being changed by relaxation of the surrounding of the nucleus, e.g. a change of orientation of the molecule containing the nucleus. Thereby the hyperfine interactions couple the molecular environment to the nuclear spin states. As will be shown below the already introduced factor describing a static quadrupole frequency $\cos\left(\frac{\Omega}{2}t\right)$ in Eq. 2.25 can then be seen as a limit in the case of slow fluctuation.

The following formalism was developed by Blume, Tjon [BT68], [TB68] and Dattagupta [DB74a], [DB74b], [Dat81] to name a few. In general the dynamics of the nuclear hyperfine states can be described by a ***perturbation factor*** [Dat81]

$$G_{LL'}^{MM'}(p) = \sum_{\substack{m_0 m_0' \\ m_1 m_1'}} (-1)^{2I_0+m_0+m_0'} \sqrt{(2L+1)(2L'+1)} \tag{2.53}$$

$$\times \begin{pmatrix} I_1 & I_0 & L \\ m_1 & -m_0 & M \end{pmatrix} \begin{pmatrix} I_1 & I_0 & L' \\ m'_1 & -m'_0 & M' \end{pmatrix} \langle m_0 m_1 | U_{av}(p) | m'_0 m'_1 \rangle \, .$$

Here L and L' are the corresponding values of the angular momentum of the absorbed and emitted photon, M and M' corresponds to the polarization of the photons, and G is expressed depending on the frequency p. I_1,I_0,m_1 and m_0 are the angular quantum numbers of the nuclear excited and ground state. The average time evolution function $U_{av}(t)$ and its Laplace transform $U_{av}(p)$ include all physical relevant information about the coupling of the nuclear spin states and their stochastic changes. The generalized Kubo-Anderson theory as presented below enables us to describe the influence of $U_{av}(p)$ on the nuclear susceptibility directly. Alternatively we can use $U_{av}(p)$ to calculate the perturbation factor, then do an inverse Laplace-transform to obtain $G_{LL'}^{MM'}(t)$ to insert into the above explained separation ansatz:

$$\varphi(\mathbf{k}, \omega) = \int_0^\infty \exp(i\omega t \;-\; t/2\tau_0) \, F(\mathbf{k}, t) \, G_{LL'}^{MM'}(t) \, \mathrm{d}t. \tag{2.54}$$

This enables us to fully incorporate translational and nuclear spin dynamics into our NFS-theory. The difficulty lies in the determination of the perturbation factor $G_{LL'}^{MM'}(t)$ or the average time evolution function U_{av}.

2.6.1 Kubo-Anderson theory

A first stochastic theory of motional narrowing was developed by Kubo [KT54] and Anderson [And54]. They introduced a general stochastic function $f(t)$ to formulate a time-dependent Hamiltonian:

$$\mathcal{H} = V \, f(t). \tag{2.55}$$

Here $f(t)$ is stochastically chosen from a finite set of values, e.g. $f(t) \in -1, 1$ or $\in -1, 0, 1$. $f(t)$ describes the stochastic influence of the environment, e.g. a heat bath leading to molecular motion. The potentials V_j model the hyperfine interactions. The theory requires the corresponding potentials V_j and thereby the Hamiltonian at different times to commutate

$[V_i, V_j] = 0 \rightarrow [\mathcal{H}(t'), \mathcal{H}(t)] = 0$. Thus the Hamiltonian can be diagonalized, and the different quantum-mechanical eigenstates of the Hamiltonian (designated by $|\ldots\rangle$) are not mixed due to changes of the stochastic states ($|\ldots)$) induced by jumps in $f(t)$. The Kubo-Anderson theory is consequently called the ***adiabatic theory of motional narrowing***, since only the resonance frequencies of the eigenstates are changed. For example the resonance frequencies of a system with

$$\mathcal{H} = g\,\mu\,h\,\mathbf{I}_z\,f(t), \qquad f(t) \in -1,\ 1, \tag{2.56}$$

with h being the amplitude of the applied magnetic field can be calculated with this theory, e.g. by a matrix-inversion algorithm proposed by Sack [Sac58]. But only adding a constant field component h_0

$$\mathcal{H} = g\,\mu\,\left(h\,\mathbf{I}_z\,f(t)\ +\ h_0\,\mathbf{I}_x\right), \tag{2.57}$$

leads to a mixing of eigenstates; the Kubo-Anderson theory can not be applied any more.

2.6.2 Generalized Kubo-Anderson theory

Blume [Blu68] generalized the Kubo-Anderson theory and Sacks algorithm to describe also non-adiabatic Hamiltonians like Eq. 2.57. From the general stochastic function $f(t)$ we can generate the specific stochastic functions $f_j(t)$ with exactly one being 1 and the others 0 at a given value of $f(t)$, and formulate a generalized Hamiltonian:

$$\mathcal{H} = \sum_j V_j\,f_j(t). \tag{2.58}$$

For example a ^{57}Fe nucleus in a molecule switching through three different molecular orientations (corresponding to different stochastic states) would experience a variation of the electric field gradient:

$$V_j = Q\left(3\,I_j^2\;-\;I^2\right), \qquad I_j = \begin{cases} I_x & : \quad j=-1 \\ I_y & : \quad j=0 \\ I_z & : \quad j=1 \end{cases}, \tag{2.59}$$

where I_j, I correspond to the set of angular motion operators in the stochastic state $|j)$. Since the ground state of the ^{57}Fe nucleus has spin $I = \frac{1}{2}$ its quadrupole moment Q vanishes, and thereby only the excited nuclear state with $I = \frac{3}{2}$ shows a quadrupole splitting. From the general stochastic function $f(t) \in -1, 0, +1$ we can build the specific stochastic functions

$$\begin{aligned} f_{-1}(t) &= \frac{1}{2}\,f(t)\,[f(t)-1], \\ f_0(t) &= 1\;-\;f^2(t) \\ f_{+1}(t) &= \frac{1}{2}\,f(t)\,[f(t)+1]. \end{aligned} \tag{2.60}$$

In each stochastic $|j)$ state a different set of hyperfine states exist. In this case every orientation of the molecule corresponds to another quantization axis leading to a different set of the nuclear hyperfine states.

The nuclear susceptibility (see Eq. 2.17) can be expressed with the aid of the generalized Hamiltonian Eq. 2.58:

$$\chi(\omega)^{(n)} \propto \int\limits_0^\infty \exp(i\omega t - \frac{t}{2\tau_0})\left\langle\left(\mathcal{H}^{(-)}\mathcal{H}^{(+)}(t)\right)_{stoch}\right\rangle_{HFI}, \tag{2.61}$$

where $\langle\ldots\rangle_{HFI}$ denotes summing over the occupation of all different hyperfine states and $(\ldots)_{stoch}$ means summing over all stochastic states introduced by $f(t)$. $\mathcal{H}^{(-)}$ and $\mathcal{H}^{(+)}$ are the annihilation and creation operators, and $\mathcal{H}^{(+)}(t)$ is the corresponding Heisenberg operator:

$$\mathcal{H}^{(+)}(t) = \exp\left[i\int\limits_0^t \mathcal{H}(t')\mathrm{d}t'\right]\,\mathcal{H}^{(+)}\,\exp\left[-i\int\limits_0^t \mathcal{H}(t')\mathrm{d}t'\right]. \tag{2.62}$$

This term can be simplified by use of the ***Liouville operator*** (designated by $^\times$) which is defined by

$$A^\times B := [A, B]. \tag{2.63}$$

The Liouville operator can be expressed as a matrix with four dimensions (labeled by $\mu\nu\mu'\nu'$), thereby it corresponds to a *superoperator*, an operator working on operators. It can be shown that (see Appendix in [Blu68]):

$$\langle\mu\nu|A^\times|\mu'\nu'\rangle = \delta_{\nu\nu'}\langle\mu|A|\mu'\rangle - \delta_{\mu\mu'}\langle\nu'|A|\nu\rangle. \tag{2.64}$$

Especially the Liouville operator of the Hamiltonian has an important physical significance: Its eigenvalues are the differences of the energy eigenvalues of the Hamiltonian, corresponding to the possible spectral lines of the system. It has the important property to disentangle the integrations introduced in the Heisenberg operator:

$$\exp(A)\, B\, \exp(-A) = \exp(A^\times)B. \tag{2.65}$$

The averaging term in Eq. 2.61 can consequently be written as

$$\left(\left\langle\mathcal{H}^{(-)}\mathcal{H}^{(+)}(t)\right\rangle_{HFI}\right)_{stoch} = \left\langle\mathcal{H}^{(-)}\left(\exp\left[i\int_0^t\mathcal{H}^\times(t')\mathrm{d}t'\right]\right)_{stoch}\mathcal{H}^{(+)}\right\rangle_{HFI} \tag{2.66}$$

The ordering of the stochastical and the quantum-mechanical averaging may be changed since we assumed that the environment only indirectly affects the nuclear states by introducing the jumps of the specific stochastic functions $f_j(t)$. The crucial part is the evaluation of the central term $\exp\left[i\int_0^t\mathcal{H}^\times(t')\mathrm{d}t'\right] =: U(t)$. $U(t)$ describes the time-development of the system under observation under influence of instantaneous changes in the stochastic states. We assume that the jump process of $f(t)$ in $\mathcal{H}^\times(t')$ governing the transition from one stochastic state to another is ***stationary*** and ***Markovian***. Then we can write $U(t)$ as a *time ordered series*:

$$
\begin{aligned}
(i|U(t)|j) \;=\; & \sum_{k\,l\,\ldots\,z} \exp(i\,V_i^{\times}\,t_i)\,\mathcal{J}_{ik}\,\exp(i\,V_k^{\times}\,(t_k-t_1))\,\mathcal{J}_{kl}\,\cdots \\
& \cdots\,\exp(i\,V_y^{\times}\,(t_y-t_x))\,\mathcal{J}_{yz}\,\exp(i\,V_z^{\times}\,(t_z-t_y))\,\mathcal{J}_{zj}.
\end{aligned} \tag{2.67}
$$

Here the $V_j^{\times}$ are the Liouville operators operating on the interaction potentials V_j, and $\mathcal{J}_{ij} = (i|\mathcal{J}|j)$ is the probability of an instantaneous jump from the stochastic state $|i)$ into $|j)$:

$$(i|\mathcal{J}|j) =: p_{ij}. \tag{2.68}$$

The matrix $(i|\mathcal{J}|j)$ is connected with the matrix of jump rates $(i|W|j) := \lambda\,((i|\mathcal{J}|j) - (i|\mathbf{1}|j))$ with λ the time scale of jump rates. We may further assume in the ***strong collision model*** or the so-called ***random phase approximation*** that the matrix element $(i|\mathcal{J}|j)$ does not depend on the initial state $|i)$, only on the final state $|j)$:

$$(i|\mathcal{J}|j) =: p_j. \tag{2.69}$$

This is equivalent with the requirement for ***detailed balance*** in thermal equilibrium:

$$p_j\,(j|\mathcal{J}|i) = p_i\,(i|\mathcal{J}|j). \tag{2.70}$$

Detailed balance thereby reduces the degrees of freedom of the $\mathcal{J}$ matrices. Eq. 2.70 can also be applied to the matrix of jumprates W. Further reduction of degrees of freedom is achieved by ***conservation of total probability*** $\sum_j (i|W|j) = 0$. As a consequence the diagonal elements of $(i|W|i)$ contain the inverse negative lifetimes of the states $|i)$.

To calculate the stochastic average of Eq. 2.67 the time-ordered series was splitted by Blume [Blu68] into two processes: A restricted averaging over a sub-ensemble $U_{av}(t)$ and then a weighted summation over all possible sub-ensembles $(i|j)$:

$$(U(t))_{stoch} = \sum_{ij} p_i \, (i|U_{av}(t)|j). \tag{2.71}$$

The restricted average of $U(t)$ in Eq. 2.67 is introduced by multiple time integrations:

$$\begin{aligned} U_{av}(t) \;&=\; \sum_{s=0}^{\infty} \int_0^t \mathrm{d}t_s \int_0^{t_s} \mathrm{d}t_{s-1} \cdots \int_0^{t_2} \mathrm{d}t_1 \exp((i\,\mathcal{H}^\times - \lambda)\, t_1)\, (\lambda \mathcal{J}) \;\cdots \\ &\cdots\; (\lambda \mathcal{J})\; \exp((i\,\mathcal{H}^\times - \lambda)\,(t - t_s)). \end{aligned} \tag{2.72}$$

This time ordered series can be solved by Laplace transformation:

$$\begin{aligned} \sum_{ij} p_i \, (i|U_{av}(p)|j) \;&=\; \sum_{ij} p_i \, (i| \left[\sum_{s=0}^{\infty} (p + \lambda - i\mathcal{H}^\times)^{-1} [\lambda \mathcal{J} (p + \lambda - i\mathcal{H}^\times)^{-1}]^s \right] |j), \\ &=\; \sum_{ij} p_i \, (i| \left[\sum_{s=0}^{\infty} (p - W - i \sum_{j'} V_{j'}^\times) F_{j'} \right]^{-1} |j). \end{aligned} \tag{2.73}$$

The $f_j(t)$ enter the solution via matrices $F_j(t)$ the trace of which contains the values of $f_j(t)$ and are 0 elsewhere (in other words $(i|F_j(t)|k) = \delta_{ji}\delta_{jk}$). This general formula can be simplified significantly with the random phase approximation from Eq. 2.69.

$$(U(p))_{stoch} = [(U^0(p+\lambda))_{stoch} - \lambda]^{-1}, \tag{2.74}$$

with

$$(U^0(p+\lambda))_{stoch} = \sum_j p_j \, [(p + \lambda) - i\, V_j^\times]^{-1}. \tag{2.75}$$

Inserting the inverse Laplace transform of Eq. 2.73 or 2.74 into Eq. 2.66 and Eq. 2.61 now describes the influence of stochastic changes of the Hamiltonian on the resonance frequencies. The main effort to calculate these is the inversion of the matrix in Eq. 2.73. This matrix is indexed by the quantum numbers of the ground and excited state in addition to the n indices formed by the different stochastic states. Consequently the matrix has a dimension of $(2I_0+1)(2I_1+1)\,n$. In the example of the rotating molecule as shown in Eq. 2.59 one would have to invert an $2 \cdot 4 \cdot 3$ matrix.

Should the Hamiltonians V_j commutate like assumed in the Kubo-Anderson formalism, then the corresponding Liouville operators $V_j^\times$ are simple scalars, and the matrix to be inverted can be reduced to dimension of n, yielding the result from Sack. This is prohibited in any other case, since the $V_j^\times$ then induce transitions between quantum mechanical states, thereby introducing off-diagonal elements.

2.6.3 Isotropic fluctuation of the electric field gradient

Many physical processes can be modelled by the generalized Kubo-Anderson theory as presented above, e.g. jumps of nuclei between lattice sites with different hyperfine parameters, fluctuating magnetic fields and/or fluctuating electric field gradients.

Analytical solutions, e.g. of the relaxation rate dependence of the resonance frequencies, are in most cases impossible due to the complex interaction of stochastic and quantum mechanical degrees of freedom. Blume and Tjon [TB68] were nevertheless able to invert the matrix Eq. 2.73 analytically in the case of the Hamiltonian Eq. 2.59 under the assumptions of

1. a ^{57}**Fe-like spin structure** $(I_0 = 1/2, I_1 = 3/2)$,
2. a **powdered sample**, thereby neglecting any polarization and direction dependence,

3.(a) a **completely isotropic** mechanism of EFG-fluctuations ($p_i = p_j = p_k = 1/3$ and $W_{ij} = W_{ji} =: W$).

The mechanism of EFG-fluctuations is in this case completely characterized by the value of the jump rate W:

$$
\begin{aligned}
(U(p))_{stoch} &= \frac{p+3W}{p^2+3Wp+(\Omega/2)^2}, \qquad (2.76)\\
&= \frac{p+3W}{(p+\frac{3}{2}W - i\,\frac{1}{2}\sqrt{\Omega^2-9W^2})(p+\frac{3}{2}W + i\,\frac{1}{2}\sqrt{\Omega^2-9W^2})},
\end{aligned}
$$

with Ω being the quadrupole splitting caused by the static EFG. In the absence of relaxation ($W = 0$) they obtained two lines separated by the static quadrupole splitting (see Fig. 2.2 (left)). The two terms $\frac{3}{2}W$ lead to an **increase of the width** of both lines with increasing W (see Fig. 2.2 (second to the left)). This corresponds to a decrease of the life time of the excited state due to slow mixing. Additionally the imaginary parts start to cause a **shift of the resonance** frequencies.

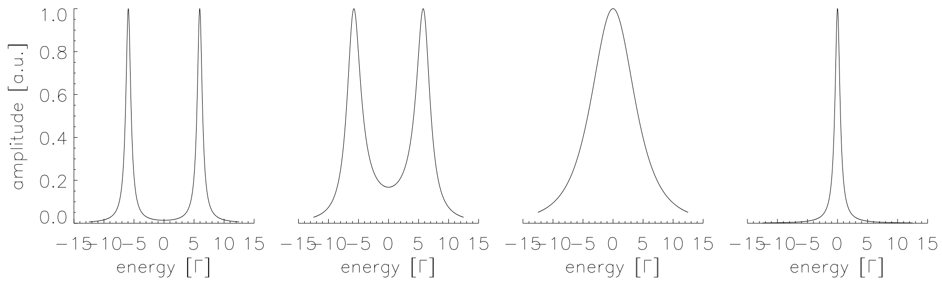

Figure 2.2: Ideal energy spectra of an ^{57}Fe-nucleus as found in ferrocene for case 3.(a). Relaxation rates are $3W = 0\Omega, 0.15\Omega, 1.0\Omega, \infty$ from left to right.

At $3W = \Omega$ the whole quadrupole splitting has been destroyed, both resonance frequencies are now identical, and the broadening of the line is at its maximum (see Fig. 2.2 (third to the left)). A further increase of W will cause the square root term to change from imaginary to real values, thereby starting to **reduce the width**. For large values $3W \gg \Omega$ follows $(U(p))_{stoch} \approx \frac{1}{p}$, leading to a single line without any quadrupole splitting or additional line broadening (see Fig. 2.2 (right)). This corresponds to a rapid rotation of the EFG, which the nucleus can not follow any more. The nucleus only observes an **average EFG**, which is zero in the case of complete isotropic rotation. This reduction of the quadrupole splitting induced by fluctuating EFGs is called ***motional narrowing***.

2.6.4 Anisotropic fluctuation of the electric field gradient

Gibb [Gib76] calculated solutions for different models of anisotropic fluctuations while keeping assumptions 1. and 2. (for detailed formulas please see original work):

3.(b) A **unique axis z** and **isotropic fluctuation in the x-y-plane**. Thereby $W_{xy} \neq W_{xz} = W_{yz}$, and $p_x = p_y \neq p_z$. The system is defined by p_z, W_{xy}, W_{xz} with the additional elements of $(i|W|j)$ following from detailed balance (Eq. 2.70) and conservation of probability.

3.(c) **Unique axis** and **anisotropic fluctuation in the x-y plane**. Here $W_{xz} \to 0$ was assumed, and the fluctuations in the x-y plane is anisotropic ($p_x \neq p_y$).

3.(d) **Completely anisotropic fluctuations**. In this case six parameters are needed to determine the fluctuation: p_x, p_y, p_z and three jump rates from the W-matrix, the remaining parameters again being fixed by detailed balance and conservation of probability.

To discuss these cases we first neglect the influence of the occupation parameters (we assume $p_x = p_y$). In case 3.(b) we can discriminate between $W_{xy} \ll W_{xz}$ and $W_{xy} \gg W_{xz}$. When $W_{xy} \ll W_{xz}$, there are fast fluctuations of the EFG into and out of the direction of the unique axis, only the fluctuation in the x-y plane is hindered. But since a transition from $|x) \to |y)$ can still occur via $|z)$ we will not notice strong differences from case 3.(a).

When $W_{xy} \gg W_{xz}$, there will be faster fluctuations in the x-y-plane than into and out of the z-direction. In the case of fast fluctuations ($W_{xy} \gg \Omega$) we will thereby only observe a partial averaging of the total quadrupole splitting, resulting in a **reduced quadrupole splitting** at intermediate values of W. If the asymmetry parameter $\eta = 0$ then the maximal reduced quadrupole splitting is $\Omega_{reduced} = 0.5\Omega$ and has negative sign (this corresponds to averaging out e.g. of V_{zz}, V_{yy} or V_{xx}). Finally, the quadrupole splitting collapses completely into a single line (see Fig. 2.3):

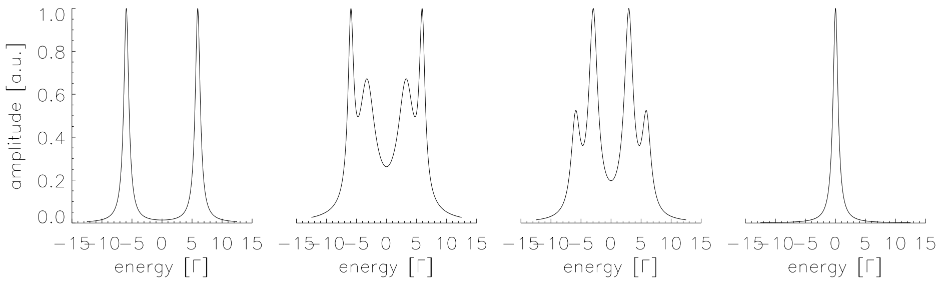

Figure 2.3: Ideal energy spectra of an ^{57}Fe-nucleus as found in ferrocene for case 3.(b). In contrast to Fig. 2.2 W_{xy} was increased by a factor of 20 and $W_{xz} = W_{yz}$ was decreased by a factor of 20.

If there are further differences in the occupational parameters $p_x = p_y \neq p_z$ (as in assumption 3.(c)) the final collapse is not complete, because not all components average out (see Fig. 2.4(right)), causing a **residual quadrupole splitting**:

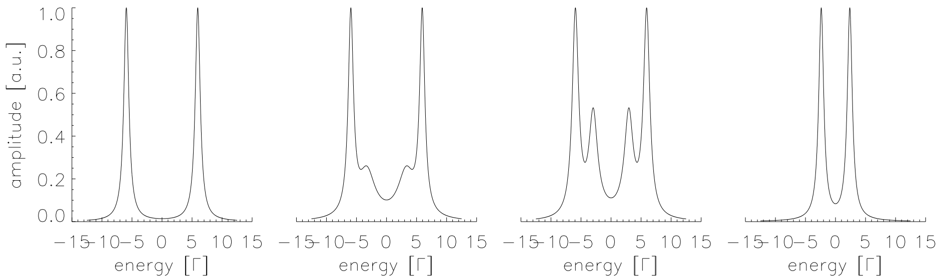

Figure 2.4: Ideal energy spectra of an ^{57}Fe-nucleus as found in ferrocene for case 3.(c). Unlike in Fig. 2.3 the occupational parameters were changed from $p_x = p_y = p_z = 1/3$ to $p_x = p_y = 0.2$ and $p_z = 0.6$

Blume mentioned that algebra was getting "straightforward but tedious" in the case of purely isotropic relaxation. Gibb cites formulas for the case 3.(c), but states that algebra in the case of full anisotropic fluctuation was "formidable", and did not attempt the calculation.

All these analytical solutions apply to powdered samples only. To describe the angular dependence of any fluctuations one has to resort to numerical algorithms instead of analytical solutions.

2.7 Small Angle X-ray Scattering

Small Angle X-ray Scattering (short: **SAXS**) is a technique to study the properties of materials which exhibit inhomogeneities in the electron density on a length scale exceeding the X-ray wavelength. Since scattering laws exhibit a reciprocal dependence of the scattering angle and the dimension of the scatterer, the X-rays are scattered at small angles.

SAXS is a method used routinely nowadays, so only the important features and formulas (for our case) are presented.

2.7.1 SAXS by a cylindrical pore

Due to Babinets principle SAXS can not depend on the electron-density, it only depends on *differences* of the electron density. Thereby the SAXS-signal of a homogenous bulk sample containing cylindrical pores is identical to the signal of rod-like particles [GO82]. The scattered amplitude is related to the sample by:

$$F(q) = \int \mathrm{d}V \rho(\mathbf{r}) \exp(-i\, \mathbf{q} \cdot \mathbf{r}). \tag{2.77}$$

Here ρ is the electron density, $\mathbf{q}$ is the scattering vector and $\mathbf{r}$ the position vector. The integration extends over the coherently illuminated sample volume V. Exploiting the axial symmetry of a pore/rod the integral can be split into a radial integral and an integral along the z-axis.

$$F(q) = \Delta\rho \int \mathrm{d}z\ \exp(-i\, \mathbf{q} \cdot \mathbf{r}_z) \int \mathrm{d}A\ \exp(-i\, \mathbf{q} \cdot \mathbf{r}_A). \tag{2.78}$$

Here r_z is the component of r along the z-axis, r_A is the component lying in the circular cross section. $\Delta\rho$ is the difference of electron density inside the pore wall and inside the pore, respectively. The integration along the z-axis yields the so-called axial factor of $L\frac{\sin(q_z L\gamma/2)}{q_z L\gamma/2}$ with L being the overall length of the pore, γ is the cosine of the angle between q and the z-axis. The integral in the x-y-plane leads to a Bessel function of first order $2\ A\ \frac{J_1(qR_0)}{qR_0}$, R_0 being the pore diameter. The result for the total scattered amplitude is:

$$F(q) \quad = \quad 2\ V\ \Delta\rho\ \frac{\sin(q_z L\gamma/2)}{q_z L\gamma/2}\frac{J_1(q_r R_0)}{q_r R_0}. \tag{2.79}$$

This result only applies to single pores. For dilute systems of single pores this equation still describes the scattered intensity, since in this case interference of the scattered waves emitted by neighboring pores can be neglected. This is not the case for dense packed systems, in this case the correlation between pores has also to be taken into account.

2.7.2 Simulation of SAXS-patterns

Inserting typical values of our mesoporous silicon ($R_0 = 5nm, L = 1\mu m$) and of the SAXS-experiment at beamline A2 (distance sample-detector = 3 m, size of the image = 8.25 cm × 8.25 cm on the detector, corresponding to $q_{max} = 0.08\text{Å}^{-1}$, $\lambda = 1.5$ Å, size of the beamstop: 9 mm width, 6 mm height) and assuming a Gaussian distribution of the pore orientation ($\sigma = 2°$) leads to the following simulated SAXS-images:

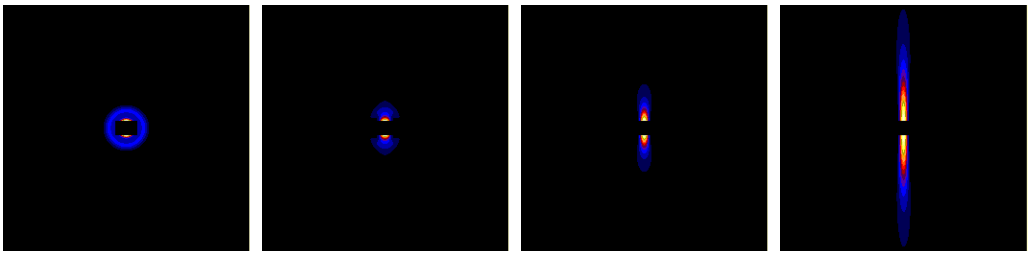

(a) $\phi = 90°$ (b) $\phi = 88°$ (c) $\phi = 85°$ (d) $\phi = 75°$

Figure 2.5: Simulated SAXS-patterns of pores with 2° width of their angular distribution

If the pores are oriented directly along the beam, small angle scattering occurs symmetrically. Upon tilting the pore axis around the vertical axis scattering is contained in a narrow, dipole shaped area.

This simulation assumes a diluted distribution of pores. But since all samples are of high porosity there exists some kind of short-range order and correlation, which should effect the SAXS-patterns due to strong interferences of the signals of neighboring pores. Proper treatment of interference and correlation in SAXS is possible in principle, but in our case not applicable to determine e.g. the pore radius distribution: We can only roughly estimate the mean pore-pore distance of our samples (from porosity and pore radius data given by the producer V. Timoshenko) and the width of its distribution, we lack knowledge of the exact coordination or geometry of the pores. Even a successful attempt to simulate the observed SAXS-patterns would not enable us to deduce e.g. an *independent* pore radius, since always several assumptions enter the simulations (for values like the mean pore length, mean pore radius, pore radius distribution, pore orientation, degree and kind of pore-pore-correlation, . . .). Due to the huge number of degrees of freedom entering such a simulation, and due to the strong intercorrelation of the entering variables, a determination of a single parameter like the pore radius without exact knowledge of the other parameters is not possible with sufficient precision.

Part II

EXPERIMENTS

3. SAMPLE

3.1 The Model Glass Former DBP:ferrocene

The glass investigated in this work is the model glass former dibutylphthalate:-ferrocene consisting of 95% dibutylphthalate and 5% ferrocene. This binary mixture dibutylphthalate:ferrocene (short: DBP:ferrocene) is well investigated in bulk [RZF76] [MFW+97] [Chu02] and in confinement [ASF+01], [Ser04]. This is an advantage, since we want to gain *principal* insights into the glass transition by observing the changes induced by geometrical confinement.

Pure **dibutylphthalate** (short: DBP) is a colorless viscous liquid of the chemical composition $C_6H_4[COO(CH_2)_3CH_3]_2$ (see Fig. 3.1(a)). Industry uses it as a plasticiser, and thereby it is also a good organic solvent. DBP is of particular interest for us because it is a very well known glass former of medium fragility (m = 69) with T_G of 179 K at a cooling rate of 10 K/s. The relative low temperature of the glass transition with respect to its Debye temperature is an advantage when applying Mößbauer-techniques due to the strong temperature-dependent decrease of f_{LM}.

Ferrocene ($Fe(C_5H_5)_2$) is a metallocene with sandwich-like molecular structure (see Fig. 3.1(b)) and particular well-investigated due to its broad application in chemical industry. At room temperature it forms orange crystals.

Ferrocene crystals can easily be solved in DBP by adding them at room temperature and stirring. Solving 5% ferrocene in DBP does neither lead to crystallization upon cooling nor change the value of T_G [MFW+97]. The

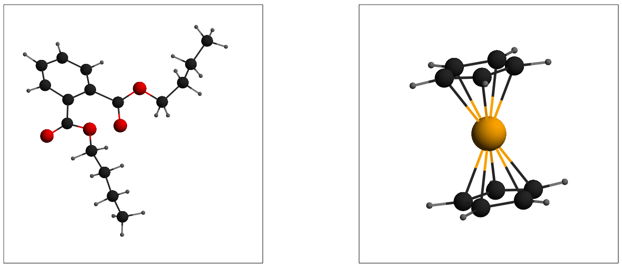

(a) Dibutylphthalate (b) Ferrocene

Figure 3.1: Chemical structure of dibutylphthalate and ferrocene

values of the critical glass transition temperature of bulk DBP:ferrocene is $\approx 200 - 205$ K [SFA+02].

3.2 The Confining Matrix: Porous Silicon

Porous silicon (pSi) is a material usually made from crystalline silicon by electrochemical etching with hydrofluoric acid HF [Leh02]. The term subsumes a lot of morphologically different materials, the morphologies of which depend e.g. on doping type and density, applied bias and current, HF concentration and its type of solvent (e.g. water or ethanol). Following the definition of Lehmann, we distinguish between *macroporous silicon* with pore diameters $d > 50$ nm and long, very straight oriented pores, *microporous silicon* with pore diameters $d < 2$ nm and sponge-like, unoriented morphology, and *mesoporous silicon* with intermediate pore diameters (2 nm $< d <$ 50 nm) and a morphology transiting from oriented to unoriented channels.

Mesoporous silicon thereby covers the pore diameters examined by previous NFS-experiments of DBP:ferrocene in confinement, while the orientation of its pores makes it feasible to study the geometrical influence of confinement.

3.2.1 Application as a confining matrix

In contrast to already applied experiments concerning glass dynamics in 2d-confinement [Ser04], [ASF+01] the application of pSi as a confining matrix allows to measure the *orientation dependence* of relaxational behavior. This was achieved by measuring QNFS-spectra with the direction of the incoming synchrotron radiation both parallel and perpendicular with respect to the pSi channel-axis (I will refer to this often simply by either the parallel or the perpendicular case). This makes it possible to compare the spectra, and thereby get information about the influence of confinement on dynamics.

3.2.2 Production

Porous silicon is made from single crystalline silicon wafers by electro-etching in hydrofluoric acid. The initial state of the silicon surface is hydrogen-terminated. Without applying a bias no reaction takes place, an anodic bias is needed to stimulate pore formation:

In a first reaction step an electron hole allows HF_2^- to substitute one of the terminating hydrogen-atoms by fluor, resulting in gaseous hydrogen. Since the availability of the hole is crucial for low voltages this step is rate-limiting, the next reaction steps follow immediately.

The Si-F bond polarizes the remaining three Si-bonds, which enables substitution of the second hydrogen under electron emission. Both fluor-atoms polarize the Si-Si-backbonds sufficiently so that further reaction with HF or H_2O can remove the Si-atom from the surface. As a result the remaining surface is again hydrogen-terminated. This applies to (100) and (110) surfaces, since they consist of Si with two hydrogen-bonds each. (111)-surfaces only offer one Si-H-bond versus three Si-Si bonds. Thereby polarization of the back-bonds is insufficient, and etching takes place predominantly only on steps of (111)-surfaces.

By this reaction mechanism pores originate at the surfaces and form a layer of pore tips. An extended space charge region (SCR) througout the layer and into the bulk material is formed. In strongly doped silicon (p^+-type) and under anodic bias tunneling of holes through the SCR occurs, forming mesoporous silicon. Due to the strong electric fields at the pore tip and the small pore-pore-distances usually obtained in highly p-doped silicon, holes are exclusively consumed here and can not enter the pore walls. The already formed layer of porous silicon is consequently depleted of charge carriers, and no electrochemical reaction takes place here. This leads to formation of straight channels and transforms bulk silicon into a passivated film of mesoporous silicon. Since the etching process is strongly anisotropic the direction of the channels is determined by the crystallographic orientation of the wafer. Especially wafers with (100)-surface show **pores growing perpendicular to the wafer surface**.

The pSi films provided by Victor Timoshenko from the TU München were small discs of ≈ 32 mm diameter made from (100)-oriented silicon wafer. The outer rim (1-2 mm) was very brittle, because it was in contact with the seal of the anodization chamber. The upper side was black and reflecting like pure silicon (see Fig. 3.2(a)), the lower side was often colored (see Fig. 3.2(b)). Very often these discs broke or developed cracks at the end of the manufacturing process, when the porous film was lifted from the substrate. The individual samples were numbered chronologically, their most important properties are displayed in Tab. 3.1.

disc	**resistivity, Si doping [mΩ cm]**	**current density [mA/cm^2]**	**film thickness [μm]**	**pore diameter [nm]**	**porosity**
#2	15, p^+	50	70	$\approx$ 5-8 nm	
#4	10-30, p^+	25	90	$\approx$ 3 nm	40%
#5	1-2, p^{++}	30	100	> 10nm	71%

Table 3.1: Parameters of the samples provided by TU München

Due to the small thickness and the high porosity of the films the inner part still was quite brittle. Great care was needed during all stages prior to the experiment to avoid further breaking of the discs or stripes.

3.2.3 Preparation

To make measurements in both orientations of the pore axis as comparable as possible the geometrical thickness in both directions should be approximately the same. Additionally a reasonable total resonant thickness of the sample is required for the experiment to be feasible. A single stripe of pSi with a thickness of $\approx$ 70 - 100 μm would not be enough to conduct experiments in reasonable time.

Calculation of the mean free path due to electronic absorption and scattering in porous silicon (porosity 50%-60%) filled with DBP:ferrocene resulted in optimal sample thickness in the order of 1 mm and a normalized resonant thickness of $\xi/f_{LM} \approx 2.5 - 3.6$. This is enough to do NFS-experiments in reasonable time.

Since at least a dozen stripes of good quality are needed to form a single sample the discs had to be cut routinely and reproducibly. Additionally the cutting had to be very gentle, so as not to rupture the discs in the process. Therefore the discs were cut with a diamond wiresaw: The sample was pushed against a moving wire impregnated with small diamonds, and slowly cut by the resulting friction. To minimize vibrations and to protect and support the stripes during the cutting process the porous silicon discs were clamped between disc holders made of plexiglass. The diamond wire accessed the discs through small slits in the disc holder. To carry away small pieces of porous silicon produced during the cutting process the wire was wetted with deionized water.

3.2.4 Characterization with SAXS

All data shown here was taken at the SAXS-beamline A2 at DORIS. The wavelength was $\lambda = 1.50$ Å, corresponding to an energy of 8.25 keV. The experimental setup is straightforward and can be seen in Fig. 3.3.

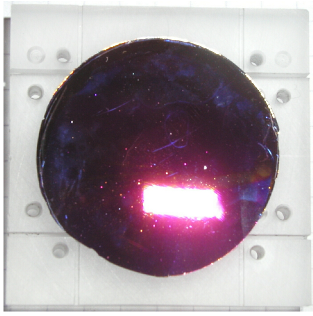

(a) Upper side of disc #2 on the first disc holder used for cutting.

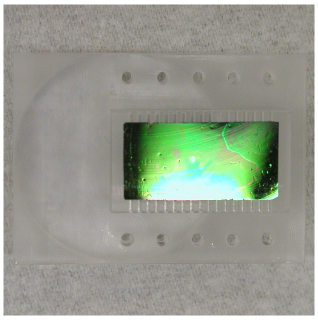

(b) One half of the inner square of disc #2 on the second disc holder, visible is the lower side.

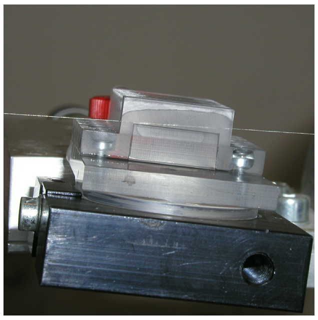

(c) The last step of the cutting process . . .

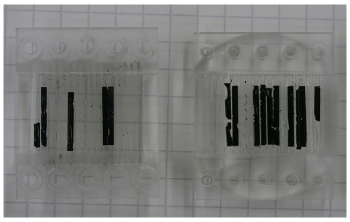

(d) The results of a rather successful final cutting step immediately after cutting.

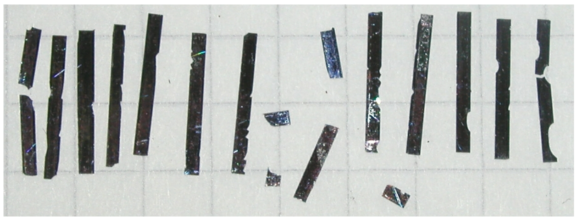

(e) . . . and after drying.

Figure 3.2: Cutting of the mesoporous silicon films.

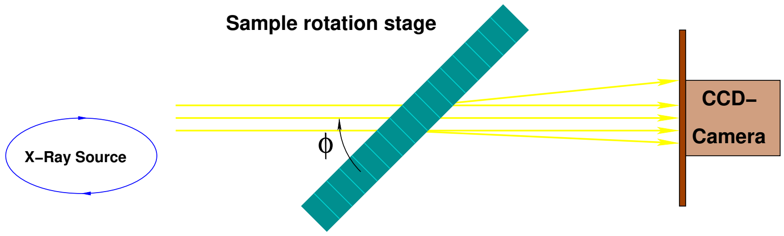

Figure 3.3: Typical SAXS-experiment

The samples were mounted vertically on a ϕ-circle, thereby the pore axis was always horizontal (neglecting a sub-degree amount of vertical tilt). The scattering patterns were recorded with a CCD-camera in a distance of 3 m and in steps of 1 degree (#2) and 1/4 degree (#4 #5) in ϕ; there is a pronounced change in the SAXS-pattern upon rotating the samples:

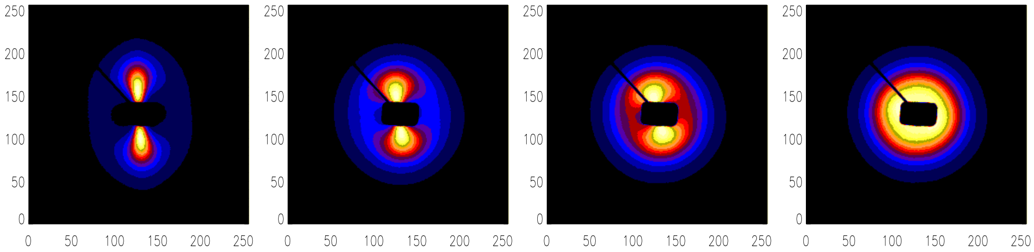

(a) $\phi = 60°$ (b) $\phi = 80°$ (c) $\phi = 85°$ (d) $\phi = 90°$

Figure 3.4: SAXS-patterns from sample #2

$\phi = 0°$ is defined as the angle between beam and sample surface. For small angles ϕ (see Fig. 3.4(a)) the scattering from the pores results in sharp dipole-shaped patterns. Upon approaching an incident angle of 90° (pore axis parallel to the beam) the scattered intensity is distributed symmetrically.

Between the three samples an obvious difference is the angular range, in which the transition between dipole-shaped pattern and symmetric pattern occurs.

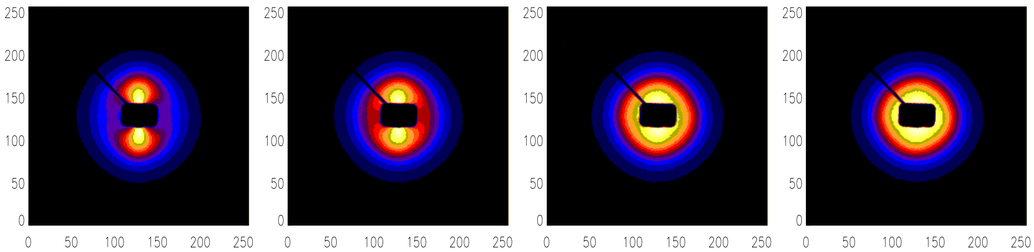

(a) $\phi = 75°$ (b) $\phi = 80°$ (c) $\phi = 85°$ (d) $\phi = 90°$

Figure 3.5: SAXS-patterns from sample #4

From this data it was possible to estimate an upper limit for the width of the angular distribution of the pores:

As we saw in the simulation of the dilute pore-system we may assume that a tilted pore only scatters parallel to its tilt axis. Thereby the axis of the dipole corresponds to the tilt axis.

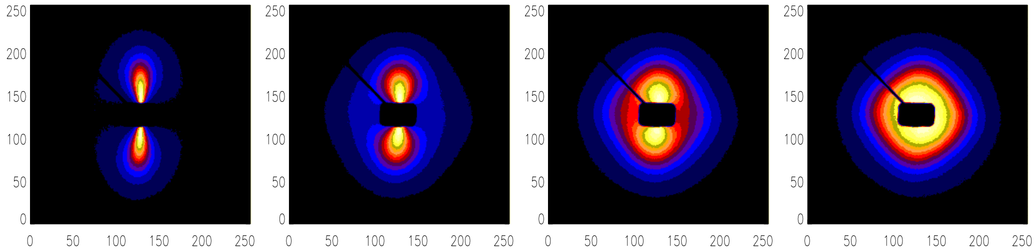

(a) $\phi = 85°$ (b) $\phi = 87.5°$ (c) $\phi = 88.75°$ (d) $\phi = 90°$

Figure 3.6: SAXS-patterns from sample #5

Since any liquid-like correlation of pores would only affect the radial but not the angular distribution of the scattered intensity, this result may be expanded to the case of dense distributions of pores. The contrast between intensity scattered parallel and perpendicularly to the dipole axis completely diminishes in the symmetric position ($\phi \approx 90°$).

The decay of the perpendicularly scattered intensity is directly connected with the angular distribution of the pore axes: If the sample is tilted more than the width of the angular distribution of the pore axes, almost no pores are in the symmetric position, and thereby no intensity is scattered perpendicularly to the tilt axis. (See Fig. 2.5.) The evaluation of the SAXS-measurements was done in several steps:

1. The dipole-axis was determined by localization of the maxima of scattered intensity

2. The intensity scattered perpendicularly to this axis was extracted

3. A Lorentzian curve was fitted to the intensity over angle plot, as can be seen in Fig. 3.7

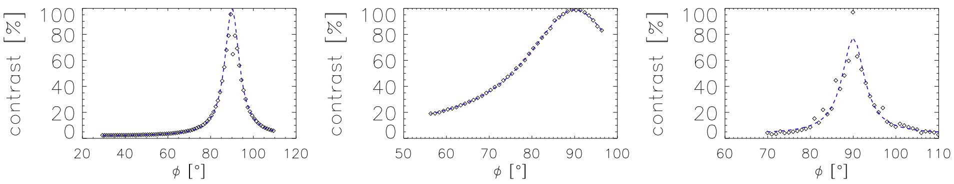

Figure 3.7: Fraction of the perpendicularly scattered intensity compared to the parallel scattered intensity (◊) for #2, sample #4 and sample #5 (from left to right), fitted with a Lorentzian (dashed line).

All three slopes are well described by a Lorentzian, the corresponding FWHM were extracted and can be seen in Tab. 3.2:

	#2	**#4**	**#5**
Nominal pore diameter	5-8nm	3nm	$>$ 10 nm
FWHM	9.5°	28.2°	6.3°

Table 3.2: Width of the angular distribution of the Lorentzian derived from fits shown in Fig. 3.7

These values are *upper limits* of the width of the angular distribution of the pore axis, since we neglected perpendicularly scattering of the tilted pores. This is justified as can be seen from the simulation of a distribution of pores (see Fig. 2.5).

The functional dependence of the width of the angular pore-axis distribution with pore diameter shows an increase of disorientation for smaller pores. This can be attributed to the beginning transition into the microporous silicon regime, where no pore-axis orientation is dominant any more.

3.2.5 Filling DBP:ferrocene into the pores

Dibutylphthalate 99+% was used as delivered by Sigma-Aldrich (Cat.: 24,047-8). DBP:ferrocene used for SAXS and filling experiments was prepared from non-enriched ferrocene, DBP:ferrocene for nuclear-resonant experiments (Mößbauer spectroscopy and NFS) was made using ^{57}Fe-enriched ferrocene (enrichment grade $\eta = 0.95$) provided by T. Asthalter (University of Stuttgart) from the same batch that was already investigated in [Chu02], [ASF$^+$01], [Ser04]. DBP:ferrocene was prepared by adding the proper amounts of 5 mol-% ferrocene to 95 mol-% DBP in an airtight container and stirred for several days.

Before filling the stripes of porous silicon to be prepared for experiment they were put into a vacuum chamber and evacuated for at least one week at pressures below $1 \cdot 10^{-5}$ mbar to empty the pores. The chamber was flushed with high-purity nitrogen (purity 5.6) and the stripes were immediately put into freshly prepared DBP:ferrocene, and left there to soak up the DBP:ferrocene for several days.

Several sample holders were designed to contain samples consisting of several stripes of 1mm width stacked up to 1 mm height. The sample can either be examined through a channel in the holder surface or a opening in the bottom, thereby allowing parallel and perpendicular measurements to be done with the same sample. Additionally the holders allowed for easy and fast rotation of the sample between parallel and perpendicular position (see Fig. 4.2).

4. QUASI-ELASTIC NUCLEAR FORWARD SCATTERING EXPERIMENTS

In this chapter the actual implementation of the experiments will be discussed. The experimental setup and its technical realization will be shown in the first section. The resulting data will be presented along with an ad-hoc fit. Results which could be directly deduced from the data are shown in the last part.

4.1 Setup

All QNFS experiments presented in this work were carried out at the nuclear resonance beamline ID18 at the ESRF in Grenoble. The experimental setup can be seen in Fig. 4.1:

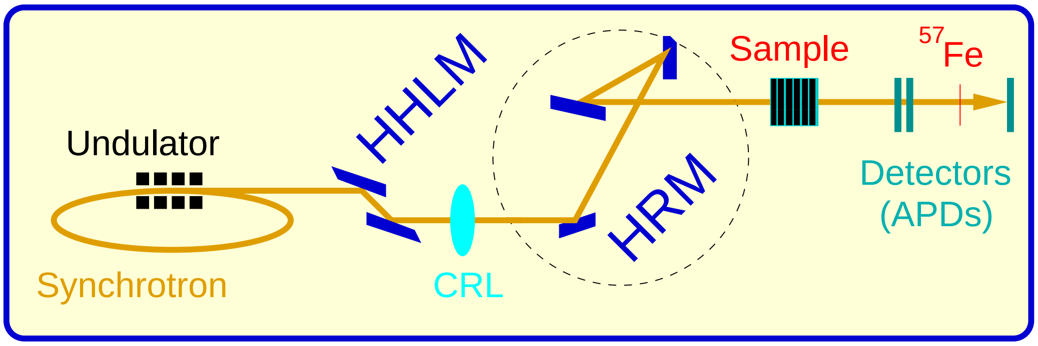

Figure 4.1: Setup of QNFS-experiments at ID18, ESRF, for detailed explanation see text. CRL: compound refractive lens, HHLM: high heat load monochromator, HRM: high resolution monochromator, APD: avalanche photo diode.

The ESRF ***storage ring*** has a circumference of 844.4 m, so a 6 GeV electron travelling at speed of light takes 2.815 μs for one revolution. In the so-called *16-bunch mode* 16 equidistant buckets are filled with a total of 90 mA, resulting in a free time window of 176 ns between two bunches. This is comparable to the life time of ^{57}Fe. In *4-bunch mode* the total current is reduced, but the larger time window of 704 ns enables data collection for up to five nuclear life times.

At beamline ID18 three 1.6 m long ***undulators*** produce synchrotron radiation optimized for highest flux at energies between 6 and 30 keV. In a first step the beam is monochromatized with a ***liquid-nitrogen cooled silicon (1 1 1)-reflection high heat load monochromator*** (short HHLM) which transmits a 3 eV band. At 14.4 keV in a 2mm $\times$ 1mm slit the total flux exceeds $6 * 10^{13}$ photons per second and per 3eV bandwidth.

Since the ^{57}Fe-nuclei only accept radiation in an energy range of a few neV, almost the complete 3 eV band would pass through the sample without any nuclear interaction. Further monochromatization is a must to decrease the overall background and not to overload the detector system. This is achieved by the ***high resolution monochromator*** (HRM) which consists of three crystals - in our case a symmetric-cut germanium crystal using the (3 3 1)-reflection and two strongly asymmetric cut silicon crystals using the (9 7 5)-reflection - reducing the transmitted energy band down to 0.65 meV. To improve the performance of the HRM a ***compound refractive lens*** (CRL) is placed in the beam before the HRM in order to reduce the divergence of the incident beam to match the acceptance of the (9 7 5)-reflections. In this setup a typical flux of more than 10^8 photons per second in the 0.65 meV bandwidth is achieved.

This highly monochromatized beam impinges on the ***sample***, which was positioned in a Oxford Instruments Optistat helium flow cryostat to attain temperatures in the range from 25 - 300 K. A Oxford ITC503 temperature controller adjusted the power of a heater incorporated into the cryostat. Two temperature sensors were applied: The first one was inside the cryostat and a Cernox temperature sensor was directly mounted against the side of the sample holder furthest away from the cryofinger. Temperature control was achieved using the built-in sensor, the Cernox sensor as can be seen in Fig. 4.2 was used to monitor the actual sample temperature.

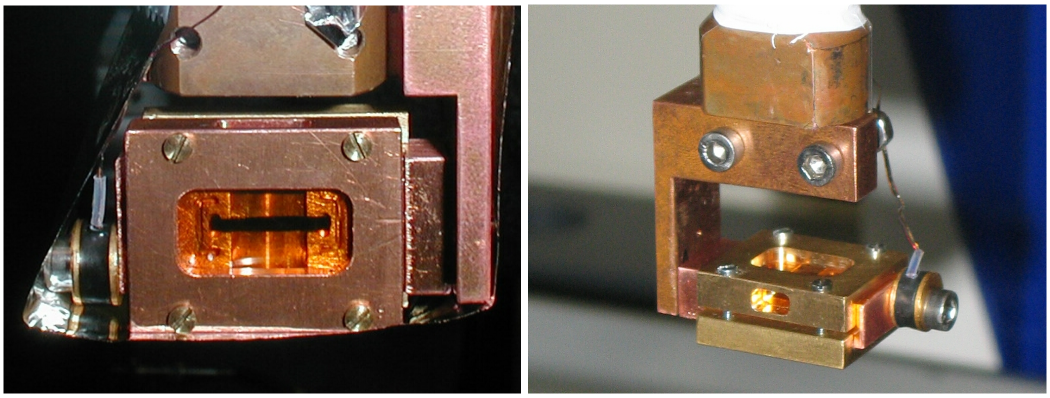

Figure 4.2: Left: The 7 mm-aperture sample-holder containing sample #2 during mounting, in the position referred to at as the *parallel case*. At the left side of the sample holder the Cernox sensor is visible. Insulation against heat transfer by radiation was done by wrapping aluminized mylar around the sample. **Right:** The 3.5 mm-aperture sample-holder in the *perpendicular case* position. Thermal contact with the cryostat was achieved by the copper elbow.

The non-resonant 99.98% of the radiation were transmitted through the sample and interacted solely with the electronic shell. After a few picoseconds all excitations and their respective cascades decayed. Only photons in the resonant bandwidth of the order of 100 neV interacted with the nuclei, causing a QNFS-signal which was detected in the semi-transparent ***avalanche photo diodes*** (APDs) downstream (see Fig. 4.3).

Approximately one-fourth of the beam was transmitted through two semi-transparent APDs. An iron foil enriched in ^{57}Fe was put into the remaining beam to monitor the incident resonant flux. The very intense NFS-signal from the iron-foil was detected by a third APD.

The APD-pulses and the bunch clock signal of the ring are fed into a constant-fraction-discriminator and a time-to-amplitude converter. The extremly strong pulses around $\Delta t = 0$ which do coincide with the bunch clock

Figure 4.3: Sample environment and APD setup: In the background the sample holder is visible already mounted in the cryostat. Behind the cryostat the entrance slit from the optics hutch can be seen. The two APDs in the center are detecting the QNFS-signal from the sample. The APD in the foreground monitored the incident resonant flux.

are rejected by a veto, thereby only so-called *delayed* APD-pulses are processed. Both the bunch clock signal and the delayed signals are then fed into the start/stop-channels of time-to-amplitude-converters, which generate pulses whose height corresponds to the delay time Δt. These are then digitized by AD-converters and accumulated in multi-channel analyzers (MCA). The MCAs are read out from the beamline control computer.

4.1.1 Sample description

Tab. 4.1 gives an overview of the most important sample parameters which were varied in the experiments:

sample	parallel case sample size W×H×D [mm]	perpend. case sample size W×H×D [mm]	bunch mode	temperature [K]
#2	$7 \times 0.77 \times 1.05$	$7 \times 0.8 \times 0.77$	16	20 - 218
#4	$3.5 \times 0.81 \times 1.05$	$3.5 \times 0.8 \times 0.81$	4 & 16	153 - 218
#5	$3.5 \times 0.80 \times 1.05$	$3.5 \times 0.8 \times 0.80$	4	152 - 237

Table 4.1: Parameters of samples used at the ESRF. Effective geometric sample size as defined by the slits of the sample holder and sample thickness is given in horizontal width (**W**) × vertical height (**H**) × sample thickness (**D**). Temperature ranges reflect the actual sample temperature covered by the experiments.

The height of the apertures in the applied sample holders were 0.8 mm in the parallel case and 1 mm in the perpendicular case, but since it was not possible to fill the sample holder with more than $\approx$ 0.8 mm of porous silicon stripes due to a slight curvature of the stripes, the effective cross section was the same for the parallel and the perpendicular case, but the effective thickness of the sample was reduced in the parallel case.

For all samples time spectra were measured at at least 10 different temperatures starting from 150 K, starting at the lowest temperature, usually in 5 - 10 k steps, until the integral count rate was too low to measure time spectra with reasonable precision. Reproducibility of the time spectra was checked by returning to lower temperatures for each sample.

4.2 Results

The obtained time spectra will be presented for each sample and both orientations at three to four temperatures: (1) well below the *bulk* glass transition temperature T_g of $\approx$ 178 K, (2) between T_g and the *bulk* mode coupling critical temperature T_C of $\approx 205K$, (3) approaching T_C and (4) well above T_C.

It is possible to fit the time spectra with a purely static theory function to a good degree of accuracy. For each sample the corresponding final fits are included into the time spectra.

Results already evident from this fit are presented below.

4.2.1 Data analysis

The data sets were fitted by a model function consisting of a coherent superposition of two quadrupole doublets and an incoherently added broad line described by the following parameters:

- Incident resonant flux $\mathbf{I_0}$,
- Resonant effective sample thickness ξ,
- Principal quadrupole splitting $\mathbf{\Omega}$,
- Second quadrupole splitting $\mathbf{\Omega_2}$,
- Relative isomer shift between both quadrupole doublets $\mathbf{\Delta}\delta$,
- Relative fraction of $\frac{\text{Second QS}}{\text{Principal QS + Second QS}}$ is denominated κ,
- Amplitude $A_{\mathbf{fast}}$ and relaxation time $\tau_{\mathbf{fast}}$ of fast decaying exponential line,
- Diffusional relaxation time $\tau_{\mathbf{diff}}$.

The superposition of the two quadrupole splittings was calculated coherently. This was realized by an adaption of Eq. 2.25 for two different quadrupole frequencies:

$$\chi_{00}^{(n)}(\mathbf{k},\omega) \propto i\,\varphi(\mathbf{k},\omega)\,\left((1-\kappa)\cos\left(\frac{\Omega}{2}t\right) + \kappa\cos\left(\frac{\Omega}{2}t\right)\exp(i\Delta\delta t)\right). \quad (4.1)$$

The evaluation of the consecutive Fourier transformations (Eq. 2.26 and Eq. 2.18) was then done with a fast-Fourier-transform based algorithm. Since no interconnection between the two quadrupole frequencies was assumed this model will be referred to as the ***static model***.

The third component, the fast decaying exponential line close to $t = 0$ was added incoherently, since such a fast decay is usually connected to fast molecular dynamics. Since a fast dynamics leads to quick successive phase shifts it destroys the coherence thereby leading to short nuclear life times and large line widths. The fitting procedure was applied as follows:

1. *First fit:* The data set with **lowest temperature** T_0 (25 K for sample #2, 150 K for sample #4 and #5) was fitted with a single quadrupole splitting Ω. We may neglect relaxation in a first step since the confined liquid is still frozen well below T_g. This fit, together with the monitor-data, yields the incident resonant flux $I_0(T_0)$.

2. *Normalization:* This $I_0(T_0)$ was used to normalize the monitor signal obtained from the third APD, and enabled the calculation I_0 for the remaining temperatures: $I_0(T) = I_0(T_0)\frac{Monitor(T)}{Monitor(T_0)}$.

3. *First fit (continued):* The data sets for higher temperatures were fitted accordingly with the corresponding I_0 **kept fixed** at the values calculated during *Normalization*. Thereby the fit determined a unique value of the resonant effective sample thickness $\xi(T)$.

4. *Second fit:* The second quadrupole splitting Ω_2, its relative isomer shift $\Delta\delta$ and fraction κ was added.

5. *Third fit for short times:* The fast exponential line was added (A_{fast}, τ_{fast}). τ_{fast} was then determined to be $\approx 0.02\tau_0$, and was fixed to this value consequently to reduce the number of degrees of freedom of the fit.

6. *Final fit:* The relaxation time τ_{diff} was set free.

4.2.2 Static model fits

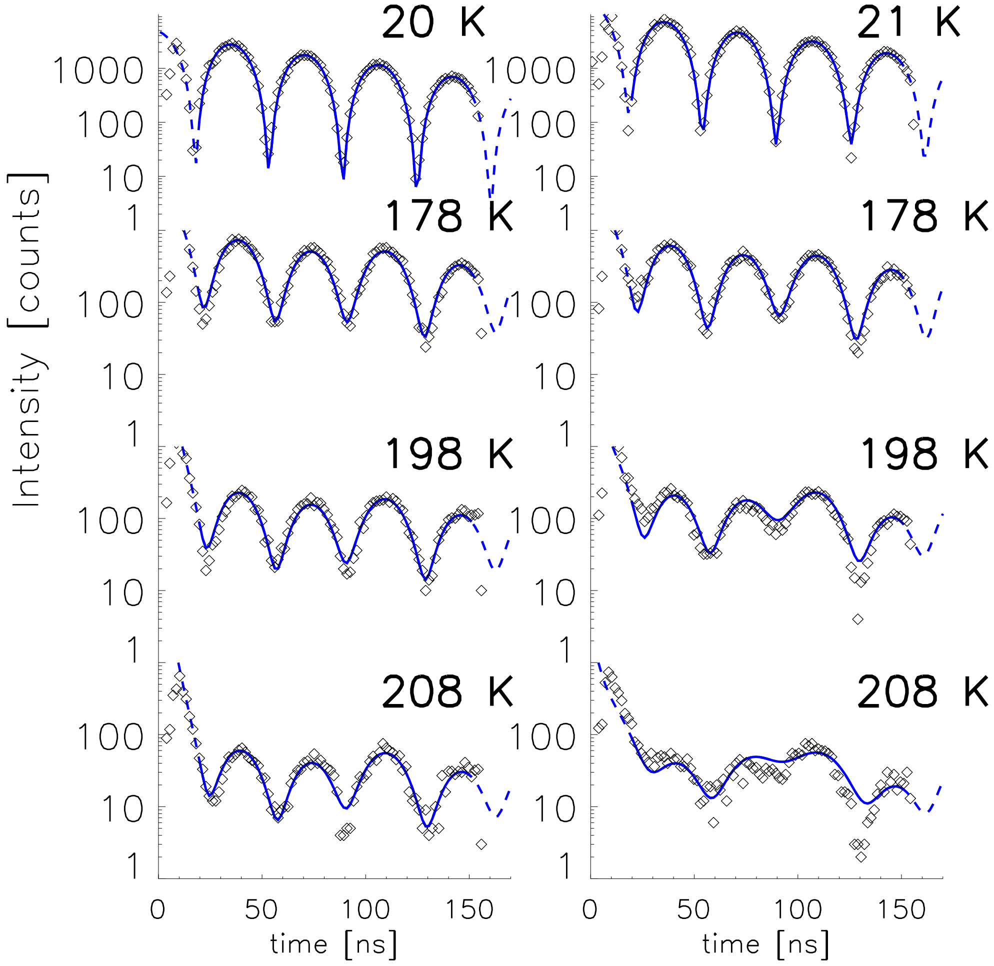

Figure 4.4: NFS-Signal of sample #2: ◇, **Left:** Parallel sample orientation, **right:** Perpendicular sample orientation. **Solid line:** Fit to the data.

Shown in Fig. 4.4 are data sets of sample #2 for selected temperatures with corresponding fits. For low temperatures the NFS-signal is independent of the sample orientation, showing only the quantum beating due to the quadrupole splitting of solid bulk DBP:ferrocene. At 208 K, well above the T_C of bulk DBP:ferrocene strong differences in both orientations are visible. The onset of these differences can already be observed starting from 178 K, which corresponds to the glass transition temperature T_g of bulk DBP:ferrocene.

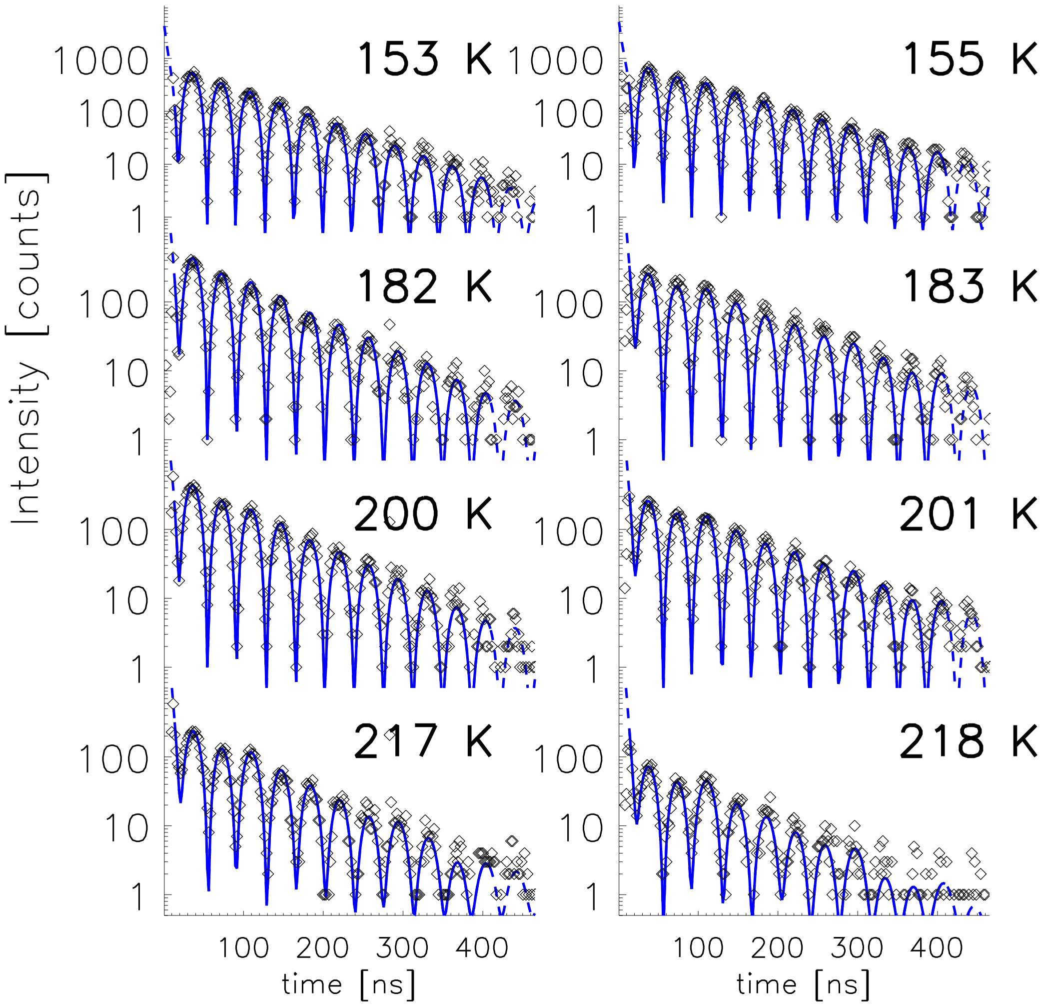

Figure 4.5: NFS-Signal of sample #4: ⋄, **Left:** Parallel sample orientation, **right:** Perpendicular sample orientation. **Solid line:** Fit to the data.

Fig. 4.5 shows the NFS-signals recorded with sample #4. Again, at low temperatures the signals only show the quantum beating of bulk DBP:ferrocene, without any differences depending on orientation. Differences develop gradually for higher temperatures[1].

[1] The peak in the parallel data sets at ≈ 282 ns is due to an electronic reflection of the prompt peak. Later on it was removed by a damping resistivity in the electronics. In the data sets where it occured it was excluded from the fit.

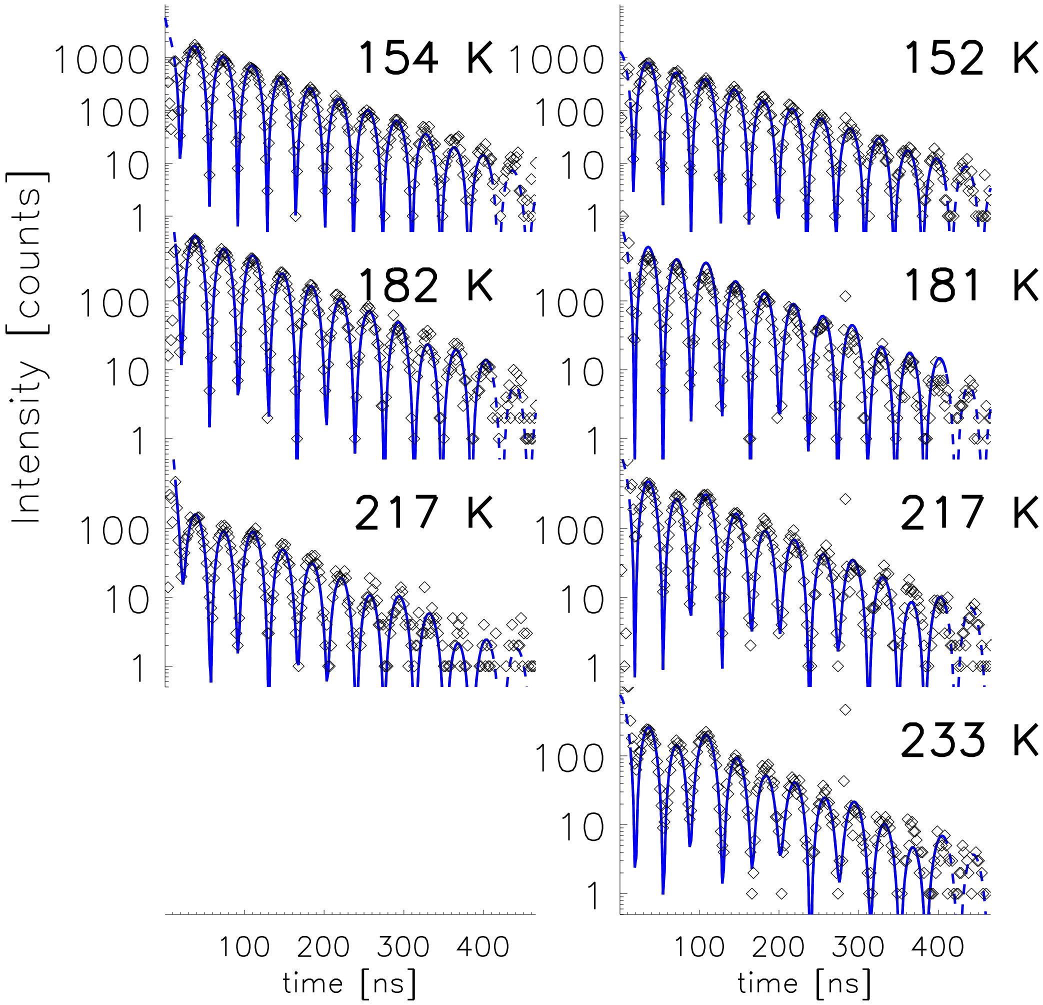

Figure 4.6: NFS-Signal of sample #5: $\diamond$, **Left:** Parallel sample orientation, **right:** Perpendicular sample orientation. **Solid line:** Fit to the data. Measurements were possible up to 217 K in the parallel orientation and 238 K in the perpendicular orientation.

As before, the signals far below T_g are independent on the sample orientation. At higher temperatures the spectra show differences which are modelled by the fit to a high degree of accuracy. The accessible temperature range is increased up to 240 K in the perpendicular orientation. It was only possible to measure a NFS-signal in reasonable time up to 220 K with parallel sample orientation. [2]

4.2.3 Principal quadrupole splitting: Motional narrowing

Fig. 4.7 shows the temperature dependence of the principal quadrupole splitting Ω [3]. For low temperatures the values ($24.8 \pm 0.1\,\Gamma$ in the parallel case and $24.7 \pm 0.1\,\Gamma$ in the perpendicular case) are comparable to findings in bulk DBP:ferrocene [MFW+97] and confined DBP:ferrocene [ASF+01] of $24.7\,\Gamma$. For higher temperatures motional narrowing is observed down to $24.1 \pm 0.1\,\Gamma$ in the parallel case and down to $22.4 \pm 0.2\,\Gamma$ in the perpendicular case.

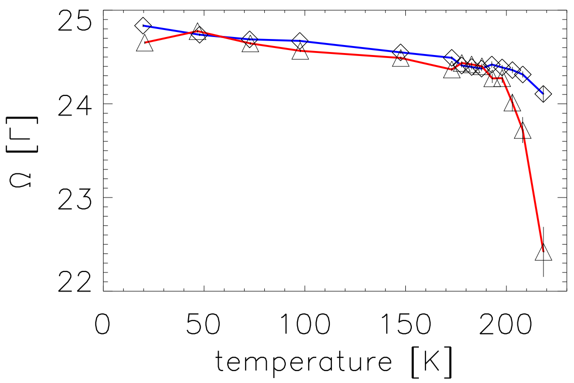

Figure 4.7: The values for the principal quadrupole splitting Ω of sample #2, $\diamond$, blue line: Parallel sample orientation, $\triangle$, red line: Perpendicular sample orientation.

As can be seen in Fig. 4.8 and Fig. 4.9 at low temperatures the values for Ω in sample #4 ($24.4 \pm 0.1\Gamma$) and #5 ($24.4 \pm 0.1\,\Gamma$) are consistent with the data from sample #2. During heating we observed motional narrowing

[2] The peak due to reflection of the prompt pulse is again visible in some of the perpendicular data sets of sample #5 as already seen before in sample #4. It was excluded from the fits.

[3] All hyperfine parameters like quadrupole splitting and Isomer shift (IS) are given in units of the natural linewidth $\Gamma = 4.6$ neV of ^{57}Fe.

down to $\Omega = 24.0 \pm 0.1\,\Gamma$ at 220 K / $\Omega = 24.0 \pm 0.4\,\Gamma$ at 220 K in the parallel / perpendicular case for sample #4 and down to $\Omega = 24.2 \pm 0.1\,\Gamma$ at 220 K / $\Omega = 24.0\,\Gamma \pm 0.1$ at 240 K for sample #5.

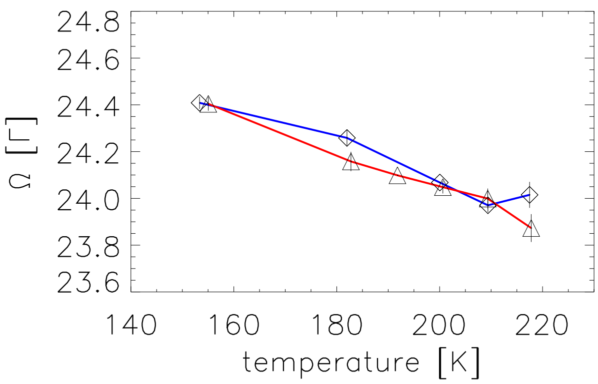

Figure 4.8: The values for the principal quadrupole splitting Ω of sample #4, $\diamond$, **blue line:** Parallel sample orientation, $\triangle$, **red line:** Perpendicular sample orientation.

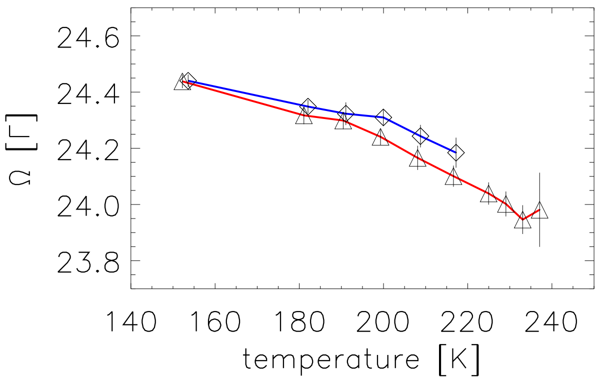

Figure 4.9: The values for the principal quadrupole splitting Ω of sample #5, $\diamond$, **blue line:** Parallel sample orientation, $\triangle$, **red line:** Perpendicular sample orientation.

4.2.4 Second quadrupole splitting: Relative fraction

Fig. 4.10 (left) displays the relative fraction κ of the second quadrupole splitting. Up to 148 K the forward spectra are dominated by the principal quadrupole splitting, thereby the relative fraction is ≈ 0. Above 148 K a strong increase is observed, with κ being $36 \pm 2\%$ at 218K in the parallel case and $62 \pm 4\%$ in the perpendicular case.

The fit parameter Ω_2 is only well defined above 148 K; its temperature dependence is displayed in Fig. 4.10 (right). Up to 208 K the values fluctuate around $9.8 \pm 0.1\,\Gamma$. At 218K there is a sudden drop down to $8.7 \pm 0.2\,\Gamma$ in the perpendicular case which may be attributed to motional narrowing as already observed in Fig. 4.7.

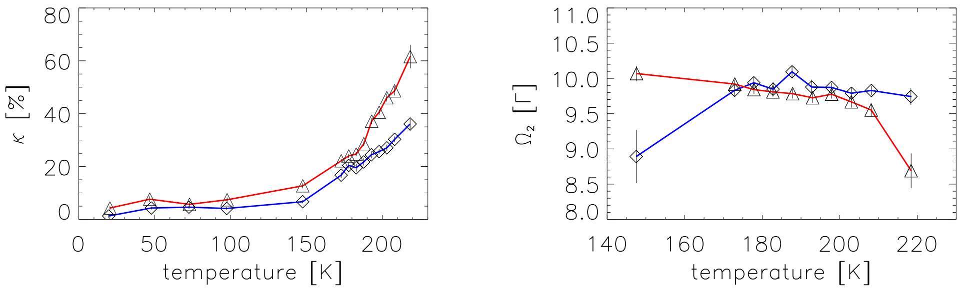

Figure 4.10: Left: The relative fraction κ of second quadrupole splitting Ω_2 of sample #2 in relation to both quadrupole splittings. **Right:** The values for the second quadrupole splitting Ω_2. $\diamond$, blue line: Parallel sample orientation, $\triangle$, red line: Perpendicular sample orientation.

For sample #4 Fig. 4.11 (left) shows the increase of κ from 1.4 ± 0.6 % / 3.5 ± 0.7 % to 13 ± 1 % / 18 ± 1 % in the parallel / perpendicular case. The value of the quadrupole splitting varies around $9 \pm 0.5\,\Gamma$ / $10 \pm 0.5\,\Gamma$.

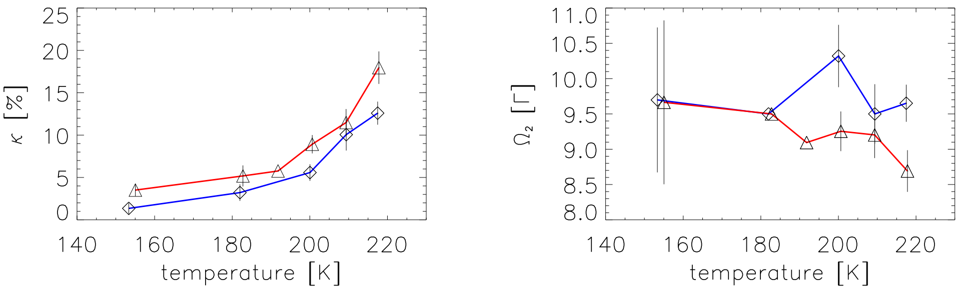

Figure 4.11: Left: The relative fraction κ of second quadrupole splitting Ω_2 of sample #4 in relation to both quadrupole splittings. **Right:** The values for the second quadrupole splitting Ω_2. $\diamondsuit$, blue line: Parallel sample orientation, $\triangle$, red line: Perpendicular sample orientation.

In Fig. 4.12 (right) we can see in the case of sample #5 that the value of the second quadrupole splitting is scattering around 9 Γ without any evidence for motional narrowing. Below Fig. 4.12 (left) shows κ, increasing steadily from 2-4% at 150 K up to 15% at 217 K for parallel case and more than 23% at 238 K in the perpendicular case.

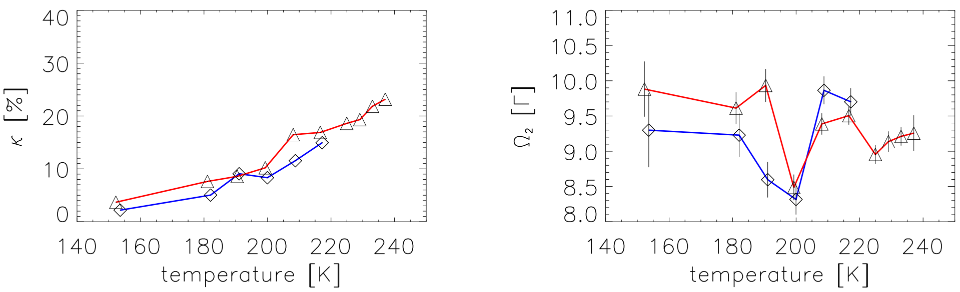

Figure 4.12: Left: The relative fraction κ of second quadrupole splitting Ω_2 of sample #5 in relation to both quadrupole splittings. **Right:** The values for the second quadrupole splitting Ω_2. $\diamondsuit$, blue line: Parallel sample orientation, $\triangle$, red line: Perpendicular sample orientation.

Due to the increase in κ the errors for the estimation of Ω_2 in Fig. 4.12 are decreasing with temperature. On the other hand the errors for the principal quadrupole splitting in Fig. 4.9 are rising with temperature due to its decreasing magnitude $\propto (1-\kappa)$.

4.2.5 Isomer shift of the second quadrupole splitting

The second quadrupole splitting exhibits a small but measurable isomer shift relative to the principal quadrupole splitting. Its influence on NFS-signals is small, and the existence of a non-zero isomer shift was only realized with the aid of the Mößbauer spectroscopy data.

The isomer shift for sample #2 (see Fig. 4.13) shows no pronounced temperature dependence in the vicinity of the glass transition, $\Delta\delta \approx 2.1 \pm 0.1\,\Gamma$ / $\Delta\delta \approx 2.2 \pm 0.1\,\Gamma$ in the parallel / perpendicular case.

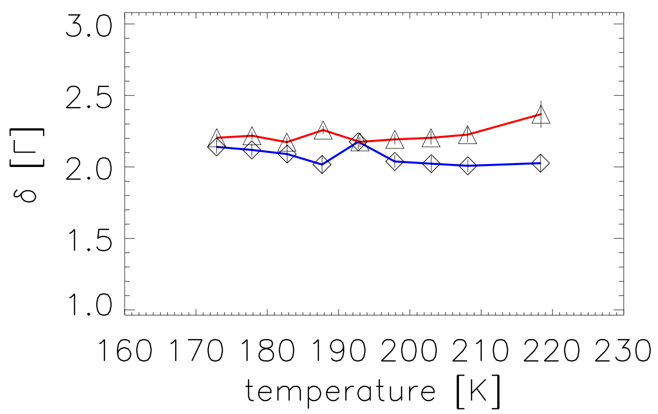

Figure 4.13: Isomer shift $\Delta\delta$ of the second quadrupole splitting of sample #2: $\diamondsuit$, blue line: Parallel sample orientation, $\triangle$, red line: Perpendicular sample orientation.

The existence of a positive isomer shift is reproduced qualitatively for sample #4 and #5, but its value is approximately halved: $1.0 \pm 0.1\,\Gamma$ /

$0.9 \pm 0.1\Gamma$ for sample #4 in the parallel / perpendicular case, $1.1 \pm 0.1\,\Gamma$ / $1.0 \pm 0.1\,\Gamma$ for sample #5.

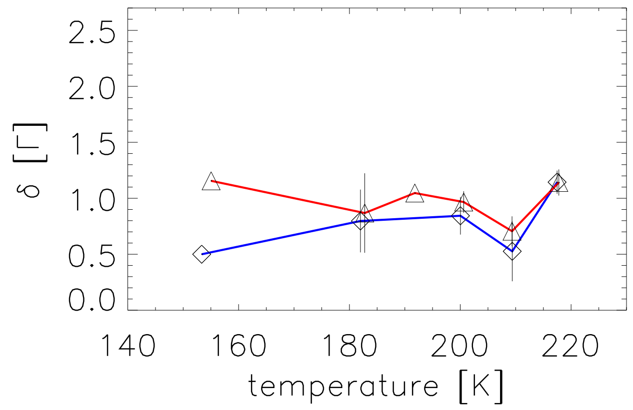

Figure 4.14: Isomer shift $\Delta\delta$ of the second quadrupole splitting of sample #4: $\diamondsuit$, blue line: Parallel sample orientation, $\triangle$, red line: Perpendicular sample orientation.

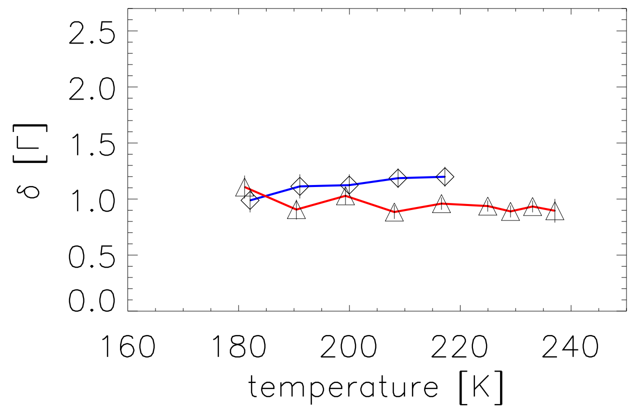

Figure 4.15: Isomer shift $\Delta\delta$ of the second quadrupole splitting of sample #5: $\diamondsuit$, blue line: Parallel sample orientation, $\triangle$, red line: Perpendicular sample orientation.

4.2.6 Fast decaying line

In addition to the principal and the second quadrupole splitting, a fast exponential decay was observed at very short delay times. Since the first 10 nanoseconds were unaccessible during the experiments, and the decay time is $\approx 0.02\,\tau_0 = 2.8$ ns this line was only visible in a very small time window. Additionally, in this time window there is also a strong contribution from the first quantum beat. The absolute fitted amplitude of the fast decaying line was normalized by (a) the total amplitude of the NFS-signal I_0, (b) the effective thickness ξ. The resulting temperature dependence is shown again in the temperature range above 140 K, starting with sample #2:

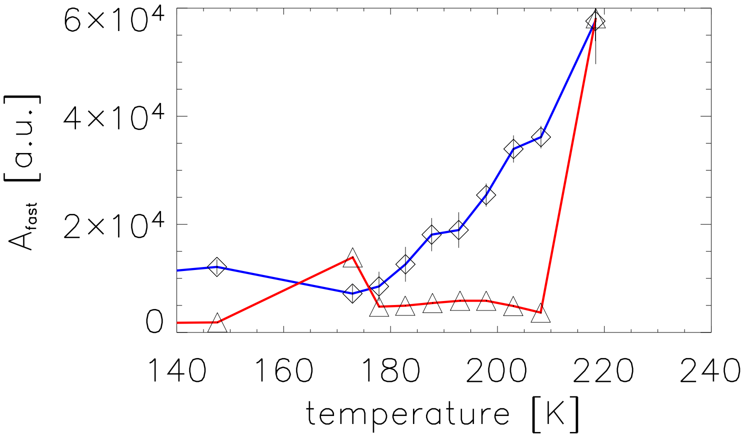

Figure 4.16: Temperature dependence of the amplitude of the fast decaying line of sample #2 ($\Diamond$: Parallel case, $\triangle$: Perpendicular case, blue / red lines are guides to the eye).

In the temperature range from 180 K to 210 K the fit may have underestimated the values in the perpendicular case of sample #2 and sample #5. In sample #4 no orientation dependence was observed. This could be attributed to the very small time window (only 10 - 20 ns) in which the fast decaying line enters the time spectra.

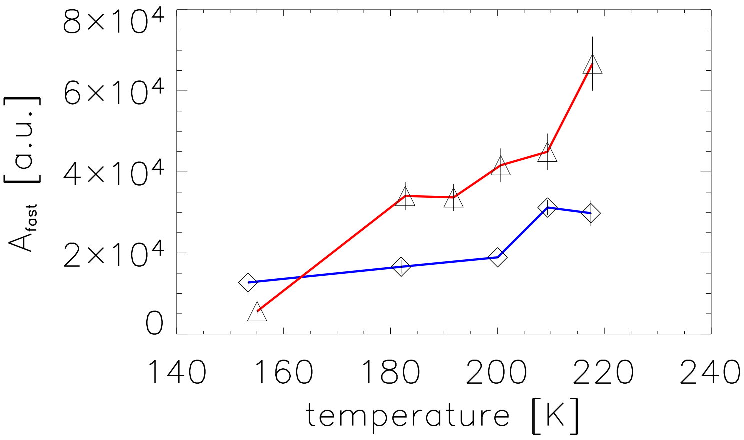

Figure 4.17: Temperature dependence of the amplitude of the fast decaying line of sample #4 (◇: Parallel case, △: Perpendicular case, blue / red lines are guides to the eye).

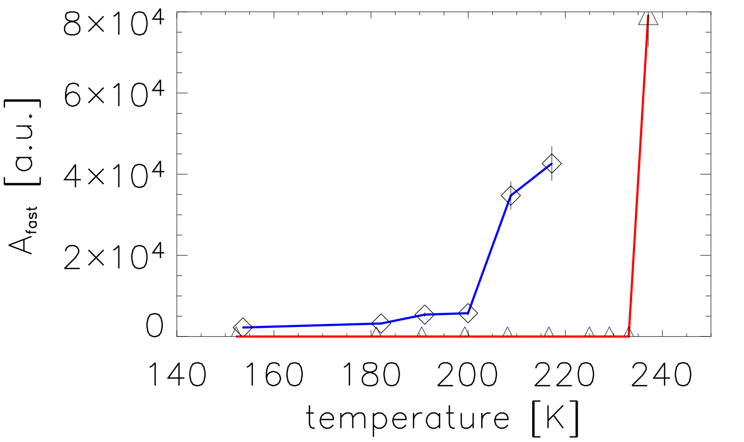

Figure 4.18: Temperature dependence of the amplitude of the fast decaying line of sample #5 (◇: Parallel case, △: Perpendicular case, blue / red lines are guides to the eye).

Based on this data we can only conclude that there *exists* a fast decaying line, but the poor sensitivity of the static model was not sufficient to resolve the line in all cases. This makes it impossible to deduct any further information, e.g. the relative amplitude of the fast decaying line compared to the amplitude of the principal and the second quadrupole splitting or if there exists any temperature dependence in the amplitude of the fast decaying line.

4.2.7 Effective thickness: Shift of T_C / Deviations from MCT

Since the Lamb-Mößbauer factor is directly proportional to the effective thickness, one can apply the MCT-prediction of square-root dependence to the resonant thickness ξ. Assuming, that only f_{LM} governs the temperature dependence of ξ the Lamb-Mößbauer factor can be extracted.

For low temperatures the data of sample #2 can be described by the Debye-model Eq. 2.6 alone. The effective vibrating mass was set to 108 atomic mass units which corresponds to ferrocene [HH97], and the corresponding Debye-temperatures as fitted in the temperature interval $75 - 150$ K were 68.2 ± 0.2 K (parallel case) and 68.4 ± 0.3 K (perpendicular case). The corresponding fit is shown in Fig. 4.19 as a dotted line:

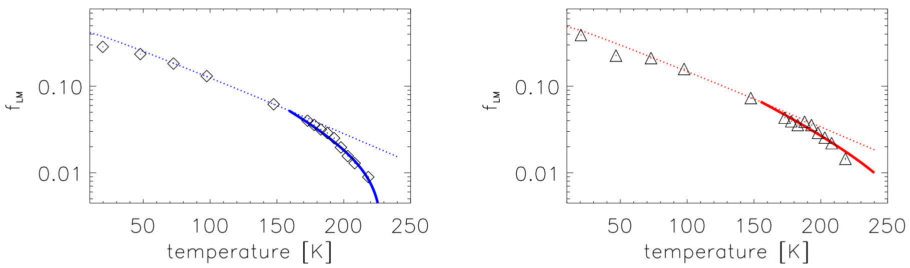

Figure 4.19: Temperature dependence of the Lamb-Mößbauer factor of sample #2 ($\diamond$: Parallel case, $\triangle$: Perpendicular case), with Debye-model (dotted blue / red line) and the corresponding fit with the square-root law from MCT (solid blue / red line). Errors are smaller than the symbols.

Above 150 K deviations from the pure Debye model are visible, which can be explained with relaxational contributions as predicted by mode-coupling theory. The corresponding fit function uses the separation ansatz Eq. 1.18 with the phononic contributions described by the Debye-model and the relaxational contributions predicted by MCT with Eq. 1.13.

In both cases there are deviations from the pure Debye model at higher temperatures. In the parallel case these deviations can be described by relaxational contributions as predicted by the square-root law of MCT, the mode-coupling critical temperature resulting from the fit is $T_C = 229 \pm 2$ K. This exceeds the value of $T_C = 205$ K for DBP:ferrocene in bulk significantly. In the perpendicular case the fit converged at $T_C = 276 \pm 7$ K.

In the case of sample #4 and #5 no data was obtained at lower temperatures, so we applied the same Debye-model with the mean Debye-temperatures of sample #2 of 68.3 K to the data. Again a fit with the square root law in both orientations was attempted (see Fig. 4.20 and 4.21):

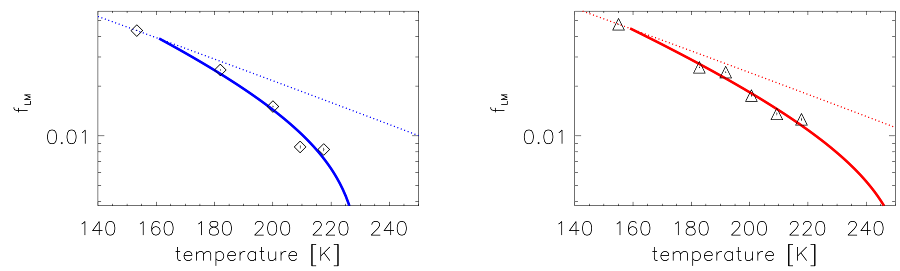

Figure 4.20: Temperature dependence of the Lamb-Mößbauer factor of sample #4 (◇: Parallel case, △: Perpendicular case), with Debye-model (dotted blue / red line) and the corresponding fit with the square-root law from MCT (solid blue / red line). Errors are smaller than the symbols.

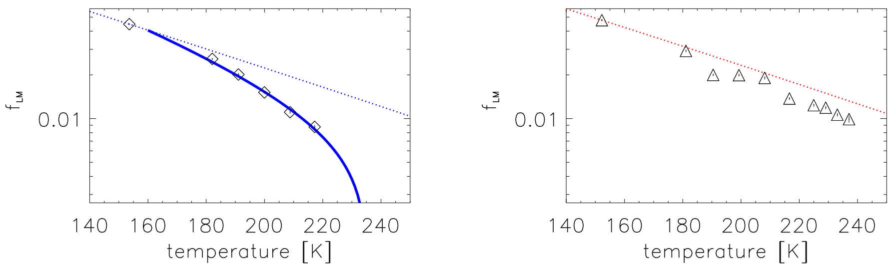

Figure 4.21: Temperature dependence of the Lamb-Mößbauer factor of sample #5 (◇: Parallel case, △: Perpendicular case), with Debye-model (dotted blue / red line) and the corresponding fit with the square-root law from MCT (solid blue line, fit was not possible in parallel case). Errors are smaller than the symbols.

The mode coupling critical temperatures resulting from the fits in the parallel orientation are $T_C = 234 \pm 6$ K (sample #4) and $T_C = 235 \pm 6$ K (sample #5), being significantly above the mode-coupling critical temperature of bulk DBP:ferrocene.

In the perpendicular case for sample #4 the effective thickness decays almost exponential, leading to a critical temperature of 258 ± 6 K. For sample #5 no critical temperature could be obtained at all. The large errors respectively the failure of the fit for sample #4 and #5 indicate that in the perpendicular direction the square-root law of MCT is either smeared out over a very large temperature range or not fulfilled at all.

4.2.8 Molecular diffusion

In the case of sample #2 no diffusion could be observed in the short time window of the limited 176 ns of 16-bunch mode. Diffusion was observed in both samples #4 and #5 during the long time window of 704 ns. The relaxation rates in units of the nuclear life time τ_0 are presented in Fig. 4.22 and Fig. 4.23:

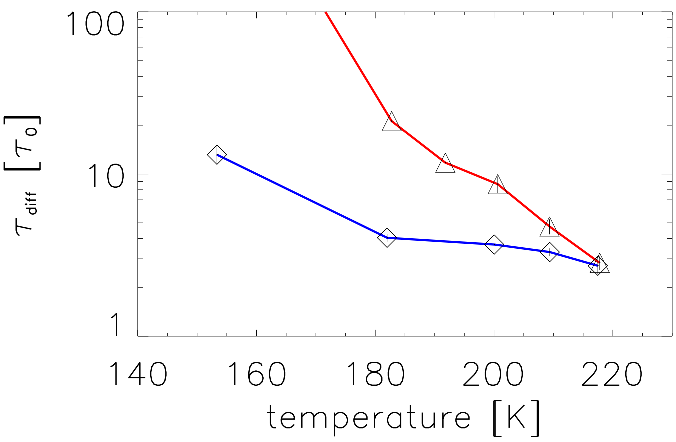

Figure 4.22: Temperature dependence of the spatial relaxation rate τ_{diff} of sample #4 ($\diamond$: Parallel case, $\triangle$: Perpendicular case).

In both cases spatial relaxation is slow, always taking place on a time scale several times larger than the nuclear life time. Fig 4.22 displays strong dependence on the orientation, and a slowing down of spatial relaxation in the perpendicular case as compared to the parallel case. In Fig 4.23 relaxation rates nearly coincide for both orientations.

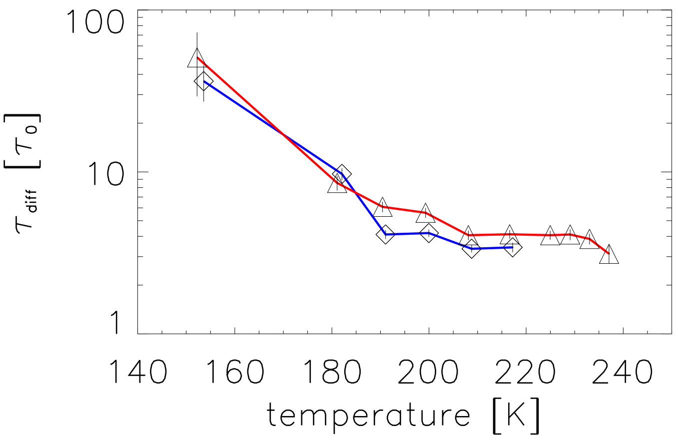

Figure 4.23: Temperature dependence of the spatial relaxation rate τ_{diff} of sample #5 ($\diamondsuit$: Parallel case, $\triangle$: Perpendicular case).

This could indicate, that relaxation is strongly anisotropic in sample #4 while it is isotropic in sample #5. The importance of measurements in sufficient long time windows (preferably covering the whole accessible time spectrum) is emphasized by these results.

5. MÖSSBAUER SPECTROSCOPY

Inspired by the finding of a second quadrupole frequency in the NFS-signals obtained during the two experiments at the ESRF additional Mößbauer spectroscopy measurements were carried out. Samples #2 and #4 were examined at the Institute of Physics at the Medical University of Lübeck.

5.1 Setup

The measurements were made with a standard Mößbauer setup in transmission geometry as can be seen in Fig. 5.1: A radioactive ^{57}Co **single line source** is mounted on a **Mößbauer drive**; emitted γ-quanta can thereby be Doppler-shifted. The sample is contained in a **cryostat**. The sample holders designed for NFS could be adapted, consequently no change of sample geometry arises. A **proportional counter** detects the transmitted radiation depending on the velocity of the source, which corresponds to an energy shift.

The cryostat was cooled with liquid nitrogen, thereby temperatures at and above 77 K were accessible for the experiment. Spectra were taken at 77 K, 180 or 190 K and 205 or 210 K for both samples and both directions.

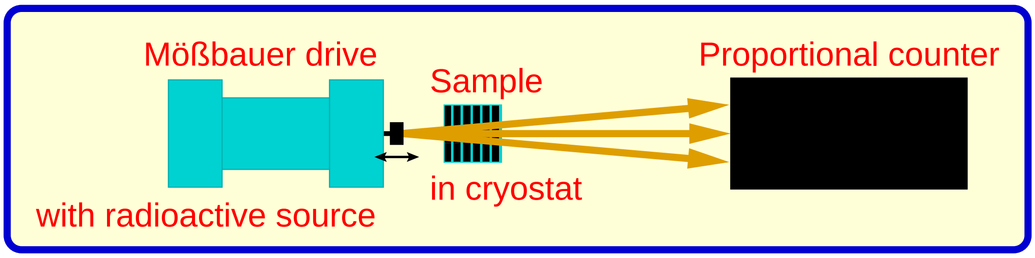

Figure 5.1: Standard setup for Mößbauer spectroscopy

Sample #2 was assembled immediately before the experiment from pSi-stripes contained in liquid DBP:ferrocene which were not used in the previous NFS-experiments. Sample #4 was the same as used for the NFS-experiments.

5.2 *Mößbauer spectroscopy with confined DBP:ferrocene*

Due to the strong absorption in the silicon matrix and the low overall ^{57}Fe content in our samples Mößbauer spectroscopy was challenging. The time needed for a single spectrum increased from at least 1 day at 77 K up to more than a week at 205 / 210 K.

5.3 *Results*

First the evaluation of the Mößbauer spectra will be described. The Mößbauer spectra will be shown together with the corresponding fits, and obvious results are presented.

5.3.1 *Data analysis*

All Mößbauer spectra were fitted with a sum of four Voigt profiles. Each line was consecutively initialized and fitted to the maxima of the remaining deviation between fit and spectrum. The result was refined by a simultaneous fit of all four lines.

5.3.2 Spectra and Fits for sample #2

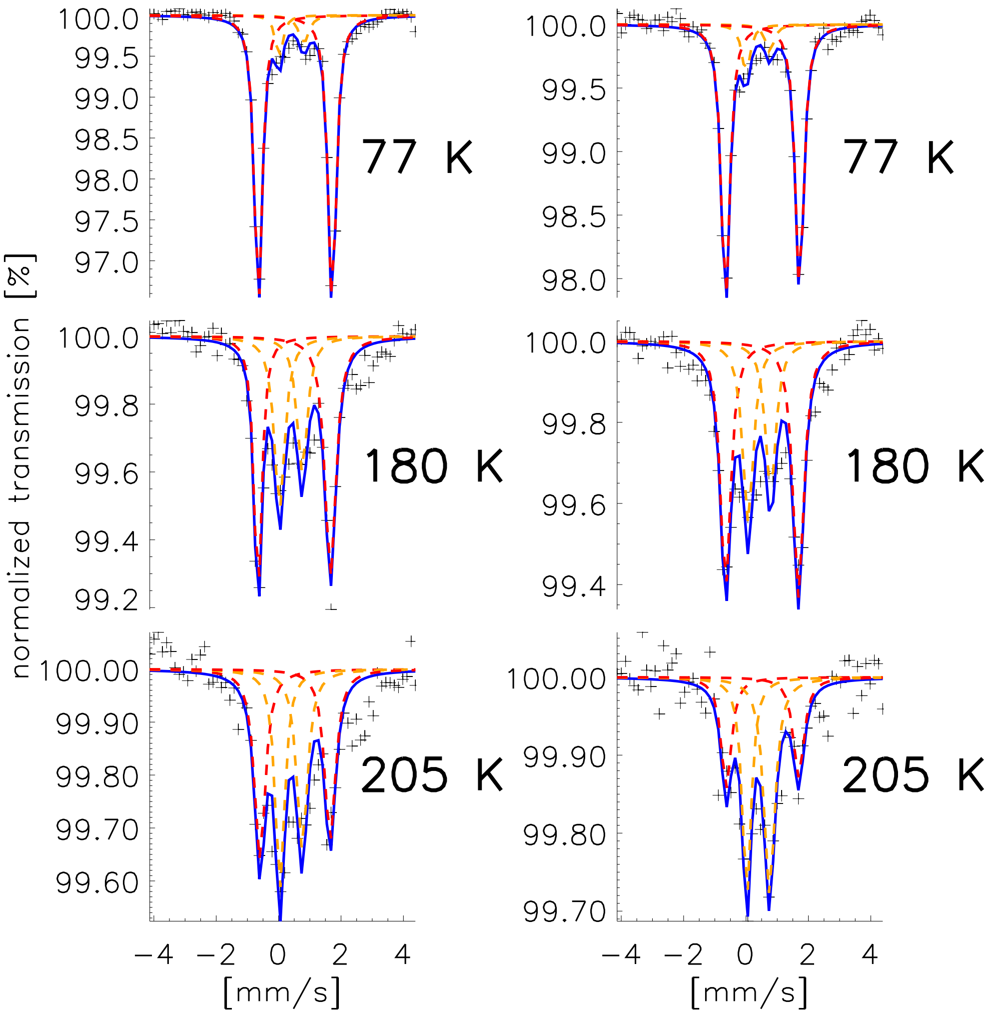

Figure 5.2: Mößbauer-spectra of sample #: +, **blue line:** Total fit, **red line:** Principal quadrupole doublet, **orange line:** Second quadrupole doublet, **left:** Parallel sample orientation, **right:** Perpendicular sample orientation

Fig. 5.2 shows the Mößbauer spectra of sample #2. The blue line is the total fit to the spectra, which is the sum of four Voigt profiles. The red lines correspond to the principal quadrupole doublet while the orange lines describe the second quadrupole doublet.

5.3.3 Spectra and Fits for sample #4

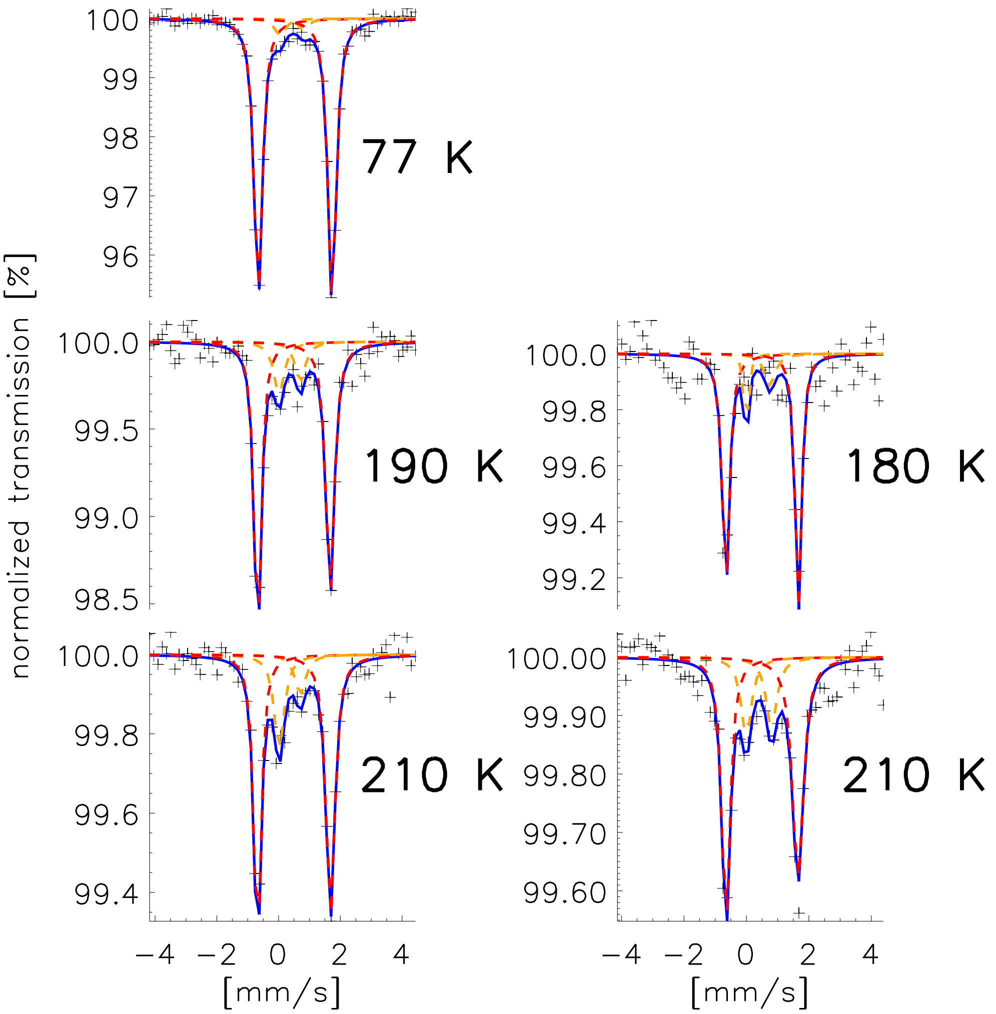

Figure 5.3: Mößbauer-spectra of sample #4: +, **blue line:** Total fit, **red line:** Principal quadrupole doublet, **orange line:** Second quadrupole doublet, **left:** Parallel sample orientation, **right:** Perpendicular sample orientation

Again the Mößbauer spectra were fitted with four Voigt profiles as can be seen in Fig. 5.3, corresponding to the red and orange lines, with the blue line being the sum of all four.

5.3.4 Principal quadrupole splitting

Fig. 5.4 displays the temperature dependence of the principal quadrupole splitting Ω, as before in units of the natural line width of ^{57}Fe.

The values at 77 K are comparable ($24.7 \pm 0.1\,\Gamma$) to the corresponding values (see Fig. 4.7) derived from the static model. At higher temperatures motional narrowing is observed. Looking at the dependence on sample orientation the situation seems to be reversed as compared to Fig. 4.7, since now motional narrowing in the parallel case appears to be stronger ($23.5 \pm 0.4\,\Gamma$) than in the perpendicular case ($24.2 \pm 1.0\,\Gamma$), but due to the rather large errors no significant differences or deviations can be determined.

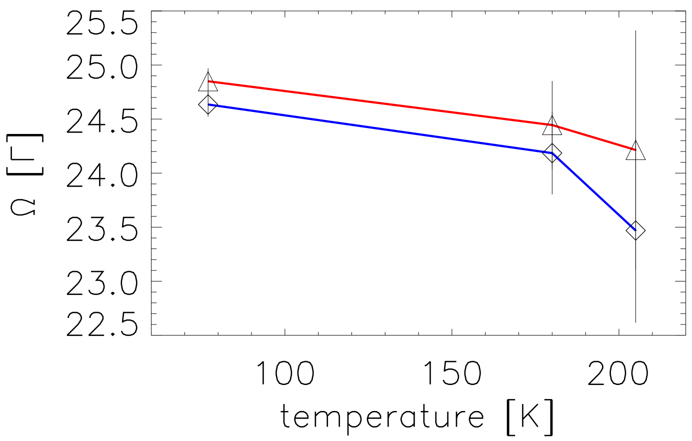

Figure 5.4: The values for the principal quadrupole splitting Ω of sample #2, $\diamond$, blue line: Parallel sample orientation, $\triangle$, red line: Perpendicular sample orientation.

While the values for the parallel case of sample #4 in Fig. 5.5 are slightly larger than those shown in Fig. 4.8, the perpendicular data matches the corresponding data.

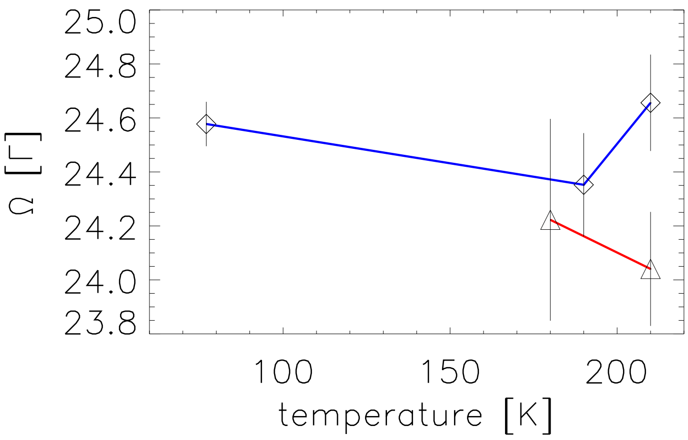

Figure 5.5: The values for the principal quadrupole splitting Ω of sample #4, ◇, blue line: Parallel sample orientation, △, red line: Perpendicular sample orientation.

5.3.5 Second quadrupole splitting

Fig. 5.6 (left) displays the relative amplitude of the inner doublet versus the sum of inner and outer doublet. The resulting values for sample #2 ($50 \pm 100\%/66 \pm 82\%$) in Fig. 5.6 (left) are significantly larger than the corresponding values derived from the static model, but show the same qualitative temperature dependence. The huge errors result from Gaussian error propagation assuming *independent* variables, which is questionable in the case of the overlapping Voigt-profiles: Reduction of the width of a line will in general lead to an increase of the width of neighboring lines, to compensate for the loss of intensity between the lines.

Fig. 5.6 (right) shows the value of the second quadrupole splitting. It decreases from $8.1 \pm 0.5\,\Gamma/7.9 \pm 1\,\Gamma$ (parallel / perpendicular case) down to $7.4 \pm 0.7\,\Gamma/7.6 \pm 0.6\,\Gamma$.

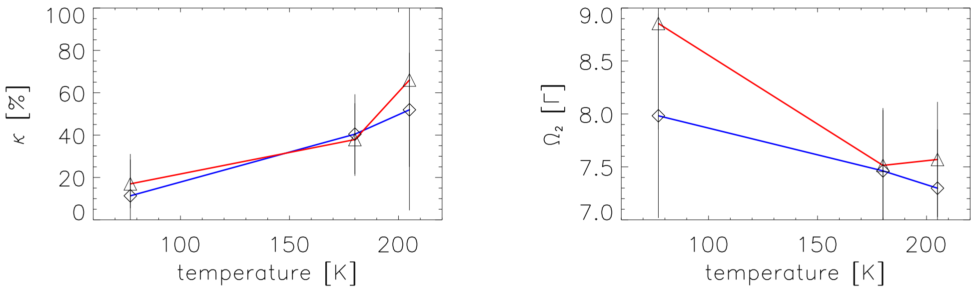

Figure 5.6: Temperature dependence of the second quadrupole splitting of sample #2: ◇, blue line: Parallel sample orientation, △, red line: Perpendicular sample orientation.

The relative fractions for sample #4 are 22±52%/24±28% in the parallel / perpendicular case shown in Fig. 5.7, which is in quantitative agreement with the results shown in Fig. 4.11.

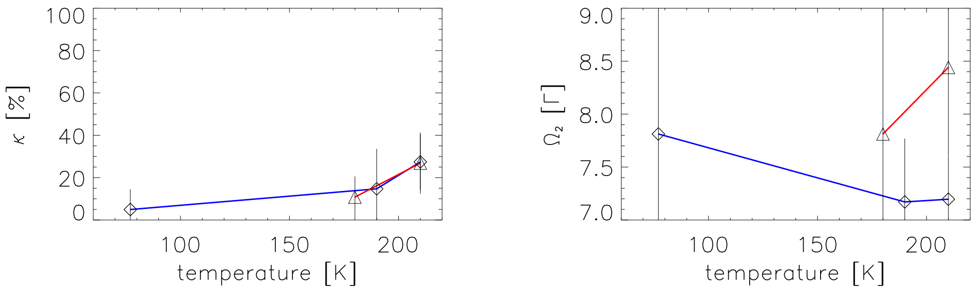

Figure 5.7: Temperature dependence of the second quadrupole splitting of sample #4: ◇, blue line: Parallel sample orientation, △, red line: Perpendicular sample orientation.

5.3.6 *Isomer shift of the second quadrupole splitting*

Neither the isomer shift of the outer (Fig. 5.8 (left)) nor the inner doublet (Fig. 5.8 (right)) of sample #2 show a temperature dependence. But

Mößbauer spectroscopy revealed that there exists a significant difference in the isomer shift: While the value of the outer doublet of $\delta = 5.4 \pm 0.1\Gamma$ agrees with the literature value of $5.52\,\Gamma$ [GG71], the IS of the inner doublet is only $\delta = 4.2 \pm 0.1\,\Gamma$. This corresponds to a difference of $\Delta\delta = 1.2 \pm 0.2$.

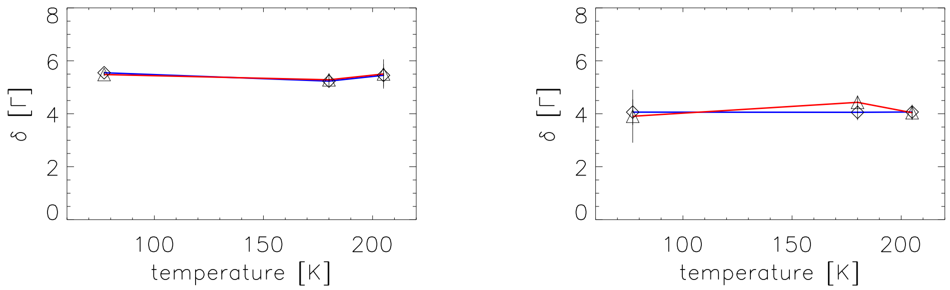

Figure 5.8: Isomer shift of the outer (left) and inner doublet of #2: $\Diamond$, **blue:** Parallel sample orientation, $\triangle$, **red:** Perpendicular sample orientation.

The situation is qualitatively the same for sample #4 as shown in Fig. 5.9: $\delta = 5.3 \pm 0.1\,\Gamma$ / $3.9 \pm 0.3\Gamma$ for the outer / inner doublet, with $\Delta\delta = 1.2 \pm 0.3$.

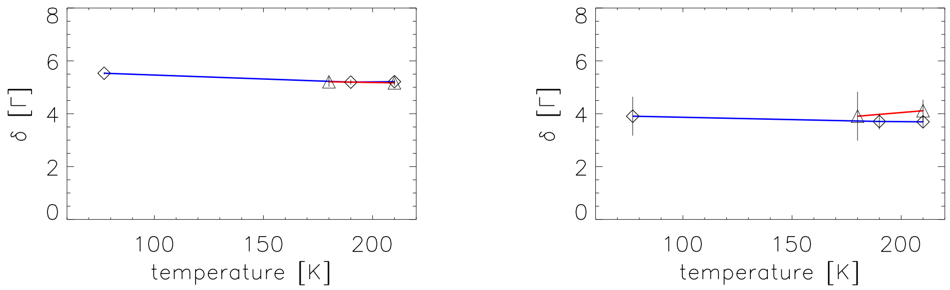

Figure 5.9: Isomer shift of the outer (left) and inner doublet of #4: $\Diamond$, **blue:** Parallel sample orientation, $\triangle$, **red:** Perpendicular sample orientation.

5.3.7 Lamb-Mößbauer factor

Fig. 5.10 displays the temperature dependence of the Lamb-Mößbauer factor of the outer doublet (left) and inner doublet. While the outer doublet shows a strong decrease of up to one order of magnitude (which is in very good qualitative agreement with the temperature dependence of the Lamb-Mößbauer factor derived from the static model), the recoilless fraction of the inner doublet stays approximately constant or even rises.

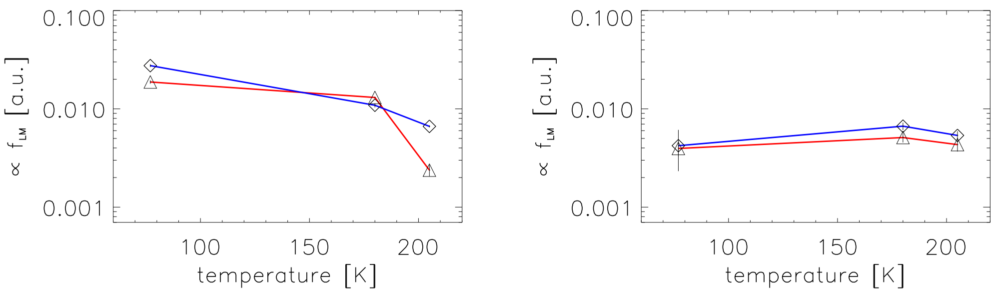

Figure 5.10: Amplitudes of the outer (left) and inner doublet of #4: $\diamond$, **blue:** Parallel sample orientation, $\triangle$, **red:** Perpendicular sample orientation.

Fig. 5.11 (left) shows the same qualitative temperature dependence for sample #4 as already observed in sample #2: A decrease of f_{LM} of approximately one order of magnitude of the outer doublet from 77 K down to 210 K, while the Lamb-Mößbauer factor for the inner doublet stays nearly constant.

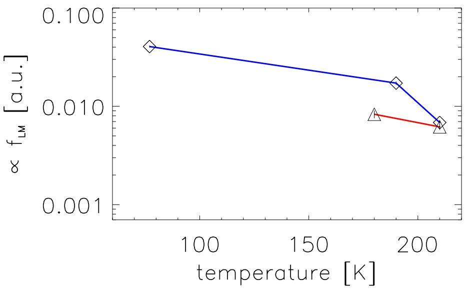

Figure 5.11: Amplitudes of the outer (left) and inner doublet of #4: $\diamondsuit$, **blue:** Parallel sample orientation, $\triangle$, **red:** Perpendicular sample orientation.

5.3.8 Additional line broadening

In principle relaxational dynamics can be detected with Mößbauer spectroscopy due to an additional line broadening. To actually measure the small deviations it would of course require an accurate determination of the line width in absence of any diffusional dynamics.

As can be seen in Fig. 5.12 the line width of the outer doublet (3.2 Γ / 3.8 Γ) is considerably larger than the expected line width of 2 Γ, but this deviation may be explained by the solution of ferrocene in DBP which leads to a broadening of the line to 0.35 mm/s = 3.6Γ, which is in very good agreement with the experimental data [Leu04]. The width then increases to (6.0 Γ / 5.3 Γ).

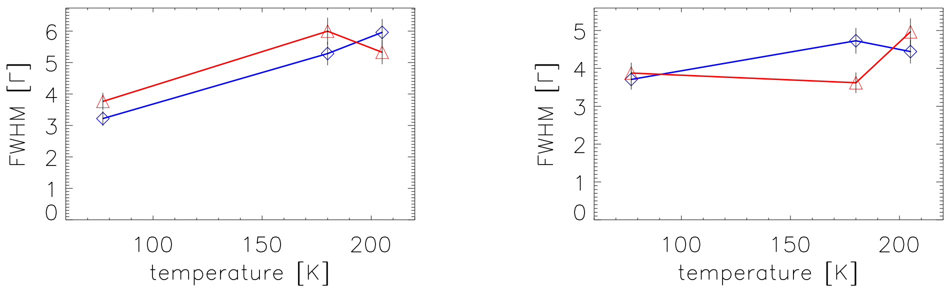

Figure 5.12: Line width of the outer (left) and inner doublet of #2: $\diamondsuit$, **blue:** Parallel sample orientation, $\triangle$, **red:** Perpendicular sample orientation.

On the opposite side the width of the inner doublet lines shows an additional broadening, without or with only a weak temperature dependence.

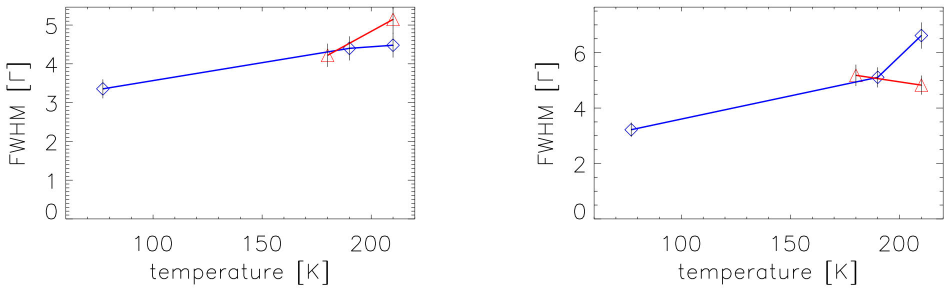

Figure 5.13: Line width of the outer (left) and inner doublet of #4: $\diamondsuit$, **blue:** Parallel sample orientation, $\triangle$, **red:** Perpendicular sample orientation.

In sample #4 both doublets show additional broadening at higher temperatures.

6. X-RAY ABSORPTION NEAR EDGE STRUCTURE EXPERIMENTS

X-ray Absorption Near Edge Structure or short **XANES** can give information about the oxidation state of a scattering atom. Since Ozin et al. [OG89] and Toda et al. [TII$^+$04] reported increased oxidation rates of ferrocene in different types of nanoporous media the question remains whether oxidation may have taken place in our samples, too. Consequently, we performed XANES experiments to determine the oxidation state of the iron in our samples.

The transmission of X-rays through a sample of thickness d can be written as $I = I_0 \exp(-\mu d)$ with μ being the absorption coefficient. Far away from any absorption edges μ can be described by $\mu \propto \frac{Z^x}{E^3}, \quad 3 < x < 4$. If additional electrons can be excited μ rises steeply with increasing energy, leading to an edge in the absorption coefficient.

The area immediately below and above (several 10 eV) the absorption edge shows features caused by the symmetry of the absorbing atom and its electronic configuration. This region is usually called the XANES-region. At higher energies the Extended X-ray Absorption Fine Structure or EXAFS-region continues, which is dominated by resonances caused by backscattering of the photoelectron from the surrounding atoms.

The exact position of the edge is connected to the oxidation state of the scattering atom, leading to shifts of the absorption edge to higher energies in the eV-range with increasing oxidation [BOJ$^+$03]. XANES can thereby give element specific information about the oxidation state.

6.1 Setup

Measurements were made at the beamline E4 at HASYLAB / DESY. A standard XANES-setup was used (see Fig. 6.1):

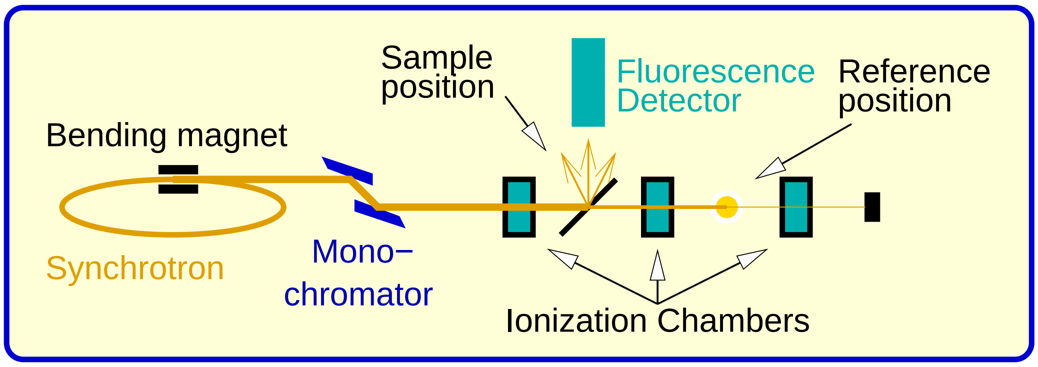

Figure 6.1: Standard setup for XANES / EXAFS experiments

The synchrotron radiation is monochromatized by two Si-(1 1 1) crystals. The monochromator is stabilized and uses encoders to reproducibly scan large energy ranges.

The transmission of a sample is measured as the intensity detected in the second ionization chamber (IC) divided by the intensity measured in the first IC, a reference sample can be measured at the same time between the second and the third IC.

Samples #2, #4 and #5 have been examined together with a reference of bulk DBP:ferrocene. Due to the high absorption of the sample only one to three stripes were used in the experiment. Because the examined samples contain only a very dilute amount of iron an energy-resolving germanium detector was used to measure the excited fluorescence of the K-electrons, which is directly proportional to the absorption coefficient μ.

6.2 Results

To enable a direct comparison of the fluorescence data from the sample and the transmission data from the reference a normalization was done. The reciprocal transmission data was scaled to the fluorescence background at 7110 eV and the maximum intensity between 7125 - 7145 eV.

6.2.1 XANES-spectra

For each sample at least three energy-scans have been measured to estimate the reproducibility of the spectra. All scans of a sample and the reference are plotted in one figure. In Fig. 6.2 the XANES-region of sample #2 is plotted in red against the reference in blue:

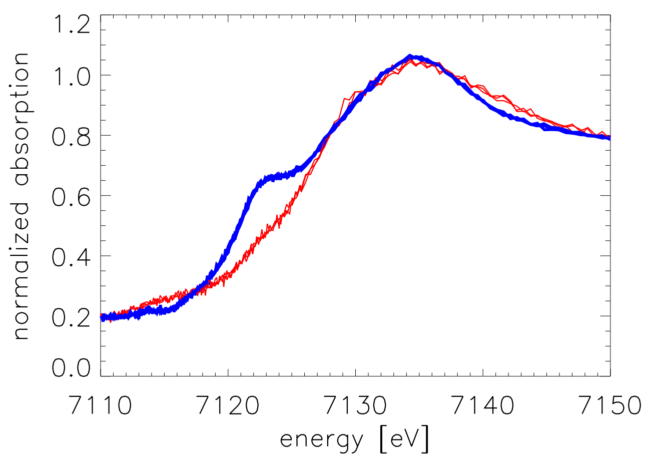

Figure 6.2: Red line: XANES-region of sample #2:, **Blue line:** Reference sample bulk DBP:ferrocene

Two major differences are visible: The pre-peak which is present in the reference sample at $\approx$ 7122 eV has essentially vanished, and there is a small amount of excess intensity from 7138 - 7145 eV. The remaining XANES-spectra coincide with the spectra measured with the reference sample.

Fig. 6.3 and 6.4 display the spectra for samples #4 and #5. The pre-peak is visible, but has significantly decreased intensity. The remaining XANES-spectra coincide with corresponding spectra obtained from the reference sample.

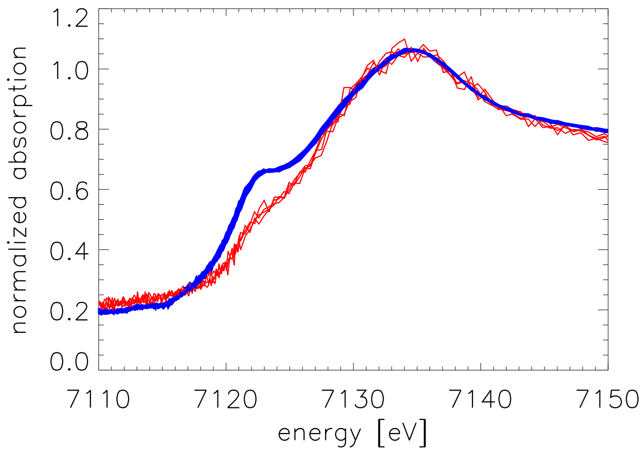

Figure 6.3: Red line: XANES-region of sample #4:, **Blue line:** Reference sample bulk DBP:ferrocene

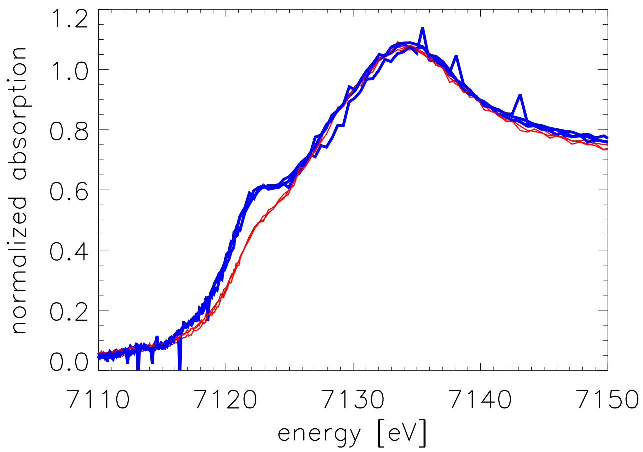

Figure 6.4: Red line: XANES-region of sample #5:, **Blue line:** Reference sample bulk DBP:ferrocene

6.2.2 Intensity of the pre-peak

In all three samples the intensity of the pre-peak is reduced. According to Ruiz-Lopez et al. [RLLG+88] this peak is a shape resonance caused by the 10 carbon-atoms surrounding the iron in the ferrocene-molecule, and the existence of this peak is "quite sensitive to small variations of the metal...C bond length" [RLLG+88]. Thereby the vanishing of the pre-peak can be attributed to a possible distortion of the ferrocene molecule.

6.2.3 Position of the absorption edge

To estimate the position of an absorption edge usually the *maximum of the first derivative* is used. In our case this proved difficult due to the varying intensity of the pre-peak. Since we are only interested in the shift of the absorption edge relative to a reference-sample the evaluation was restrained to the determination of the *maximum of absorption* in sample and reference. For this purpose a Gaussian was fitted to the maximum of each spectrum; the resulting positions of the maximum and the corresponding shifts are displayed in Tab. 6.1:

	#2 [eV]	**#4 [eV]**	**#5 [eV]**
Sample	7135.3 ± 0.1	7134.7 ± 0.1	7134.39 ± 0.02
Reference	7135.00 ± 0.08	7134.76 ± 0.08	7134.7 ± 0.3
Shift	0.3 ± 0.2	0.0 ± 0.2	-0.3 ± 0.3

Table 6.1: Position of the absorption maximum for different samples

In all cases the shift is of the order of the statistical error.

The decrease of the pre-peak is obviously the strongest in sample #2. A strong distortion of the ferrocene-molecule will at some point also start to influence the EXAFS-region, which could explain the deviations from the reference data.

In total **no significant shift** of the absorption edge could be detected in any sample, thereby we do not measure any change of the iron oxidation state.

7. MODELLING OF RESULTS

In this chapter models for the observed QNFS- and Mößbauer-spectra are presented. As was already shown in chapter 2.6 that an anisotropic relaxation of the EFG may lead to a partially reduced quadrupole splitting [Gib76]. Consequently it was attempted to explain the existence of the second quadrupole splitting by anisotropic rotation of ferrocene-molecules in the theoretical part. The QNFS datasets were modelled by an implementation of the generalized Kubo-Anderson algorithm called MONDIA provided by Mati Haas (Institute of Physics at the University of Tartu, Finland) and Heiner Winkler (Institute of Physics of the Medical University of Lübeck). MONDIA is based upon the SYNFOS algorithm [HRW$^+$00].

7.1 Anisotropic relaxation: The MONDIA approach

In 1976 Gibb reported partial motional narrowing of the quadrupole splitting of ferrocene confined in urea-clathrates [Gib76]. He explained this by anisotropic relaxation of the molecular EFG as presented in chapter 2.6.

To model anisotropic relaxation numerically, the program MONDIA was used. MONDIA stands for MONocrystalline and DIAmagnetic, since it is an adaption of SYNFOS to our special, monocrystalline sample structure. Initially MONDIA was only capable of producing single time-spectra, but was incorporated into a fitting algorithm.

MONDIA in its final implementation calculates a coherent superposition of the radiation scattered by a user-defined number of relaxation centers. Each of these centers is defined by a set of parameters including:

- Statistical weight,
- Orientation of three EFG-states relative to the beam,
- Configurational energy (corresponds to the population p_x, p_y and p_z of the three EFG-states),
- Quadrupole splitting and asymmetry parameter for the three EFG-states,
- jump rates for the three EFG-states (corresponds to W_{xy}, W_{xz} and W_{yz}).

Thus for each relaxation center at least 16 parameters are necessary. At least three different relaxation centers (corresponding to the two different quadrupole doublets and the fast decaying line already used in the static model) are needed to model the time spectra.

Since each step of the fitting procedure needs the partial derivative of each variable parameter, and each single call of MONDIA takes nearly one second the number of variable parameters had to be reduced to a minimum to make fitting feasible on a timescale of hours to days.

For each center the Eulerian angles of the three EFG-sites have to be defined; these were chosen to resemble three orthogonal orientations of the EFG. The orientation of these three states could be further altered by a rotation affecting the whole sample at once. This rotation is defined in the laboratory system: The beam-direction designates the z-axis of the system, the x-axis coincides with the polarization axis (see Fig. 7.1). Thereby the transition between parallel and perpendicular orientation of the sample could be realized by a change of the crystal Eulerian angles from $[0, 0, 0]$ to $[90, 90, 0]$.

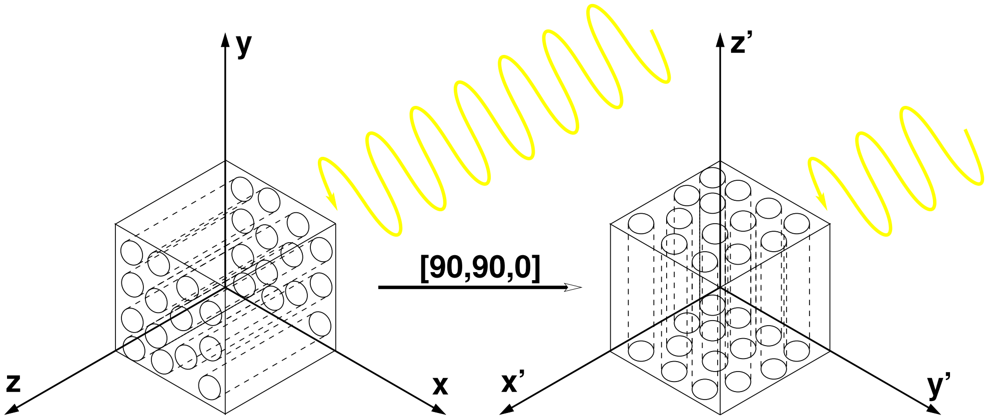

Figure 7.1: Transition of the sample in parallel orientation in the coordinate system spanned by $(\mathbf{x}, \mathbf{y}, \mathbf{z})$ is achieved by a 90° rotation around the **z**-axis, then a 90° rotation around the new **y**-axis. The final orientation of the pore axis is perpendicular to the beam-direction (designated by the old **z**-axis), the resulting sample coordinate system $(\mathbf{x}', \mathbf{y}', \mathbf{z}')$ is displayed on the right hand site.

As was shown in 4.2.3 the principal quadrupole splitting does not strongly depend upon orientation of the sample. The angular dependence was consequently omitted by using a single quadrupole splitting for all relaxation centers and orientations of the EFG, reducing the number of fit parameters.

The **first center** models the amount of frozen in bulk-like ferrocene dissolved in DBP. Thereby the jump rates and the asymmetry parameters were fixed at 0.. The statistical weight was fixed at 1.0, thereby all other weights are given in relative units compared to the first center.

The **second center** corresponds to a fraction of ferrocene molecules rotating isotropically, thereby leading to a fast decaying exponential line. The jump rates were set to fixed values ($W_{xy} = W_{xz} = W_{yz} = 1.0\ \hbar\Omega$) after initial testing.

The **third center** corresponds to anisotropically rotating ferrocene, causing the incomplete reduction of the quadrupole splitting. Values for the jump rates were obtained by initial testing and then fixed at $W_{xy} = 0.8\ \hbar\Omega$, $W_{xz} = 0\ \hbar\Omega$ and $W_{yz} = 25.0\ \hbar\Omega$. To model quadrupole splitting below 1/2 of the principal quadrupole splitting the asymmetry parameters had to allowed to be set to non-zero values.

The amplitudes from these three types of scattering centers are added up *coherently* and yield the NFS-signal. It has to be stressed that since we did not apply any distribution function to jump rates, quadrupole splittings or asymmetry parameters, this sum is only capable of answering *if* the experimental data can be modelled by anisotropic relaxation, but the result must not be unique.

The statistical weights include two different factors: First, the number density of relaxation centers; second, the Lamb-Mößbauer fraction of these relaxation centers. While the number density can not be orientation dependent, the Lamb-Mößbauer factor could be depending on the orientation of the incident angle of radiation.

Since we already observed that the statistical weights and the fraction of the second quadrupole splitting exhibit a strong orientation dependence it is obvious that we have to assume different statistical weights (and thereby different Lamb-Mößbauer factors) of the centers two and three in both orientations.

7.2 Results from MONDIA

The data sets were fitted with the model implemented by MONDIA as explained above in the following procedure:

- Only the first center corresponding to bulk-like DBP:ferrocene was fitted to the data, the statistical weights of the other centers was set to 0 and fixed. Normalization of the data was done in the same way as for the static model.
- The second and third center were added, with fixed transition rates and free values for the asymmetry parameters η.
- The η-values were fixed at the best overall values, and the fit was refined with these values.

In the following exemplary fits for selected temperatures are shown, and the results of the MONDIA-fit are compared with the static model.

7.2.1 Fits with MONDIA

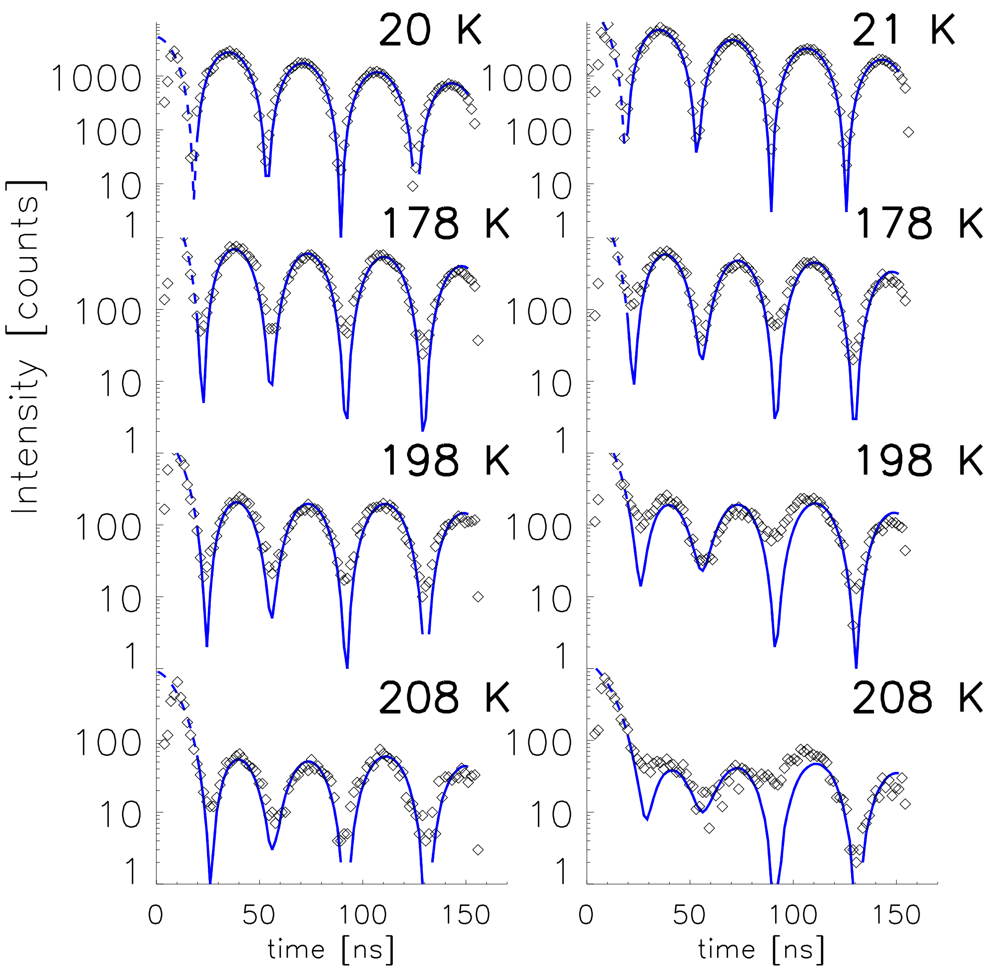

Figure 7.2: NFS-Signal of sample #2: $\diamond$, **Left:** Parallel sample orientation, **right:** Perpendicular sample orientation. **Blue line:** MONDIA-fit to the data.

Fig. 7.2 shows the fit with MONDIA for the same selected temperatures as before in the static model. While the static model fitted all data sets independently, MONDIA took the rotation of the sample properly into account and was therefore capable of fitting both orientations simultaneously.

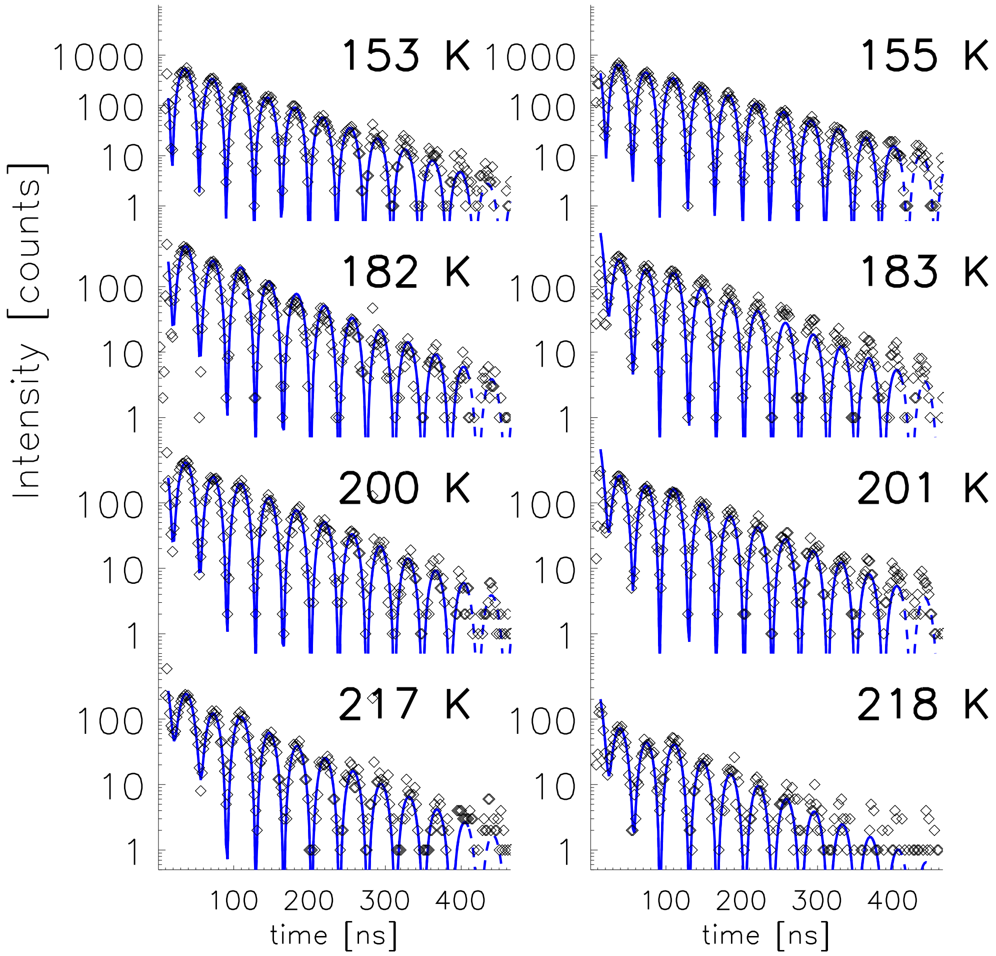

Figure 7.3: NFS-Signal of sample #4: $\diamond$, **Left:** Parallel sample orientation, **right:** Perpendicular sample orientation. **Blue line:** MONDIA-fit to the data.

Fig. 7.3 and 7.4 show very good agreement of experimental data and the fit by MONDIA. Again, both orientations of the sample were fitted simultaneously[1].

[1] The peak in the intensity in the data sets at around 300 ns was excluded from the fit as before for the static model fits.

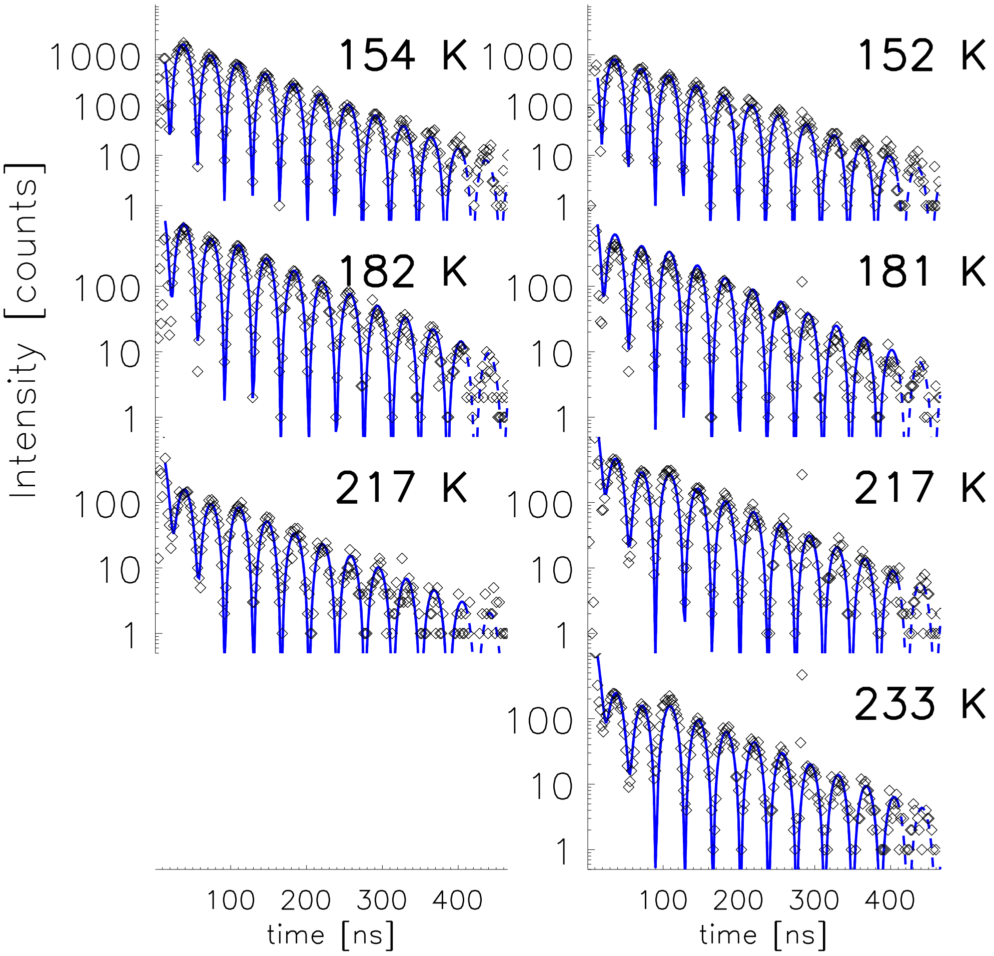

Figure 7.4: NFS-Signal of sample #5: $\diamond$, **Left:** Parallel sample orientation, **right:** Perpendicular sample orientation. **Blue line:** MONDIA-fit to the data.

7.2.2 Principal quadrupole splitting

As can be seen in Fig. 7.5 the quadrupole splitting of sample #2 behaves almost exactly as expected for an averaged value of both orientations as seen in the results from the static model: Starting from $24.8 \pm 0.1\,\Gamma$ at 20 K we again observe motional narrowing down to $23.8 \pm 0.1\,\Gamma$ at 218 K.

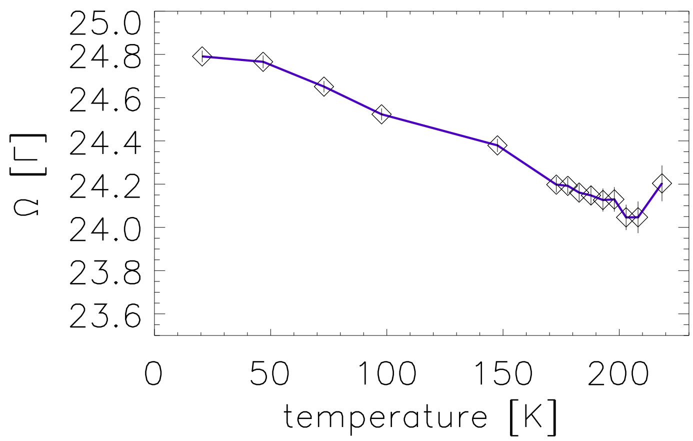

Figure 7.5: Values for the principal quadrupole splitting Ω of sample #2 derived from the fit with MONDIA: $\diamond$, purple line: Guide to the eye

The values of the principal quadrupole splitting as shown in Figs. 7.6 and 7.7 also correspond to those resulting from the static model with the exception of a constant offset of 0.2 Γ. Apart from this the temperature dependence is essentially the same: For sample #4 the quadrupole splitting reduces from $24.6 \pm 0.1\,\Gamma$ down to $24.3 \pm 0.1\Gamma$, for sample #5 it reduces from $24.7 \pm 0.1\,\Gamma$ down to $24.3 \pm 0.1\,\Gamma$.

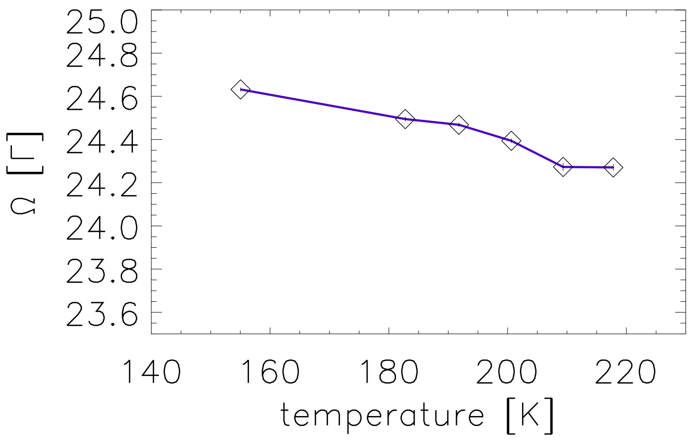

Figure 7.6: Values for the principal quadrupole splitting Ω of sample #4 derived from the fit with MONDIA: ◊, purple line: Guide to the eye

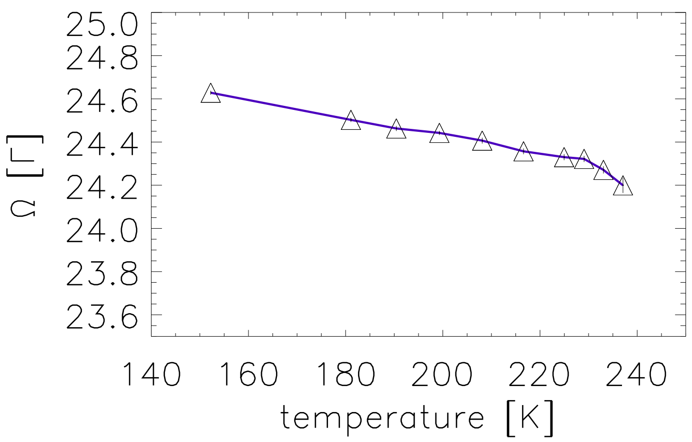

Figure 7.7: Values for the principal quadrupole splitting Ω of sample #5 derived from the fit with MONDIA: ◊, purple line: Guide to the eye

7.2.3 Onset of anisotropic rotation

The onset of anisotropic rotation in the static model is observed via the increase of the fraction of the second quadrupole splitting, while in the MONDIA-model it is introduced by the rise in the statistical weight of the third center of relaxation. To make the comparison easier the statistical weights were converted to fractions $\kappa = \frac{\text{Third relax. center}}{\text{First r.c. + Third r.c.}}$. Since we already observed with aid of the static model that the Lamb-Mößbauer factor is anisotropic in porous silicon we had to assume an orientational dependence of the statistical weights, as can be seen in Fig. 7.8, Fig. 7.9 and Fig. 7.10:

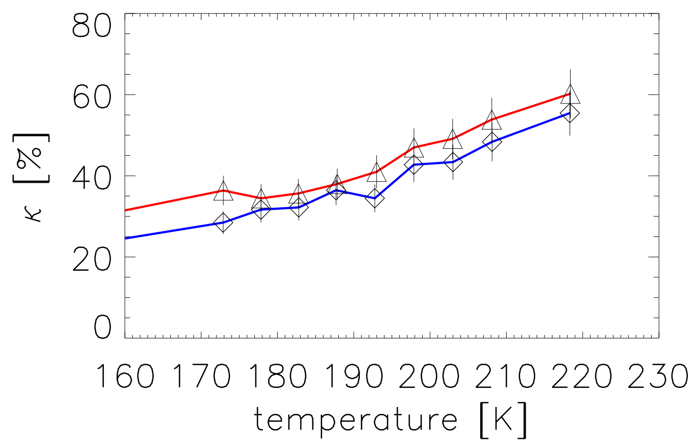

Figure 7.8: Statistical weight κ of the third relaxation center of sample #2 derived from the fit with MONDIA: $\diamond$, blue line: Parallel sample orientation, $\triangle$, red line: Perpendicular sample orientation.

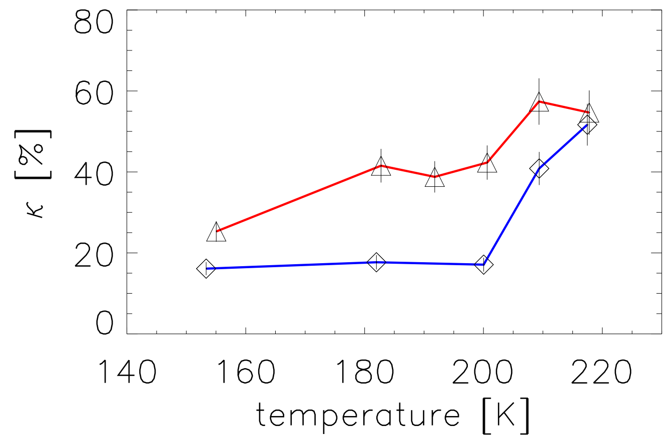

Figure 7.9: Statistical weight κ of the third relaxation center of sample #4 derived from the fit with MONDIA: $\diamondsuit$, blue line: Parallel sample orientation, $\triangle$, red line: Perpendicular sample orientation.

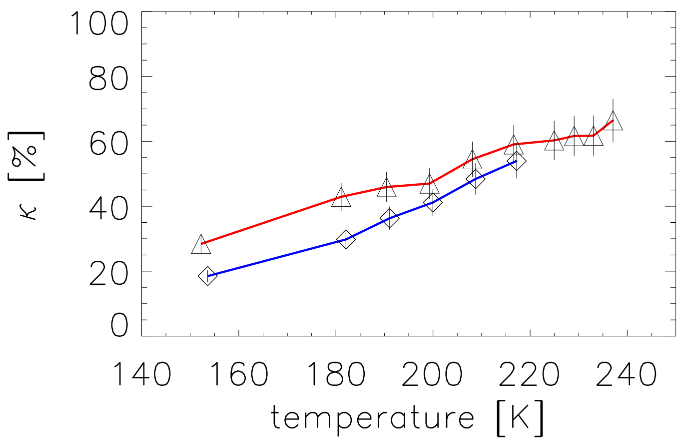

Figure 7.10: Statistical weight κ of the third relaxation center of sample #5 derived from the fit with MONDIA: $\diamondsuit$, blue line: Parallel sample orientation, $\triangle$, red line: Perpendicular sample orientation.

In all cases the statistical weight of the third relaxational center is increased in the perpendicular orientation.

7.2.4 Onset of isotropic rotation

The results for the fraction showing isotropic rotation were converted to fractions $\kappa = \frac{\text{Second relax. center}}{\text{First r.c. + Second r.c.}}$, as before in the case of anisotropic rotation.

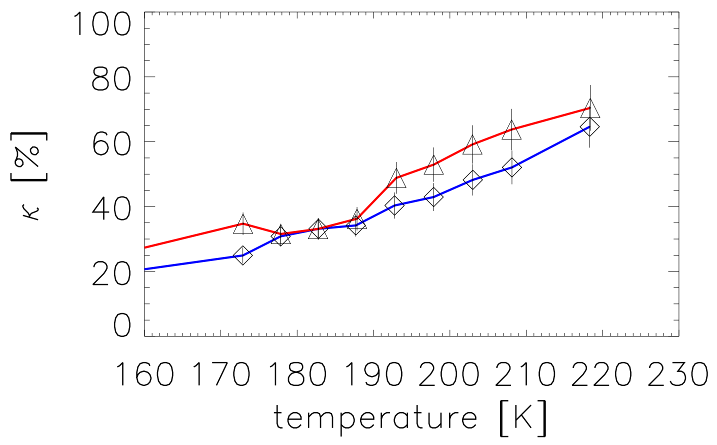

Figure 7.11: Statistical weight κ of the second relaxation center of sample #2 derived from the fit with MONDIA:$\diamondsuit$, blue line: Parallel sample orientation, $\triangle$, red line: Perpendicular sample orientation.

Also the fraction of the second relaxation center attributed to molecules undergoing isotropic rotation increases with raising temperature. While it was not possible to derive any orientation dependence from the static model, the MONDIA model consistently shows that the statistical weight of isotropic rotation is always larger in the perpendicular case, as before in the case of anisotropic rotation.

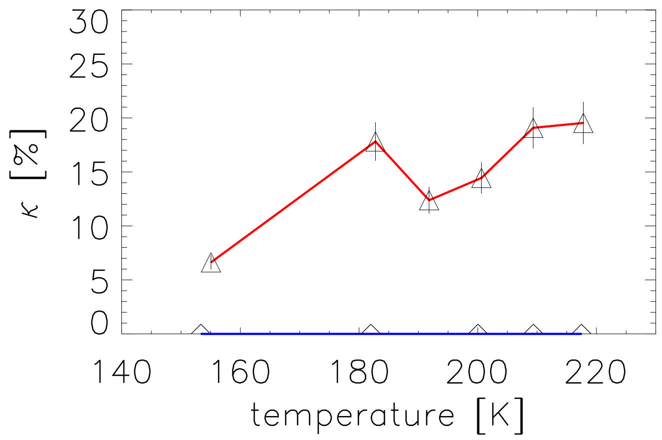

Figure 7.12: Statistical weight κ of the second relaxation center of sample #4 derived from the fit with MONDIA:$\diamondsuit$, blue line: Parallel sample orientation, $\triangle$, red line: Perpendicular sample orientation.

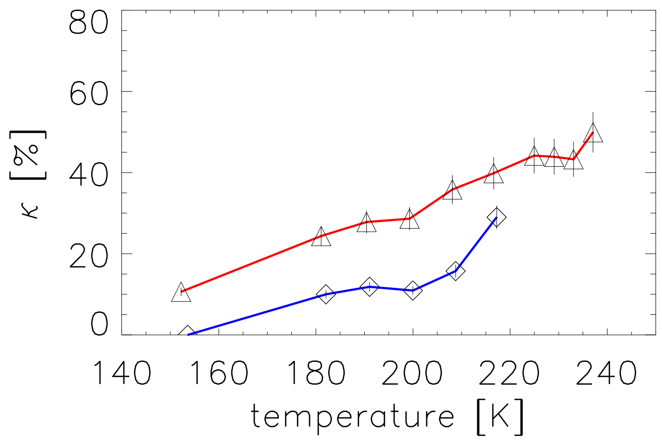

Figure 7.13: Statistical weight κ of the second relaxation center of sample #5 derived from the fit with MONDIA: $\diamondsuit$, blue line: Parallel sample orientation, $\triangle$, red line: Perpendicular sample orientation.

8. DISCUSSION

In this chapter the findings presented in the former chapters will be linked and discussed. First the origin of additional spectroscopic components will be addressed. In the second part the observed dynamics is interpreted in the scope of mode-coupling theory of the glass transition.

8.1 Origin of the reduced quadrupole doublet

In the preceding chapters the experimental data on the dynamics was presented both in time and energy domain. Using NFS one fraction which produced the ***quadrupole beating of bulk ferrocene*** **(1)**, a second one which generated a ***fast decaying line*** **(2)** and a third one with a ***significantly decreased quadrupole beating frequency*** and an additional small phase shift **(3)** were detected. With Mößbauer spectroscopy the corresponding quadrupole doublet of bulk ferrocene (1) and a reduced quadrupole doublet (3) were observed[1].

We have no difficulties to understand the existence of the first spectroscopic component, which is caused by static ferrocene. *Chemical* or *dynamical* effects could explain the appearance of the spectroscopic components (2) and (3): A ***change of the valence state*** of the iron atom in ferrocene would directly result in a change of the quadrupole splitting and isomer shift; the possibility of a valence state change will be addressed in the first part of this chapter. As was shown in chapter 2.6 also rotational dynamics of molecules can lead to motional narrowing of a quadrupole doublet. A model

[1] The broad background corresponding to the fast decaying line (2) could not be resolved because of the low overall statistics and the small energy window chosen.

of ***anisotropic relaxation*** of ferrocene will be discussed in the second part of this chapter.

8.2 Chemical change of the valence state

In 1994 evidence for a ***mixing of the valence state*** of ferrocene was presented by Wagener et al. [WHF+94]. Consequently the possibility of a change of the valence-state of ferrocene in the presented experiments is reviewed first.

In addition Ozin et al. [OG89] and Toda et al. [TII+04] reported increased ***oxidation*** rates of ferrocene in mesoporous matrices leading to ferrocenium. These models could also explain the existence of a second, smaller quadrupole doublet, and are consequently discussed in the second part of this section.

8.2.1 Mixing of the valence-state of ferrocene

Wagener et al. reported Mößbauer spectroscopy measurements on ferrocene incorporated in several polymers showing not only the typical quadrupole splitting of $24.35\,\Gamma$ but also an additional second quadrupole splitting of $\approx 8.5\,\Gamma$. Its isomer shift is $\approx 0.5 - 1.0\,\Gamma$ relative to ferrocene, which could indicate iron in a (III)-valence state in contrast to iron in ferrocene having (II)-valence.

The temperature dependence of this inner doublet suggests that the number of molecules contributing to this doublet increases with rising temperature. In addition the inner doublet is broadened, but since this broadening is not temperature dependent it is attributed to static inhomogeneities instead of being of relaxational origin.

Wagener et al. explained this by two species of iron atoms in their sample: Iron atoms in structure S_1 produce the ferrocene quadrupole doublet in the whole temperature region, while atoms in structure S_2 may transit between (II)- and (III)-valence states with increasing temperature. For this purpose an *unoccupied molecular orbital* is assumed to be very close to the highest occupied molecular orbital.

The resulting formalism is then used to describe the experimental spectra as a sum of iron atoms of mixed valence. Wagener et al. observed a doubling of the resonating mass and concluded that this suggests a *binding between two ferrocene units*. Since the overall amount of iron in structure S_2 increased significantly when the samples were exposed to air and daylight this binding was interpreted to be rather stable.

Setting aside the unsolved question of the unoccupied molecular orbital assumed by Wagener et al., the question remains whether the inner doublet observed in NFS and Mößbauer spectroscopy in our sample could be explained in a similar fashion.

The formation of ferrocene-dimers as reported by Wagener et al. is not plausible in our case because

- ferrocene molecules are only present in a very dilute dispersion in our sample, the amount of dimers should be considerably lower than in the samples investigated by Wagener et al.

- if a simple dimerization of ferrocene would be possible the question arises why the corresponding inner doublet was never observed in previous experiments of pure ferrocene in bulk [GG71], DBP:ferrocene in bulk [MFW+97] or confined in controlled pore glasses [ASF+01].

- comparable doublets have been observed in pure ferrocene loaded into the cages of the nanoporous zeolith $AlPO_4$-5 [AVGOK05]. Since electron spin resonance did not yield any signal down to 4.2 K, dimerization as a possible source for this doublet was excluded by the authors.

Obviously another mechanism which generates these reduced quadrupole splittings in meso- and nanoporous matrices specifically is needed.

8.2.2 Oxidation of ferrocene in porous silicon?

Ferrocene is a very stable molecule, as well in bulk crystalline state as solved in DBP: After more than 1 year of storage no traces of oxidation products were found in the DBP:ferrocene sample which was used to fill the porous silicon. There has been evidence for quick oxidation of metallocenes in zeolites reported by Ozin et al. [OG89], but this could be attributed to the strong polarity and ion-exchange capability of the zeolite host-lattice.

Only recently Toda et al. [TII+04] have reported that also in MCM-41 oxidation of ferrocene is strongly induced. MCM-41 samples were prepared under acidic (MCM-A) or basic (MCM-B) conditions, leading to pore-diameters of 2.8 nm and 0.9 nm. Ferrocene was adsorbed in the pores at 413 K to 5 % respectively 25 % with ferrocene enriched in ^{57}Fe.

Immediately after filling, MCM-A showed the existence of paramagnetic iron which was later identified to be part of ferrocenium, the cation of ferrocene. MCM-B was free of ferrocenium initially, but over the period of several months an amount of ferrocenium formed also.

The amount of paramagnetic iron was estimated by ESR to be $74 \pm 5\%$ and $6.5 \pm 0.5\%$ in MCM-A and MCM-B, respectively. Toda et al. conclude that the oxidation rates strongly depend upon the pore diameter.

In our case we have to consider the oxidation of ferrocene (valence state II) into ferrocenium with valence state III. Like before in the case of dimerization the iron in ferrocene has to get rid of one electron, but this time **permanently**. Since oxidation was only observed in porous media the host lattice has to play a crucial role in this reaction, e.g. by absorbing the electron at a local defect site.

If we assume a remaining host-oxide interaction this could further explain why the amplitude of the oxidation products was so temperature-independent (see Fig. 5.10 and 5.11): Ferrocene adsorbed on the surface of a silicon matrix would participate in the vibrational dynamics of the solid silicon (Debye temperature $T_\Theta = 625$ K). This is further backed by the argument that we did not observe any oxidation products outside the porous silicon matrix.

But as before in this case of valence-state mixing some major questions remain:

- Toda et al. found that ferrocene was oxidized into ferrocenium. The isomer shift of ferrocenium matches the values found in the experiments, but the values of its quadrupole splitting found in literature of only $\approx 2.1\,\Gamma$ is significantly lower than the observed splittings [GG71] [HH97].

- Oxidation of ferrocene to ferrocenium and a rigid chemical binding to the porous silicon matrix could explain the existence of a reduced quadrupole splitting at temperatures significantly higher than T_C. But even at temperatures 40 K above T_C the major fraction of the NFS-signal corresponds to (1), which can only be interpreted as unoxidized ferrocene! Thereby the oxidation model is not able to explain on its own, why *both* spectroscopic components (1) and (3) are observed far above T_C.

  Off course one could argue, that the existence of the spectroscopic component (3) at higher temperatures could be linked to oxidized ferrocene bound to the silicon host matrix and participating in its dynamics, and the existence of (1) resembles unoxidized ferrocene in the remaining pore, whose glass transition temperature is shifted due to confinement effects.

- Additionally, this model can only explain the fast decaying line (2) by additional assumptions, e.g. fast molecular dynamics resulting in motional narrowing of the quadrupole doublet.

- A change of the oxidization state of iron should lead to a shift of the iron K-absorption edge towards higher energies. The XANES experiments presented in chapter 6 showed no shift of the absorption edge of iron with respect to bulk DBP:ferrocene.

Overall, the oxidation model could only explain small parts of the observed phenomena, e.g. the existence of spectroscopic component (3); other models are required to explain the remaining spectroscopic components (1) and (2). Consequently a model being capable to explain the existence of more or all spectroscopic components would be preferred over the oxidation model.

8.3 Anisotropic relaxation of the ferrocene molecule

Anisotropic relaxation of ferrocene was first presented by Gibb in his work on ferrocene in thiourea-ferrocene clathrates in 1976 [Gib76]. A recent work [AVGOK05] also relies on anisotropic relaxation to qualitatively discuss dynamics of ferrocene in confinement. As was shown in chapter 7 the presented data can also be understood as a result of anisotropic relaxation of ferrocene molecules in porous silicon.

As was pointed out before (see chapter 1.3.2) dynamical heterogeneity (e.g. regions of fast or slow relaxation rates) may be caused by the liquid-wall interaction. The theoretical model developed with MONDIA proposed in chapter 7 assumes three different relaxation centers. These may be understood as a result of ferrocene surroundings with different magnitude of wall-liquid interaction:

1. A ferrocene molecule in surroundings **without** wall-liquid interaction would produce a bulk-like quadrupole splitting at low temperatures. Upon heating the Lamb-Mößbauer factor decreases, which leads to a complete destruction of the coherent signal produced by this fraction at higher temperatures.

2. Other ferrocene molecules in a surroundings **with** wall-liquid interaction, e.g. in direct contact with the pore wall show different behavior: While they produce the same, bulk-like quadrupole splitting at lower temperatures, the increase of their translational movement is slowed down at higher temperatures (as observed by Scheidler et al.). Depending on which kind of *rotational* relaxation the molecule can carry out, two subensembles are possible:

(a) If isotropic rotational relaxation is possible and fast (relaxation times $<<$ 140 ns) then a complete **collapse** of the quadrupole doublet is observed - this corresponds to the **fast decaying line (2)**.

(b) If fast rotational relaxation is anisotropic, e.g. only possible in one plane then a partial **reduction of the quadrupole doublet** will result - corresponding to a mixture of the bulk-like quadrupole splitting (1) and the reduced quadrupole splitting (3).

To understand this model better a comparison of the fraction showing the reduced quadrupole splitting (3) by the static fit (see Fig. 4.10, 4.11 and 4.12) with the occupation of the relaxation center (3) by MONDIA (see Fig. 7.8, 7.9 and 7.10) is useful. Obviously the fractions of the third relaxation center obtained by MONDIA for all samples increase during the glass transition to values up to 50%. On the other hand, values of the fractions for the reduced quadrupole splitting are a factor of approximately 2 lower for sample #4 and #5. The values for sample #2 are increased, but this is most probably attributed to the small time window of 16-bunch mode which cuts off the time spectra after the first, huge interference of principal and reduced quadrupole frequencies at 50 - 80 ns, which can have caused a systematic overestimation of the fraction of the reduced quadrupole splitting.

This seemingly disagreement between the static fit and the MONDIA model is directly related to the physical model implemented in MONDIA: The third relaxation center not only produces the reduced quadrupole doublet that was connected with the fraction obtained from the static fit. The spectrum of an anisotropic rotating molecule consist of both a principal and a reduced quadrupole doublet. Thereby we would expect the values for the fraction obtained from the static fit to underestimate the total percentage of ferrocene molecules undergoing anisotropic rotation, while overestimating those participating in bulk-like dynamics.

This model explains:

- the **existence** of a **reduced quadrupole splitting** due to fast anisotropic relaxation of the ferrocene molecule.

- a **constant or even rising weight** of the reduced quadrupole doublet as observed in Mößbauer spectroscopy. Thermal excitation of anisotropic relaxation will lead to an increase of the reduced quadrupole doublet, while simultaneously the Lamb-Mößbauer factor decreases.

- the **existence** of a **fast decaying line** on the same basis as the reduced quadrupole doublet, which is further backed by the fact that the occupational increase is nearly identical.

But also in this case some questions remain:

- A strong wall-liquid interaction had to be assumed, capable of inducing an asymmetry parameter of significant magnitude ($\eta > 0.25$). Due to the limitations of the MONDIA-model (no distribution of jump rates, quadrupole splittings, etc. but only three exemplary relaxation centers) the values of η have to be understood as approximate mean values.

  This result is supported by the decreased pre-peak observed in the XANES-experiments, which yielded evidence for a possible distortion of the ferrocene molecule in porous silicon compared with bulk DBP:ferrocene.

  In the literature also possibilities for a direct or indirect bonding of ferrocene molecules to a chlorine terminated silicon-surface are discussed: Gun'ko et al. demonstrated, that lithiated ferrocene bonds to chlorine-capped silicon directly via the cyclopentadienyl ring, or via a propylsiloxy spacer group [GPB+03]. A ferrocene molecule bond via the cyclopentadienyl ring to silicon would not be able to rotate or diffuse freely, and we can not rule out that the isomer shift could also deviate slightly from free ferrocene due to the change of the chemical environment of the iron nucleus, but a change of the valence state of iron does not seem plausible due to this kind of bonding.

- The change of the isomer shift as observed in NFS and Mößbauer spectroscopy is not predicted by the presented model of anisotropic relaxation. The question whether a strong wall-ferrocene interaction may have induced changes of the electronic configuration, and thereby of the s-electron density at the nucleus, or if other processes are responsible for this change remains open.

A similar change of the isomer shift was observed by Lund et al. in $AlPO_4$-5:ferrocene [LNW94]: At 20 K the quadrupole splitting and isomer shift of bulk ferrocene ($\delta = 5.6\Gamma$) were measured, at room temperature the quadrupole doublet was almost completely narrowed due to rotational dynamics, and the isomer shift was reduced to $\delta = 4.0\,\Gamma$. This agrees very well with the difference of the isomer shift found in our experiments of $\approx 1.2\,\Gamma$. That indeed a fast rotational molecular relaxation is responsible for these changes of the hyperfine parameters was not only observed with Mößbauer spectroscopy, but also with ^{2}H NMR ([AVGOK05]. ^{2}H NMR of ferrocene is only sensitive to the motion of the hydrogen nuclei; a change of the valence state due to dimerization or oxidation of the central iron atom has no influence on the NMR-results. The authors interpret their spectra as being caused by rotational dynamics of the ferrocene molecules.

Thus changes of the isomer shift in the presence of rotational dynamics as observed in the presented experiments also are discussed in the literature for comparable porous matrices.

8.4 The glassy dynamic of DBP:ferrocene in porous silicon

In this section the results of the presented experiment concerning glass dynamics are discussed. First, the temperature dependence of the diffusive molecular motion as observed in our experiments is addressed. In the second part the orientation dependence and shift of the mode-coupling critical temperature T_C is examined.

8.4.1 Diffusive molecular motion

In previous works on DBP:ferrocene in isotropic confinement (controlled pore glasses (CPG) without any preference orientation of the pores) a reduction of the relaxation rate ($= 1/\tau_{diff}$) was found [ASF+01]. The relaxation time τ_{diff} does not decrease below 2-3 τ_0. This was attributed to a slowing down of molecular dynamics in confinement as predicted by Scheidler et al. in a matrix with a rough wall. But no shift of the glass transition itself was observed.

We were not able to measure τ_{diff} in sample #2 with NFS due to the small time window in 16-bunch mode, but a broadening of the line width of the outer doublet was observed with Mößbauer spectroscopy in sample #2 and #4 (see Fig. 5.12 and 5.13), which must be attributed to increasing relaxational dynamics. Unfortunately, the experimental errors are too large in both samples to resolve any orientation dependence of the diffusive motion.

Our NFS-experiments in porous silicon yielded values for the time of diffusive motion τ_{diff} in the case of sample #4 and #5 (see Fig. 4.22 and 4.23). As before in the case of the CPGes the relaxation time decreased from starting values much larger than the nuclear life time τ_0 continuously down to values between 2-3 τ_0. This behavior is virtually independent of the pore size (#4 has a pore-diameter of 2-3 nm, and #5 10-15 nm, respectively). Relaxation in sample #5 shows no dependence upon the pore orientation. For sample #4 with the smallest pore size there is a strong dependence upon the pore orientation, relaxational motion is enhanced along the pore axis and hindered perpendicular to it.

Following Scheidler et al. the wall influences the glassy dynamics up to a depth of several molecular diameters. In sample #4 the whole pore would be affected, while in sample #5 the inner parts of the pore would be unaffected. This explains why we observed a strong orientation dependence of the diffusion in sample #4 while the remaining small orientation dependence in sample #5 may have been concealed by the experimental error. This is evidence for an ***anisotropy of the viscosity***, which could be either caused by an anisotropy of the hopping parameter δ alone, or indicate an anisotropy of the whole glass transition in confinement.

8.4.2 The shift of the critical temperature T_C

The square-root law prediction of mode-coupling theory in Eq. 1.13 was fitted to the Lamb-Mößbauer factor obtained from the data, and the values of T_C corresponding to the fits are displayed in Tab. 8.1:

	#2	**#4**	**#5**
Parallel orientation	229 ± 2 K	234 ± 6 K	235 ± 6 K
Perpendicular orientation	276 ± 7 K	258 ± 6 K	-

Table 8.1: Shift of the mode-coupling critical temperature T_C. Only experimental errors as derived from the fit are displayed, systematic errors are not accounted for.

The square-root law from MCT can be applied in the parallel case to all samples successfully, and it describes the deviations from the harmonic Debye approximation very well. The shifts of the mode-coupling critical temperature T_C to higher temperatures were measured, the values of T_C for all samples in the parallel case coincide in the margin of error with a mean T_C of 233 ± 3 K. This indicates a shift of the glass transition of nearly 30 K, which may be caused either by an indirect change of the molecular dynamics induced by the confinement as compared to bulk dynamics, or e.g. simply by the strong surface-molecule interactions.

In the perpendicular case we expect the effect on the glassy dynamics caused by the confining of the glass former to be increased, while the effects induced by surface-molecule interaction can be assumed to be isotropic and thereby have to remain constant. The deviations from the Debye-model in the perpendicular case are obviously smaller, and the fit of the square-root law to these deviations succeeded only in the case of sample #2 and #4. For sample #5 also a fit was attempted, but values for T_C would have exceeded 280 K.

The nearly harmonic temperature dependence of f_{LM} in sample #5 either could indicate that at least the ***square-root law predicted by mode-coupling theory fails in confinement***. But also in sample #5 there exist deviations from the harmonic approximation, and in the other cases could be well described by the square-root law.

It is more plausible to attribute this harmonic temperature dependence to a ***smearing of the glass transition*** caused e.g. by strong heterogeneities of the dynamics. For example the value of T_C could strongly depend upon the distance from the pore axis (slow dynamics close to the wall vs. fast dynamics far from the wall). This can, additionally, explain why the deviation from the Debye approximation is smaller in sample #5 as compared to #4, since one would assume a lesser degree of heterogeneity in a narrow pore than in a pore with large diameter. The value of T_C is obviously increasing with the pore diameter distribution width from sample #4 (pore diameter 2-3 nm, δr = 1 nm) over #2 (pore diameter 5-8 nm, δr = 3 nm) up to #5 (pore diameter 10-15 nm, δr = 5 nm).

In total there exists a strong orientation dependence of the Lamb-Mößbauer factor: along the pore axis results from different samples are very comparable, and a square-root law is obviously able to describe the deviations from the harmonic behavior satisfactorily. Perpendicular to the pore axis almost harmonic behavior is observed. Since the vanishing of the Lamb-Mößbauer factor is directly connected to the glassy dynamics, the observed differences are strong evidence for a ***anisotropy of the glass transition*** in confinement.

Since the additional shifts of T_C in the perpendicular case are purely caused by the structural changes of the liquid induced by the confinement we can with this method for the first time distinguish between surface- and confinement-induced effects in DBP:ferrocene. Not taking into account the shift of T_C in the parallel case a shift of at least several ten degrees remains, which is attributed to a ***slowing down of dynamics in confinement***.

9. CONCLUSION

The experimental data obtained from nuclear resonant scattering and Mößbauer spectroscopy as presented in this work proves that the glass transition and the molecular dynamics of DBP:ferrocene is significantly different in anisotropic confinement as compared to bulk samples or samples in isotropic confinement (e.g. controlled pore glasses).

The different spectroscopic components found in the time and energy spectra were successfully identified as being caused by ferrocene molecules undergoing ***different, partially anisotropic rotational dynamics***, which is in accordance with recent works on ferrocene confined in zeolithes [AVGOK05]. In our opinion other models attempting to explain the existence of the spectroscopic components on the basis of ***dimerization or oxidation of ferrocene*** can be ruled out.

We observed molecular dynamics due to two different mechanisms: The diffusion of ferrocene molecules on the time-scale of τ_{diff} (can be up to the order of the nuclear life time) which can be connected to the α-relaxation, and a change of the Lamb-Mößbauer factor f_{LM} which is directly connected to the β-relaxation and the vibrational dynamics.

The obtained values for τ_{diff} coincide with recent works on DBP:ferrocene in isotropic confinement [ASF$^+$01], their orientation dependence was linked to the pore diameter of the samples under investigation. We thereby observed a ***slowing down of molecular dynamics of the $\alpha-$relaxation in confinement.***

The orientation dependence of f_{LM} was also very pronounced: While the glass transition was shifted consistently to values around 233 K in the case of parallel orientation of the confining pores, the sample in the perpendicular orientation either did not behave as predicted by MCT or the ***glass transition was smeared out*** over a large temperature interval. The final discrimination between these two interpretations has to be achieved by further experiments in confining matrices, supported by molecular dynamics simulations exploring the orientation dependence for temperatures even closer to T_C.

Furthermore, the shift of T_C was splitted into a shift partially caused by wall-liquid interaction and a shift caused solely by the change of sample orientation, which was consequently attributed to geometrical confinement effects only. Thereby we measured a ***shift of the glass transition in confinement***, which is not to be attributed to wall-liquid interaction. Since this was observed in ***all*** samples ***confinement-induced effects play a decisive role up to pore diameters of 10-15 nm***.

In general, examining the orientation dependence of experimental parameters connected to the glass transition yielded and will yield new, important insights into the glass dynamics unaccessible otherwise. Discovering suitable confining matrices with high aspect ratios of pore diameter / pore length, good pore orientation, well defined pore morphology and sufficient long time stability poses the main problem, especially if macroscopic samples are required for the successful implementation of experiments.

APPENDIX

A. ACKNOWLEDGEMENTS

Many people have been involved in this thesis, and without their support this thesis would not have been possible. I would like to express my gratitude to them:

First of all, I would like to thank my supervisor, **Dr. Hermann Franz**. Since he introduced me to nuclear resonant scattering during a proseminar five years ago, I had the opportunity to learn from him. I enjoyed (and massively exploited) the fact that he always found the time to discuss with me.

I am further indebted to **Prof. Dr. Jochen R. Schneider** and the entire **HEP work group** for the opportunity to do my PhD-thesis among them at the HASYLAB.

The search for a feasible mesoporous matrix lasted at least the first year of my thesis, and without **Dr. Uwe van Bürcks** idea to implement porous silicon, I would probably still be searching. He also established contact with **Dr. Victor Yurievich Timoshenko**, who was responsible for manufacturing the porous silicon films.

Dr. Tanja Asthalter, **Dr. Ilia Sergueev**, **Dr. Aleksander Chumakov** and **Dr. Olaf Leupold** did not only provided important support when it came to prepare samples and set up experiments at the ESRF, they also gave invaluable advice and help concerning the interpretation and classification of the results.

A big "thank you!" goes to Lübeck: The Mößbauer-spectroscopy experiments were performed together with **Dr. habil. Heiner Winkler** in the group of **Prof. Dr. Alfred X. Trautwein**. Heiner Winkler and **Dr. Mati Haas** created MONDIA by adapting SYNFOS to my special needs.

Sergio Funari and **Martin Dommach** gave advice and help concerning SAXS-experiments and their interpretation, as did **Konstantin Klementiev** and **Edmund Welter** concerning XANES.

I have to thank **Jens Brehling** and his crew for their patience whenever I wanted another variant of my sample holders or needed any kind of tiny-special-gadget. For the cutting process of the mesoporous films I must thank **Peter Stutz** from the Mineralogisch-Petrographischem Institut, who gave me unrestrained access to "his" diamond wire saw and workshop.

All my **fellow PhD-students** from the HASYLAB Doktorandenseminar, who either enjoyed or endured my talks and questions . . . I enjoyed it.

A friend of mine, **Oliver Gries**, has to be mentioned. Despite the fact that he is no physicist, he proofread my entire work with the unshakeable determination to hunt down every mistake, wrong preposition and forgotten comma.

And last but not least I have to thank **my family**, which supported me throughout my course of studies.

Thank you!

B. BIBLIOGRAPHY

BIBLIOGRAPHY

[AG65] G. Adam and J.H. Gibbs. On the Temperature Dependence of Cooperative Relaxation Properties in Glass-Forming Liquids. *J.Chem.Phys.*, 43:139–146, July 1965.

[And54] P.W. Anderson. A Mathematical Model for the Narrowing of Spectral Lines by Exchange or Motion. *J.Phys.Soc.Japan*, 9:316, 1954.

[ASF+01] T. Asthalter, I. Sergueev, H. Franz, K. Messel, W. Petry, P. Haerter, and A. Huwe. Quasielastic Nuclear Forward Scattering as a Background-Free Probe of Slow Glass Dynamics in Confined Geometries. *Euro.J.Phys.B*, 22:301, 2001.

[ASG+97] M. Arndt, R. Stannarius, H. Groothues, E. Hempel, and F. Kremer. Length Scale of Cooperativity in the Dynamic Glass Transition. *Phys.Rev.Lett.*, 79:2077, 1997.

[AVGOK05] T. Asthalter, J. Villanueva Garibay, V. Olszowka, and J. Kornatowski. Dynamics of ferrocene in $AlPO_4$-5 single crystals probed by nuclear forward scattering. *J.Chem.Phys.*, 122:014508, 2005.

[BB04] G. Biroli and J.-P. Bouchaud. Diverging length scale and upper critical dimension in the Mode-Coupling Theory of the glass transition. *Eur. Phys. Lett.*, 67(1):21–27, 2004.

[BC63] S. Bernstein and E.C. Campbell. Nuclear Anomalous Dispersion in ^{57}Fe by the Method of Total Reflection. *Phys. Rev.*, 132(4):1625–1633, July 1963.

[BD64] P.J. Black and I.P. Duerdoth. A direct observation of diffraction in nuclear resonant scattering. *Proc. Phys. Soc.*, 84:169, 1964.

[BGS84] U. Bengtzelius, W. Götze, and A. Sjölander. Dynamics of supercooled liquids and the glass transition. *J.Phys.C: Solid State Phys.*, 17(33):5915–5934, November 1984.

[Blu68] M. Blume. Stochastic Theory of Line Shape: Generalization of the Kubo-Anderson Model. *Phys.Rev.*, 174:351, 1968.

[BOJ+03] A. J. Berry, H.St.C. O'Neill, K.D. Jayasuriya, S.J. Campbell, and G.J. Foran. XANES calibration for the oxidation state of iron in a silicalite glass. *Am.Min.*, 88:967–977, 2003.

[BT68] M. Blume and J.A. Tjon. Mössbauer spectra in a fluctuating environment. *Phys.Rev.*, 165(2):446–456, January 1968.

[CDF+93] H.Z. Cummins, W.M. Du, M. Fuchs, W. Götze, S. Hildebrand, A. Latz, G. Li, and N.J. Tao. Light-scattering spectroscopy of the liquid-glass transition in $CaKNO_3$ and in the molecular glass Salol: Extended-mode-coupling-theory analysis. *Phys.Rev.E*, 47(6):4223–4239, 1993.

[Chu02] A.I. Chumakov. Mößbauer spectroscopy on bulk dibutylphthalate:ferrocene. Private communication, 2002.

[CT59] M.H. Cohen and D. Turnbull. Molecular transport in liquids and glasses. *J. Chem. Phys.*, 31:1164–1169, 1959.

[Cum99] H.Z. Cummins. The liquid-glass transition: a mode-coupling perspective. *J.Phys.C:Condens.Matter*, 11:A95, 1999.

[Dat81] Dattagupta. Study of time-dependent hyperfine interactions by PAC, Mössbauer effect, μSR and NMR - a review of stochastic models. *Hyperfine Interact.*, 11:77 – 126, 1981.

[DB74a] S. Dattagupta and M. Blume. Stochastic theory of line shape: I. Nonsecular effects in the strong collision model. *Phys.Rev.B*, 10(11):4540–4550, December 1974.

[DB74b] S. Dattagupta and M. Blume. Stochastic theory of line shape: II. Nonsecular effects in the EPR spectrum of CO_2^- in calcite. *Phys.Rev.B*, 10(11):4551–4559, December 1974.

[Deb96] P.G. Debenedetti. *Metastable Liquids*. Princeton University Press, 1996.

[DLC+94] W.M. Du, G. Li, H.Z. Cummins, M. Fuchs, J. Toulouse, and L.A. Knauss. Light-scattering study of the liquid-glass transition in propylene carbonate. *Phys.Rev.E*, 49(3):2192–2205, 1994.

[FGHL92] M. Fuchs, W. Götze, S. Hildebrand, and A. Latz. A theory for the ?-relaxation process near the liquid-to-glass crossover. *J.Phys.:Condens.Matter*, 4:7709, 1992.

[FKZ03] B. Frick, M. Koza, and R. Zorn. *2nd International Workshop on Dynamics in Confinement*. European Physical Journal E, 2003.

[FM99] M. Fuchs and M.R. Mayr. Aspects of the dynamics of colloidal suspensions: Further results of the mode-coupling theory of structural relaxation. *Phys.Rev.E*, 60(5):5742–5752, November 1999.

[GG71] N.N. Greenwood and T.C. Gibb. *Mößbauer Spectroscopy*. Chapman and Hall Ltd., 1971.

[Gib76] T.C. Gibb. Anisotropic relaxation of the electric field gradient tensor in the ^{57}Fe Mössbauer spectra of a thiourea-ferrocene clathrate. *J.Phys.C: Solid State Phys.*, 9:2627–2642, March 1976.

[GO82] O. Glatter and Kratky. O. *Small Angle X-ray Scattering*. Acedemic Press, 1982.

[GPB+03] Y.K. Gun'ko, T.S. Perova, S. Balakrishnan, D.A. Potapova, R.A. Moore, and E.V. Astrova. Chemical modifications of silicon surfaces with ferrocene functionalities. *phys.stat.sol (a)*, 197:492–496, 2003.

[GS92] W. Götze and L. Sjögren. Relaxation processes in supercooled liquids. *Re.Prog.Phys.*, 55(3):241–376, March 1992.

[HH97] R.H. Herber and T.P. Hanusa. Hyperfine Interactions and Lattice Dynamics of Ferrocene, Ring-substituted Ferrocenes, and their Oxidation Products. *Hyperfine Interact.*, 108:563–575, 1997.

[HRW+00] M. Haas, E. Realo, H. Winkler, W. Meyer-Klaucke, and A.X. Trautwein. SYNFOS. *Hyperfine Interact.*, 125:189–195, 2000.

[Kaw70] Kawasaki. Kinetic equations and time correlation functions of critical fluctuations. *Ann.Phys.*, 61(1):1–56, November 1970.

[KBD+92] M. Kiebel, E. Bartsch, O. Debus, F. Fujara, W. Petry, and H. Sillescu. Secondary relaxation in the glass-transition regime of ortho-terphenyl observed by incoherent neutron scattering. *Phys.Rev.B*, 45(8):10301–10305, 1992.

[Käm97] Kämmerer, S. and Kob, W. and Schilling, R. Dynamics of the rotational degrees of freedom in a supercooled liquid of diatomic molecules. *Phys.Rev.E*, 56(5):5450, November 1997.

[Käm04] Kämmerer, S. and Kob, W. and Schilling, R. Test of mode-coupling theory for a supercooled liquid of diatomic molecules. II. q-dependend rotational correlators. *Phys.Rev.E*, 58:2141, 2004.

[KS98] V.G. Kohn and G.V. Smirnov. Theory of nuclear resonant scattering of synchrotron radiation in the presence of diffusive motion of nuclei. II. *Phys.Rev.B*, 57:5788, 1998.

[KS99] V.G. Kohn and G.V. Smirnov. Synchrotron radiation time spectra affected by diffusion: theory. *Hyperfine Inter.*, 123/124:327, 1999.

[KT54] R. Kubo and K. Tomita. A General Theory of Magnetic Resonance Absorption. *J.Phys.Soc.Japan*, 9:888, 1954.

[Lam39] W.E. Lamb. Capture of Neutrons by Atoms in a Crystal. *Phys.Rev.*, 55:190, 1939.

[Leh02] V. Lehmann. *Electrochemistry of Silicon*. WILEY-VCH Verlag, Weinheim, 2002.

[Leu84] E. Leutheusser. Dynamical model of the liquid-glass transition. *Phys.Rev.A*, 29(5):2765–2773, May 1984.

[Leu04] O. Leupold. Resonance line broadening of ferrocene in DBP. Private communication, October 2004.

[LNW94] A. Lund, V.P. Nicholson, Parish, and J.P. Wright. ^{57}Fe Mössbauer Spectroscopic Studies of the Ferrocene Molecular Reorientation in $AlPO_4$-5 and $AlPO_4$-8 Frameworks. *Acta Chem.Scand.*, 48:738–741, 1994.

[McK03] G.B. McKenna. Status of our understanding of dynamics in confinement: Perspectives from Confit 2003. *Eur. Phys. J. E*, 12:191–194, 2003.

[MFW$^+$97] A. Meyer, H. Franz, J. Wuttke, W. Petry, N. Wiele, R. Rüffer, and C. Hübsch. Resonant Scattering of Synchrotron Radiation for the Study of the Dynamics around the Glass Transition. *Z.Phys.B*, 103:479, 1997.

[OG89] G.A. Ozin and J. Godber. Intrazeolite Metallocenes: Chemistry, Spectroscopy and Dynamics. *J. Phys. Chem.*, 93(2):878–893, 1989.

[Oss03] P.M. Ossi. *Disordered Materials*. Springer, 2003.

[PR60] R.V. Pound and G.A. Rebka. Apparent weight of photons. *Phys.Rev.Lett.*, 4:337, April 1960.

[RLLG+88] M.F. Ruiz-Lopez, M. Loos, J. Goulon, M. Benfatto, and C.R. Natoli. Reinvestigation of the EXAFS and XANES spectra of ferrocene and nickelocene in the framework of the multiple scattering theory. *Chem.Phys.*, 121:419–437, 1988.

[RZF76] S.L. Ruby, B.J. Zabransky, and P.A. Flinn. Molcular Motions in a viscous organic Liquid: Ferrocene in cold butyl phthalate. *J.Physique*, 12:C6–745, 1976.

[Sac58] R.A. Sack. Contribution to the theory of the exchange narrowing of spectral lines. *Mol. Phys.*, 1:163–167, 1958.

[Sch00] R. Schilling. Mode-coupling theory for translational and orientational dynamics near the ideal glass transition. *J.Phys:Cond.Matt.*, 12:6311–6322, 2000.

[Sch02] Ernst Schreier. Mössbauer isotopes in the energy range 6 keV - 30 keV and with lifetimes greater than 1 ns. http://www.esrf.fr/exp_facilities/ID18/pages/technique-/moess/tech_isotopes.html, 2002.

[Sch03] R. Schilling. Theories of the Structural Glass Transition. *appears in "Collective Dynamics of Nonlinear and Disordered Systems", eds. G.Radons, W.Just and P.Haeussler, Spronger(2003)*, 2003.

[Ser04] I. Sergueev. *Structural relaxation in a viscous liquid studied by quasi-elastic nuclear forward scattering.* PhD-Thesis, http://tumb1.biblio.tu-muenchen.de/publ/diss/ph/2004/sergueev.html, Technische Universität München, 2004.

[SF03] J.S. Sharp and J.A. Forrest. Tickness dependence of the dynamics in thin films of iostactic poly(methylmethacrylate). *Eur. Phys. J. E*, 12:S97–S101, 2003.

[SFA+02] I. Sergueev, H. Franz, T. Asthalter, W. Petry, U. van Bürck, and G.V. Smirnov. Structural relaxation in a viscous liquid studied by quasielastic nuclear forward scattering. *Phys.Rev.B*, 66(184210):1–8, November 2002.

[SK95] G.V. Smirnov and V.G. Kohn. Theory of nuclear resonant scattering of synchrotron radiation in the presence of diffusive motion of nuclei. *Phys.Rev.B*, 52:3356, 1995.

[SKB00] P. Scheidler, W. Kob, and K. Binder. The relaxation dynamics of a simple glass former confined in a pore. *Europhys.Lett.*, 52:277, 2000.

[SKB02] P. Scheidler, W. Kob, and K. Binder. Cooperative motion and growing length scales in supercooled confined liquids. *Europhys.Lett.*, 59:701–707, 2002.

[SKB03] P. Scheidler, W. Kob, and K. Binder. The relaxation of a confined glassy simple liquid. *Euro. Phys. J. E*, 12:5–9, 2003.

[TB68] J.A. Tjon and M. Blume. Mössbauer spectra in a fluctuating environment II: Randomly Varying Electric Field Gradients. *Phys.Rev.*, 165(2):456–461, January 1968.

[TII+04] Y. Toda, S. Ishimaru, R. Ikeda, T. Mitani, S. Kitao, and M. Seto. Oxidation of ferrocene molecules adsorbed in MCM-41. *J. Phys. Chem. Solids*, 65:471–473, 2004.

[Weg65] H. Wegener. *Der Mößbauereffekt und seine Anwendung in Physik und Chemie*. Bibliographisches Institut AG Mannheim, 1965.

[WHF+94] W. Wagener, M. Hillberg, R. Feyerherm, W. Stieler, F.J. Litterst, T. Pöhlmann, and O. Nuyken. Mixed Valence behaviour in polymeres containing ferrocene. *J.Phys: Condens. Matter*, 6:L391–L398, July 1994.